Collective effects and experimental verification of the CLIC drive beam and decelerator

Reidar Lunde Lillestøl
Department of Physics
University of Oslo
Norway

Dissertation presented for the degree of
Philosophiae Doctor (PhD) in Physics

July 2014

Series of dissertations submitted to the
Faculty of Mathematics and Natural Sciences, University of Oslo
No. 1569

ISSN 1501-7710

Cover: Hanne Baadsgaard Utigard.
Printed in Norway: AIT Oslo AS.

Produced in co-operation with Akademika Publishing.
The thesis is produced by Akademika Publishing merely in connection with the thesis defence. Kindly direct all inquiries regarding the thesis to the copyright holder or the unit which grants the doctorate.

Abstract

The Compact Linear Collider (CLIC) is a potential next-generation particle collider, in which electrons and positrons collide at a center-of-mass energy of up to 3 TeV. In order to reach a high accelerating gradient and reduce the length of the machine, CLIC uses a novel two-beam scheme. Here, the acceleration energy for the main beam is provided by energy extraction from a secondary electron drive beam, by the use of Power Extraction and Transfer Structures (PETS).

This Ph.D. thesis describes deceleration measurements from the CLIC Test Facility 3 at CERN, from a beam that had up to 37 % of its kinetic energy converted into 12 GHz rf power. The results are part of the feasibility demonstration of the CLIC scheme. The measured difference in beam energy of the decelerated beam is correlated with particle tracking simulations and with predictions based on analytical formulae, and a very good agreement is demonstrated. The evolution of the transverse emittance was also studied, since it is critical to contain the large drive beam within the limited available aperture. The emittance was not found to increase from other effects than adiabatic undamping.

In order to reach consistency between measurements, theory and simulations, it is important to take the bunch phase into account, which affects the rf field produced in the PETS. New formulae have been derived to take this effect into account.

Also longitudinal space charge in the CLIC decelerator has been studied. It has been a concern that, despite the high energy of the CLIC drive beam, longitudinal space charge may lead to a violation of the strict bunch length tolerance. However, it is shown that the space charge effect is still negligible. For this a new Particle-in-Cell written in Octave was developed, and is described in the thesis.

Contents

List of Figures

List of Tables

Chapter 1

Introduction

This Ph.D. thesis concerns accelerator physics related to the global effort towards a future linear electron-positron collider. Specifically, we look at energy extraction from a high-intensity *drive beam* in the Compact Linear Collider (CLIC) scheme, and study the beam dynamics and associated rf power production. Experimental data from the CLIC Test Facility at CERN are compared to theory and simulations. In addition, the influence of space charge on the longitudinal bunch distribution has been studied with simulations.

This chapter presents some background, and an outline of the thesis is given in Section 1.3.

1.1 CERN and high-energy physics

CERN is the European Center for Particle Physics (originally Conseil Européen pour la Recherche Nucléaire) and is the largest laboratory for particle physics in the world. The organization was founded after the second world war, partly to revive and reunite European science after the second world war. Throughout the years a number of achievements have been made at the laboratory, including the discovery of the W and Z bosons, the creation, isolation and trapping of antihydrogen atoms, and most recently the discovery of a spinless boson consistent with the long-sought Higgs boson.

CERN has a large complex of particle accelerators, and some are pushing the frontiers in high-energy physics. One accelerator is the Proton Synchrotron, which is more than 50 years old and still in operation, acting as a pre-accelerator for the larger rings. The largest machine at the laboratory is the storage ring Large Hadron Collider (LHC), which is designed to accelerate protons to an energy of 7 TeV per beam. LHC has so far successfully collided beams of up to 4 TeV, which led to the discovery of the elusive Higgs boson, around 40 years after its theoretical prediction.

The Higgs particle was the last piece of the puzzle that is the *standard model*, which mediates the known theory about sub-atomic particles. This comprises the matter particles (fermions), three of the four fundamental forces in nature (bosons) and the Higgs boson that gives particles mass. However, the theory has some shortcomings. Firstly, it does not include gravity, which is one of the four fundamental forces. One may predict that there exists a boson for this force, but since gravity is much weaker than the other three forces at small ranges[1], it is currently not possible to investigate this.

[1] With example sources and sub-atomic distances, gravity is 10^{40} times weaker than electromagnetism [1].

In addition, the standard model only accounts for 4.9 % of the mass/energy in space [2]. In addition to the normal matter, 26.8 % comprises dark matter that affects the motion of large-scale objects like galaxies, and 68.3 % comprises a hypothetical dark energy that tends to accelerate the expansion of the universe. Physics beyond the standard model is clearly needed to understand these phenomena. The group of theories known as *supersymmetry* is a potential candidate to explain some of this, and postulates that all existing particles have a "superpartner". The superpartner shares most of the properties of the normal particle except for a difference in *spin*, which changes the fermions' superpartners to bosons and vice versa. The LHC has probed some of these models, but so far there has been no evidence for supersymmetry, only constraints on the possible masses of the particles [3]. However, many models are still not validated, but when the LHC is running at full energy our knowledge will hopefully be expanded further.

1.2 Future particle colliders

The LHC is the latest and most powerful machine from a century with increasingly energetic particle accelerators. Still, even though the LHC is expected to run for approximately another 20 years, feasibility studies of the next generation colliders have been going on for decades. The reason is that the each generation of particle accelerator is more technically advanced, and increasingly more research and development is needed.

The main motivation for building a new collider is to get access to new physics. For example, collisions between other particles will bring other particle interactions. A promising candidate for the next generation collider is a lepton machine, which will feature electroweak interactions. The LHC collides protons and lead ions, where each hadron consists of three valence quarks, in addition to sea quarks and gluons. The hadron collisions are in reality collisions between these smaller constituents, each of which carries a fraction of the total particle energy. Therefore, a whole distribution of collision energies exists inside the particle detectors, which is beneficial for making new discoveries. The drawback is that it is difficult to perform precision measurements.

Leptons, on the other hand, are fundamental particles. Lepton collisions therefore happen at approximately the same energy, with well defined initial conditions. This makes precision measurements easy, but ideally one wants to set up the machine for a specific collision energy that is already known. Traditionally, high-energy physics has alternated between using hadron colliders and lepton colliders, because of the complementarity between the two. This is therefore a strong motivation to build a lepton collider next. The most mature option today is a collider for electrons and their antiparticle positrons (an e^+e^- collider). This option has two promising, global schemes; namely the International Linear Collider (ILC) and the Compact Linear Collider (CLIC). The former is a design for a 0.25–1 TeV machine with superconducting accelerating cavities, while the latter is a 0.3–3.0 TeV, normal-conducting machine that uses a novel *drive beam* concept for acceleration. Instead of e^+e^- colliders, it is also thinkable to build a muon collider [4]. However, this scheme is not fully mature and requires further research. An example of a feasibility issue is that the muons are unstable and quickly decay into other particles. Therefore, the acceleration must be very fast and bring the muons to a relativistic speed (where time is dilated) before they decay.

One challenge for building an e^+e^- collider is that the particles are extremely light. They lose a significant fraction of their kinetic energy when they change direction at high

energies [5], and this counteracts the acceleration energy given to the particles. This effect is usually referred to as *synchrotron radiation*. To describe this effect in a circular accelerator like the LHC, we look at the energy loss per turn of a particle. When the bending radius ρ_{B} is the same for all bending magnets, the energy loss per turn due to synchrotron radiation can be expressed [5]

$$\Delta\mathscr{E}_{\mathrm{SR}} = \frac{q^2}{3\,\varepsilon_0}\frac{1}{(m_0c^2)^4}\frac{\mathscr{E}^4}{\rho_{\mathrm{B}}}, \tag{1.1}$$

where q is the particle charge, ε_0 is the electric permittivity in vacuum, m_0 is the particle mass, c is the speed of light, and $\mathscr{E}$ is the current particle energy. First of all, from this equation we can see that synchrotron radiation is much more pronounced for electrons and positrons than for heavier particles. Being 1836 times lighter than protons, these particles lose 10^{13} times more energy in one turn. From the fraction $\mathscr{E}^4/\rho_{\mathrm{B}}$ we also see that as the particle energy is increased, one must compensate heavily with the accelerator radius to avoid more energy losses. The Large Electron-Positron (LEP) collider at CERN was close to the limit of tolerable synchrotron radiation losses, and was earlier placed in the same 27 km tunnel where the LHC is today. A higher energy circular machine for e^+e^- collisions would therefore be very large.

To avoid synchrotron radiation at high energies, it is therefore attractive to build a linear e^+e^- collider, where the two particle beams are sent to each side of a straight line, before being accelerated to a high energy and colliding in the middle of the line. This idea is employed in both the ILC and CLIC. The drawback of a linear collider is that the particles only have one chance to collide, whereas in a circular collider they can circulate millions of times through the same collision point. It is therefore important to achieve a high collision rate (luminosity) in the linear collider.

Also, in a linear accelerator the acceleration *gradient* (the acceleration per unit length) is very important, since this directly affects the length of the machine. To achieve a high gradient, CLIC uses a novel two-beam scheme where acceleration energy is extracted from a *drive beam* running in parallel to the main beam. This scheme is used because the high gradient requires a power source with a high frequency and a high peak power, something that is difficult to achieve with traditional methods.

The layout of the whole CLIC machine is shown in Figure 1.1. The electron and positron main beams are generated in the bottom part of the figure, and after manipulation of beam parameters they are sent to the main linacs. Then the two beams are accelerated up to the final energy, and collide in a detector in the middle of the figure. The drive beams are generated in the upper part of the figure, and accelerated to an energy of 2.4 GeV. They are then sent through a *delay loop* and two *combiner rings*, and the function of these will be briefly described in Section 3.2. Finally, the drive beams are sent through each of the *decelerator sectors* in turn, where most of the beam energy is extracted and transferred to the main beams. This thesis concerns energy extraction from the drive beam in CLIC.

1.3 Outline

Chapter 2 of the thesis describes relevant theory for this work. It starts describing a type of *collective effect* in particle beams known as *longitudinal space charge*, that can deteriorate the beam quality. Next follows a description of beam physics in radiofrequency (rf) structures,

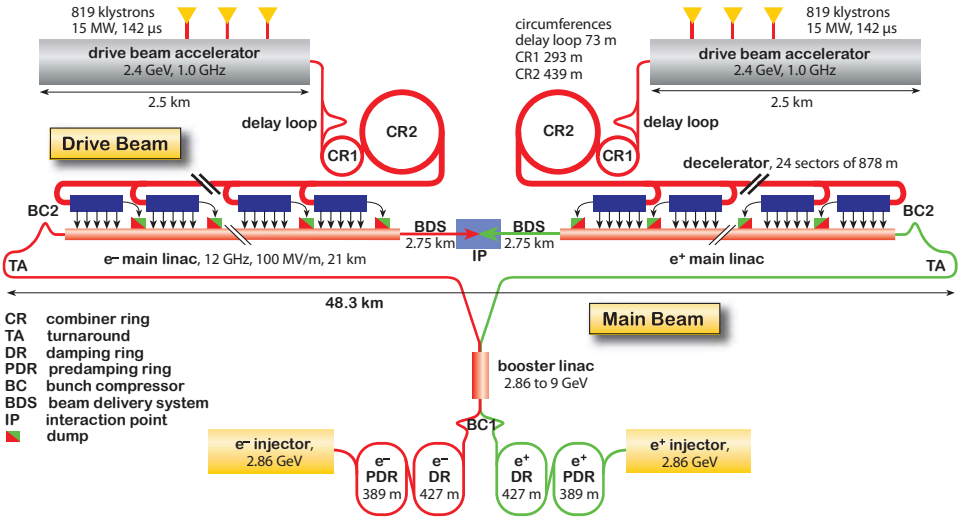

Figure 1.1: CLIC layout for a center-of-mass energy of 3 TeV. The drive beam complexes are shown in the upper part of the picture while the main beam complexes are shown in the lower part.

including the effects on the beam and on the electromagnetic field inside. Finally, transverse beam parameters are explained briefly, before a method for measuring them is explained.

Some theory is also presented in Chapter 3, specific for the CLIC technology, and this includes some new derivations. Firstly, in Section 3.1 we describe the *Power Extraction and Transfer Structure* (PETS), that extracts rf power from the drive beam. This section includes a model for ohmic losses, how the power is generated and the beam is decelerated, and finally how the bunch length and bunch phase affect the efficiency. The chapter also explains how the longitudinal structure of the drive beam is created, before it describes the 1 km long *decelerators* that run in parallel to the main CLIC beams. The prototype decelerator at CERN – where the experiments have been performed – is presented in Chapter 4.

Even though some of the main results of this thesis are presented in the publications in Appendix A, additions to the published results are summarized in Chapters 5 and 6. The former describes measurements on a heavily decelerated drive beam in the CLIC Test Facility 3 at CERN, while the latter describes simulation results on the longitudinal space charge effect in the CLIC drive beam decelerators.

1.4 Acknowledgements

After a three year long project in a big collaboration there is a lot of people I want to thank. First and foremost my supervisors with all of their experience, who could always give useful tips and guide me on the right path. Steffen Döbert has been a major asset with his broad knowledge, good scientific intuition and hands-on experience, and his ability to always find time even with a busy schedule. Erik Adli, even though beeing located almost 10,000 km

away, has still provided good guidance, motivation and explanations. Steinar Stapnes is an excellent catalyst and organizer, and together my three supervisors have completed each other very well.

There are several other people that have contributed to the final results of this work. Either by being involved in the experiments, providing good discussions, or providing tips for continued research, they have been very good resources. For this I want to thank Maja Olvegård, Kyrre Sjøbæk, Yngve Levinsen, Guido Sterbini, Andrea Latina, Roberto Corsini, Daniel Schulte, Frank Tecker, Igor Syratchev, Hamed Shaker, Steven Lund, Esa Paju, Alan Bell and Anne Dabrowski.

I also want to acknowledge the operators of the CLIC Test Faciliy 3, who have worked hard to provide the best conditions for the Test Beam Line experiment. In addition to some already mentioned, this includes Piotr Skowronski, Tobias Persson, Ben Constance, Javier Barranco, Lukas Malina and Luis Quirante.

There are also many other people at CERN that, even though they did not contribute directly to my work, helped making my days in Geneva a memorable experience. In addition to people already mentioned, in a semi-random order thank you Ole, Theo, Erwan, Bart, Viktor, Marlene, Yisel, Rati, Nikos, Annelie, Miriam, Aleksey, David, Michael, Xiaowei, Foteini, Lars, Adam, Diamanto, Alexander, Giulia, Lene, Marion, Hannes, Jochem, Frank, Eduardo, Anna, Andrea, Christos, Matina, Andriy, Helga, Daniel, Glenn, Christoph, Juha, Pieter, Line, Marta, Christina, Brian, Anders, Cian, Marko, Johannes, Øystein, Elisabeth, Jürgen, Patricia, Vetle, Adrian, Jens, Nils and of course my uncle Egil and aunt Danielle (I hope that was everyone).

Last but not least, my ever-supporting family in Norway! Even though I have not seen you often in the real life, Skype has been great for keeping contact. You have helped me with numerous practical issues. Kjell, Turid, and Lars – thank you for being there!

Chapter 2

Accelerator physics

This chapter introduces some theory that is used generally in accelerator physics and is used in this work. Firstly, Section 2.1 describes the longitudinal space charge force, that elongates particle bunches of the same charge. This effect has been of concern for CLIC because of the strict tolerance on the drive beam bunch length. Section 2.2 explains the physics of radiofrequency structures and the beam behavior inside. This is needed in order to understand Power Extraction and Transfer Structures that are at the core of this work, and the theory will be expanded in Chapter 3. Finally, Section 2.3 describes the quadrupole scan method for measuring transverse beam parameters, which is used in the results in Chapter 5.

Throughout the thesis, quantities per unit length will be denoted with a prime (').

2.1 Longitudinal space charge

A particle beam will in most cases consist of charged particles. It can therefore be accelerated using electric fields, and guided around the accelerator by magnets. To get the same electromagnetic force on all particles they also have the same charge, for example electrons for the CLIC drive beam. Because the particles have the same charge, they are forced apart because of the electrostatic Coulomb force. When many particles are packed together in a stationary bunch, the force is very strong, and if placed inside a container like a vacuum pipe the particles would eventually get lost in the pipe wall.

If the bunch is set in motion however, it will also have a magnetic field because of Faraday's law of induction. At high velocities approaching the speed of light, the magnetic field will tend to cancel most of the force from the electric field, so that the particles can still be packed together. In proton accelerators, it is common to use *radiofrequency quadrupoles* that can accelerate the particle bunches to a high velocity while providing focusing at the same time. The electromagnetic self field produced by a bunch is called *space charge*, and this effect is often separated into transverse and longitudinal forces.

For a continuous beam, the field is purely transverse. For a bunched beam however, as used in today's high-energy accelerators, there are both transverse and longitudinal forces. In this thesis the focus will be on longitudinal effects only. As will be seen later, space charge is normally not a concern for high-energy machines such as CLIC. However, because of the strict bunch length tolerance of the drive beam, it has been a concern that longitudinal space charge may still play a role.

For looking at longitudinal space charge analytically, let us follow the derivation in [6] and

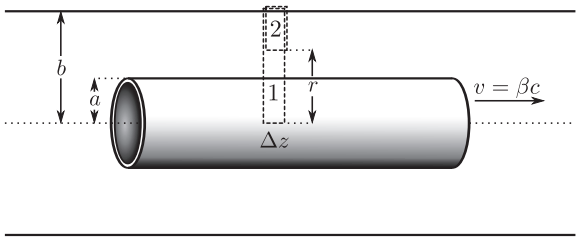

Figure 2.1: Ring bunch used for the analytical model of longitudinal space charge. Faraday's law is applied to the closed circuits '1' and '2'.

consider a 'ring bunch' as shown in Figure 2.1. The ring has a radius of $r = a$ and is placed in the middle of a beam pipe of radius b. When the charge distribution is $e\lambda(z)$, where z is the longitudinal coordinate relative to the bunch motion, the radial electric field inside and outside of the bunch is approximately given by

$$E_r = \begin{cases} 0 & \text{if } r < a, \\ \frac{e}{2\pi\varepsilon_0 r}\lambda(z) & \text{if } a < r < b, \end{cases} \tag{2.1}$$

where ε_0 is the electric permittivity in vacuum and r is the radius. The field outside the bunch is approximated by the field from a wire charge, and for a bunch of length l the condition $l \gg b/\gamma$ must therefore be fulfilled. Here γ is the relativistic Lorentz factor. The magnetic field is simply $B_\theta = \frac{\beta}{c}E_r$. To calculate the longitudinal electric field, we apply Faraday's law

$$\oint \vec{E} \cdot \mathrm{d}\vec{l} = -\int \frac{\partial \vec{B}}{\partial t} \cdot \mathrm{d}\vec{A} \tag{2.2}$$

to the closed circuit named '1' in Figure 2.1,

$$E_z \Delta z + \frac{e}{2\pi\varepsilon_0}\left[\lambda(z+\Delta z) - \lambda(z)\right]\int_a^b \frac{\mathrm{d}r}{r} = -\frac{e\beta}{2\pi\varepsilon_0 c}\frac{\partial\lambda(z)}{\partial t}\Delta z \int_a^b \frac{\mathrm{d}r}{r}. \tag{2.3}$$

Dividing by Δz and multiplying the right hand side by $\partial z/\partial z$, we have an expression for the longitudinal electric field inside the bunch,

$$E_z = -\frac{e}{2\pi\varepsilon_0}\left[\frac{\lambda(z+\Delta z) - \lambda(z)}{\Delta z} + \frac{\beta}{c}\frac{\partial\lambda(z)}{\partial t}\frac{\partial z}{\partial z}\right]\int_a^b \frac{\mathrm{d}r}{r}. \tag{2.4}$$

The first term inside the brackets is simply the definition of the spatial derivative of $\lambda(z)$. In the second term we have $\partial z/\partial t = -\beta c$. We can therefore simplify the expression as

$$E_z = -\frac{e}{2\pi\varepsilon_0\gamma^2}\frac{\partial\lambda(z)}{\partial z}\ln\frac{b}{a}. \tag{2.5}$$

The longitudinal electric field outside the bunch can easily be found by doing the same derivation on circuit '2' in Figure 2.1. The only difference is the limit of integration r, which gives the result

$$E_z = -\frac{e}{2\pi\varepsilon_0\gamma^2}\frac{\partial\lambda(z)}{\partial z}\ln\frac{b}{r}. \tag{2.6}$$

This field component vanishes at the conducting beam pipe $r = b$, as it should. Physically, the space charge force comes from an imbalance between charge in front of and behind the longitudinal position considered. If there is more charge in front, $\partial\lambda(z)/\partial z$ is positive, which leads to a retarding force. Similarly, the force is accelerating if there is more charge behind. Therefore, longitudinal space charge tends to elongate the bunch, as expected from the Coulomb force.

Note that Equations (2.5) and (2.6) both contain the factor $1/\gamma^2$, which means that there is a strong suppression of the space charge effect for highly relativistic beams. One can also extend the analysis to radial bunch distributions more general than the ring bunch. The result [6] is still that the longitudinal electric field scales as $1/\gamma^2$.

2.2 Radiofrequency structures with beam physics

This section explains concepts in radiofrequency technology and beam behavior that are important for the understanding of PETS. We will first define fundamental quantities in use, before moving on to a description of beam loading and wake fields. Finally, we will derive the energy loss of a particle bunch in a structure, which will be of importance in later chapters.

2.2.1 Fundamental quantities in radiofrequency technology

In high energy particle accelerators, radiofrequency (rf) technology is utilized to efficiently accelerate bunches of particles. In this section we will introduce some key parameters of rf technology that will be of importance later. All of these quantities are properties of the rf structure geometry. Based on the design of the structure, it will have a certain number of resonating modes of different strength, and each individual mode will be denoted by the index n.

The *shunt impedance* of a structure measures the effectiveness of producing a field on the axis, per unit power loss in the structure walls [7]. This quantity increases linearly with the structure length L_S, and it is therefore convenient to use the *shunt impedance per unit length* R'_n. If E_n is the longitudinal electric field of the mode travelling wave, and $\mathcal{P}_n$ is the power dissipated in the walls due to electrical resistivity, the shunt impedance per unit length is defined as

$$R'_n \equiv \frac{E_n^2}{\mathcal{P}_n/L_\mathrm{S}}. \tag{2.7}$$

Another important property of a mode in a cavity is its resonator *quality factor* Q_n. A high quality factor corresponds to a mode that will ring inside the structure for a long time with only small losses of field energy. The quality factor depends on the mode frequency ω_n, and if $\mathcal{E}_n$ is the stored field energy of the mode it can be expressed

$$Q_n \equiv \frac{\omega_n \mathcal{E}_n}{\mathcal{P}_n}. \tag{2.8}$$

For a structure with a high Q_n fundamental mode, the mode impedance is proportional to the quantity R'_n/Q_n, which is a fundamental design parameter when designing RF structures. Combining equations (2.7) and (2.8), we get

$$R'_n/Q_n = \frac{E_n^2 L_\mathrm{S}}{\omega_n \mathcal{E}_n} = \frac{E_n^2}{\omega_n \mathcal{E}'_n}, \tag{2.9}$$

where $\mathcal{E}'_n = \mathcal{E}_n/L_\mathrm{S}$ is the stored field energy per unit length.

2.2.2 Beam loading

When passing through an RF structure, a particle bunch absorbs some of the energy of the field due to its electric charge. However, as described in Section 2.1 the bunch also has a self-field, which will act on the structure. The beam-induced field adds vectorially to the cavity field and modifies the amplitude and phase. This effect is known as *beam loading*.

Consider a bunch that passes through an unexcited cavity. It will excite the cavity with a retarding cavity voltage $-V_{\mathrm{b},n}$ in the mode n. However, only half of this voltage is seen by the bunch itself, because the voltage is being established while the bunch is passing through [7]. This is called the *fundamental theorem of beam loading*, and the energy loss of the bunch of charge q_b is therefore $-q_\mathrm{b}V_{\mathrm{b},n}/2$. The stored energy in the cavity will be proportional to the voltage squared through a proportionality constant α, and is therefore $\mathcal{E}_n = \alpha V_{\mathrm{b},n}^2$. Because of conservation of energy, the bunch energy loss must be equal to the stored energy in the cavity, and we have

$$\mathcal{E}_n = \alpha V_{\mathrm{b},n}^2 = q_\mathrm{b}\frac{V_{\mathrm{b},n}}{2}. \tag{2.10}$$

For travelling wave structures it is more convenient to use the electric field E_n. Since the bunch voltage is $V_{\mathrm{b},n} = E_n L_\mathrm{S}$ we can instead write Equation. (2.10) as

$$\mathcal{E}_n = \alpha E_n^2 L_\mathrm{S}^2 = q_\mathrm{b}\frac{E_n L_\mathrm{S}}{2}. \tag{2.11}$$

Solving for E_n, we get $E_n = q_\mathrm{b}/2\alpha L_\mathrm{S}$, and by substituting this relation into Equation (2.11) we have

$$\mathcal{E}_n = \alpha E_n^2 L_\mathrm{S}^2 = \frac{q_\mathrm{b}^2}{4\alpha} = k_n q_\mathrm{b}^2, \tag{2.12}$$

where we have defined the loss parameter $k_n \equiv 1/4\alpha$. Physically, the loss factor for a given mode is the proportionality between the energy transferred to the structure and the squared bunch charge. In terms of the loss parameter we can rewrite Equation (2.12)

$$\mathcal{E}_n = \alpha E_n^2 L_\mathrm{S}^2 = \frac{E_n^2 L_\mathrm{S}^2}{4k_n}, \tag{2.13}$$

which, when solved for the loss parameter divided by the structure length, gives

$$\frac{k_n}{L_\mathrm{S}} = \frac{E_n^2 L_\mathrm{S}}{4\,\mathcal{E}_n} \tag{2.14}$$

The left hand side of Equation (2.14) is the loss parameter per unit length k_n', while the stored energy per unit length $\mathcal{E}_n' = \mathcal{E}_n/L_\mathrm{S}$ has been introduced before. We therefore write

$$k_n' = \frac{E_n^2}{4\,\mathcal{E}_n'}. \tag{2.15}$$

This relation is very similar to Equation (2.9), so in terms of familiar structure parameters we can write

$$k_n' = \frac{1}{4}(R_n'/Q_n)\,\omega_n. \tag{2.16}$$

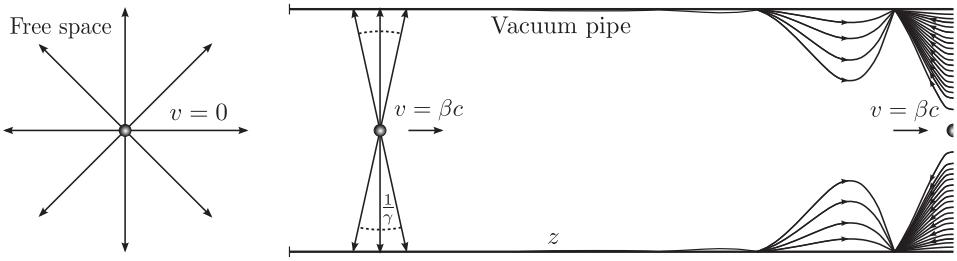

Figure 2.2: Wake field effects from a particle. Left: The free space electrostatic field of a stationary particle. Middle: The electric field of a relativistic particle passing through a perfectly conducting beam pipe. Right: The monopole wake field of an ultrarelativistic particle passing through a resistive beam pipe (picture inspired by [6]). The monopole wake is normally dominant for longitudinal effects.

2.2.3 Wakefields

From the previous discussion, one may think that the field set up by a passing bunch in a cavity is a static one, however in reality the field will dynamically change. This is because of the phenomenon known as a *wakefield*, that is related to beam loading. A relativistic bunch leaves an electromagnetic wake behind it, just like a boat passing through water. We will here explain wakefields mainly from the case of a bunch passing through a resistive vacuum pipe.

Consider first a point particle in free space. Its electric field distribution is well known from electrostatics, and is shown to the left in Figure 2.2. Once the particle starts to move, the field will no longer be equal in all directions, but will instead be length contracted. The angular spread of the field is proportional to $1/\gamma$, where γ is the relativistic Lorentz factor, and when the particle speed approaches the speed of light the field will approach an infinitely thin pancake distribution [6].

If the particle passes through a perfectly conducting vacuum pipe, the length contracted field lines will simply be truncated at the pipe walls if the particle travels on the axis [6]. The situation with a relativistic particle inside a vacuum pipe is shown in the middle in Figure 2.2. In this case, image currents will travel on the vacuum pipe along with the particle. However, if the beam pipe is not perfectly conducting, the image currents will experience an impedance, and so will the particle itself due to its electromagnetic interaction with the pipe. This leads to the characteristic wake field that trails the particle, and is shown to the right in Figure 2.2. Calculation of wake fields is complicated and is normally performed by simulation codes.

A particle or a particle bunch can have different multipole moments dependent on its position and charge distribution. For the simple case of a point particle or a ring bunch on axis, it will only have a monopole moment. This leades to a corresponding *monopole wake*. The wakefield from this moment in constant in the radial direction and is only dependent on the relative longitudinal distance from the particle or bunch. The monopole wake is often the strongest and is then dominant for longitudinal effects [6]. The field distribution to the right in Figure 2.2 is that of the monopole wake. As seen from the field lines in the figure, the field immediately behind the bunch leads to a retarding force. This is proportional to half the voltage of the bunch, in the same way as in Equation (2.10).

More general bunch distributions and off-axis bunches or particles will also comprise higher-order moments. Normally, the dominant moment is the *dipole moment*, and the corresponding dipole wake is usually dominant for transverse effects [6]. This can be detrimental to the beam quality, since particles e.g. can be kicked out from the axis. In this work we will however focus on the monopole wake, which is important for the function of PETS.

Another cause of wakefields is when a bunch passes through a changing vacuum pipe cross-section, for instance in an accelerating cavity. The field generated inside a cavity can be described in terms of a superposition of cavity modes, each with its own mode frequency ω_n and R'_n/Q_n, and the energy deposited into a given mode is given by Equation (2.12).

Wake field effects are often described in terms of *wake functions* in the time domain, or equivalently in terms of *impedances* in the frequency domain. The two are Fourier transform pairs, so that one of them gives the full information about the other. The longitudinal monopole impedance $Z_0^{\parallel}$ of a cavity mode n can often be modeled as a parallel LRC circuit [6],

$$\frac{1}{Z_0^{\parallel}\Big|_n} = \frac{1}{R_n} + \frac{1}{\omega L_n} - i\omega C_n, \tag{2.17}$$

where R_n is the (resistive) shunt impedance, L_n is an inductance and C_n is a capacitance. For a mode with a high quality factor $Q_n = R_n\sqrt{C_n/L_n}$, Equation (2.17) can be simplified by letting $Q_n \to \infty$ and $R_n \to \infty$ while keeping R_n/Q_n fixed. Including all modes, we have

$$\text{Re } Z_0^{\parallel}(\omega) = 2\pi \sum_n k_n \left[\delta(\omega - \omega_n) + \delta(\omega + \omega_n)\right], \tag{2.18a}$$

$$\text{Im } Z_0^{\parallel}(\omega) = 2 \sum_n k_n \left(\frac{1}{\omega - \omega_n} + \frac{1}{\omega + \omega_n}\right). \tag{2.18b}$$

The Fourier transform of Equation (2.18) is the longitudinal monopole wake function $W_0^{\parallel}(z)$, which describes the shock response of the environment to a δ-function bunch,

$$W_0^{\parallel}(z) = \begin{cases} 2\sum_n k_n \cos\left(\frac{\omega_n}{c} z\right), & \text{for } z < 0, \\ \sum_n k_n, & \text{for } z = 0, \\ 0, & \text{for } z > 0. \end{cases} \tag{2.19}$$

As can be seen from Equation (2.19), because of causality the wake function only has a non-zero value at the location of the particle or behind it, where $z \leq 0$. Because of the high quality factor of the structure, the wake function for a single mode is simply modeled as a cosine. For a structure with a low Q_n, there would also be attenuation of the wake function behind the particle.

Physically, for a witness particle a distance z behind the driving bunch, the wake function in Equation (2.19) describes the average force the witness particle experiences per unit length when travelling through the cavity, normalized by the charge of both particles. The electric field experienced by a witness bunch of charge q_b trailing a point-like bunch is then $q_\text{b} W_0^{\parallel}(z)$.

2.2.4 Energy loss of a bunch in a cavity

We will now look at the energy loss of a bunch in a cavity, which will be used later to describe Power Extraction and Transfer Structures (PETS).

As described in the previous section, the wake function in Equation (2.19) describes the impulse response of a cavity when excited by a δ-function bunch. Real particle bunches will have a finite longitudinal length, however, and the phases of particles at different longitudinal positions will cause destructive interference. Therefore the energy lost by such a bunch will get smaller if the bunch is longer. Similarly to a linear time-invariant system, the produced wake field can be described by a convolution of the wake function by the charge distribution of the bunch. The effective energy loss is also affected by the location that the bunch sees the wake field, so the result of the convolution needs to be multiplied by the charge distribution and integrated over the longitudinal coordinate.

Let us consider a normalized charge distribution $q_\mathrm{b}\lambda(z)$ so that $\int_{-\infty}^{\infty}\lambda(z)\,\mathrm{d}z = 1$. The energy loss is then given by [6]

$$\begin{aligned}\Delta\mathscr{E} &= -\int_{-\infty}^{\infty} q_\mathrm{b}\lambda(z)\left[q_\mathrm{b}\lambda(z) * W_0^{\parallel}(z)\right]\mathrm{d}z \\ &= -q_\mathrm{b}^2\int_{-\infty}^{\infty}\lambda(\tilde{z})\int_{\tilde{z}}^{\infty}\lambda(z)W_0^{\parallel}(\tilde{z}-z)\,\mathrm{d}z\,\mathrm{d}\tilde{z}.\end{aligned} \tag{2.20}$$

We can equivalently express this in the frequency domain by using the impedance. Only the real part of the impedance will contribute to the energy loss, so we get

$$\Delta\mathscr{E} = -\frac{q_\mathrm{b}^2}{2\pi}\int_{-\infty}^{\infty}\left|\int_{-\infty}^{\infty}\lambda(z)e^{-i\omega z/c}\mathrm{d}z\right|^2 \mathrm{Re}\; Z_0^{\parallel}(\omega)\,\mathrm{d}\omega. \tag{2.21}$$

We will in the following focus on a single mode, that has a resonance frequency $\omega_n = \omega_\mathrm{r}$. By using the real impedance from Equation (2.18), Equation (2.21) then becomes

$$\Delta\mathscr{E} = -q_\mathrm{b}^2 k_n\int_{-\infty}^{\infty}\left|\int_{-\infty}^{\infty}\lambda(z)e^{-i\omega z/c}\mathrm{d}z\right|^2 \left[\delta(\omega-\omega_\mathrm{r})+\delta(\omega+\omega_\mathrm{r})\right]\mathrm{d}\omega, \tag{2.22}$$

which because of the sifting property of the delta functions is equivalent to

$$\Delta\mathscr{E} = -q_\mathrm{b}^2 k_n\left|\int_{-\infty}^{\infty}\lambda(z)e^{-i\omega_\mathrm{r} z/c}\mathrm{d}z\right|^2 - q_\mathrm{b}^2 k_n\left|\int_{-\infty}^{\infty}\lambda(z)e^{i\omega_\mathrm{r} z/c}\mathrm{d}z\right|^2. \tag{2.23}$$

The two integrals will be complex conjugates of each other, and their absolute values will thus be equal. To prove this, we can use Euler's formula together with the expansion $|a+b|^2 = |a|^2 + 2\,\mathrm{Re}\,a\bar{b} + |b|^2$ of two complex numbers a and b, where $\bar{b}$ denotes the complex conjugate of b. For the first integral we get

$$\begin{aligned}\left|\int_{-\infty}^{\infty}\lambda(z)e^{-i\omega_\mathrm{r} z/c}\mathrm{d}z\right|^2 &= \left|\int_{-\infty}^{\infty}\lambda(z)\left[\cos\left(\frac{\omega_\mathrm{r}}{c}z\right) - i\sin\left(\frac{\omega_\mathrm{r}}{c}z\right)\right]\mathrm{d}z\right|^2 \\ &= \left|\int_{-\infty}^{\infty}\lambda(z)\cos\left(\frac{\omega_\mathrm{r}}{c}z\right)\mathrm{d}z\right|^2 + \left|\int_{-\infty}^{\infty}\lambda(z)\sin\left(\frac{\omega_\mathrm{r}}{c}z\right)\mathrm{d}z\right|^2 \\ &\quad + 2\mathrm{Re}\left\{i\left[\int_{-\infty}^{\infty}\lambda(z)\cos\left(\frac{\omega_\mathrm{r}}{c}z\right)\mathrm{d}z\right]\left[\int_{-\infty}^{\infty}\lambda(z)\sin\left(\frac{\omega_\mathrm{r}}{c}z\right)\mathrm{d}z\right].\right\}\end{aligned} \tag{2.24}$$

The last term (inside the real value) is completely imaginary, because both integrals are real. Since it does not have a real part this term is therefore equal to zero. One can do a similar

expansion of the second integral in Equation (2.23) and get the same result. The energy loss of the bunch can therefore be written

$$\begin{aligned}\Delta\mathscr{E} &= -2q_{\mathrm{b}}^2 k_n \left| \int_{-\infty}^{\infty} \lambda(z) e^{-i\omega_{\mathrm{r}} z/c} \mathrm{d}z \right|^2 \\ &= -2q_{\mathrm{b}}^2 k_n F^2 \left\{\lambda(z)\right\},\end{aligned} \tag{2.25}$$

where we have introduced a functional called the *charge distribution form factor*, that will be elaborated on in later chapters,

$$F\left\{\lambda(z)\right\} \equiv \left| \int_{-\infty}^{\infty} \lambda(z) e^{-i\omega_{\mathrm{r}} z/c} \mathrm{d}z \right|. \tag{2.26}$$

This is the magnitude of the Fourier transform of the charge distribution evaluated at the mode frequency ω_{r}. Because of normalization we have $0 \leq F\left\{\lambda(z)\right\} \leq 1$. For symmetric charge distributions the form factor can be simplified as the cosine transform

$$F\left\{\lambda(z)\right\} = \int_{-\infty}^{\infty} \lambda(z) \cos\left(\frac{\omega_{\mathrm{r}}}{c} z\right) \, \mathrm{d}z, \tag{2.27}$$

where the modulus has been omitted because of the integration of two real functions.

2.3 Measuring transverse emittance

A particle bunch will have a certain size, and for Gaussian bunches the size in each of the three dimensions can be expressed by the standard deviations σ_x, σ_y and σ_z. For an accelerator with linear optics[1], and without dispersion and chromaticity, the transverse beam sizes can be expressed $\sigma_u = \sqrt{\varepsilon_u \beta_u}$, where u can be either x or y. Here, the beta functions β_u are a property of the accelerator optics, and depend on the focusing strength of the quadrupole magnets.

The quantities ε_u are the transverse emittances, that are properties of the beam itself. It is common to use the phase spaces (x, x') and (y, y') for particles in the bunch. Then, the emittance for one of the transverse dimensions will be proportional to the area of an ellipse in the phase space. This phase space area stays constant throughout the accelerator as long as the beam energy does not change or if there are nonlinear effects. The shape of the ellipse will however change depending on the focusing.

When the beam energy increases, the transverse phase spaces decrease due to *adiabatic damping*. This is due to Liouville's theorem, which states that a phase space element $p\Delta u \Delta u'$ will remain constant, where p is the momentum. As the beam momentum increases, the other quantities must be reduced accordingly. It is convenient to define *normalized emittances* $\varepsilon_{\mathrm{N}_u} = \beta\gamma\varepsilon_u$ that stay constant even with changing beam energy. Note that β and γ are here relativistic quantities that are not related to the beta functions. The non-normalized emittance is often referred to as the *geometric emittance*.

[1] This includes dipole and quadrupole magnets. However, it is not possible to create perfect magnets, so they will in reality also have small components that are sextupolar, octupolar and higher.

2.3.1 Beam transport

Together with the lattice beta functions mentioned above, two related quantities are also used, which are $\alpha_u = -\beta_u'/2$ and $\gamma_u = (1+\alpha_u^2)/\beta_u$. These quantities with the subscript u are not related to the relativistic parameters, and the confusing choice of letters is of historical origin.

The three parameres α_u, β_u and γ_u are together referred to as the *Twiss parameters*. Together with the emittance they make up the beam matrix

$$\Sigma_{u0} \equiv \varepsilon_u \begin{pmatrix} \beta_{u0} & -\alpha_{u0} \\ -\alpha_{u0} & \gamma_{u0} \end{pmatrix} \tag{2.28}$$

for a given longitudinal point '0' in the lattice, and for one of the transverse planes. Note that from the way this matrix is defined, together with the definitions of the Twiss parameters, the determinant of the matrix is equal to ε_u^2.

Another useful quantity is the transfer matrix $\mathcal{M}$ of a given lattice. This describes how the particle position and transverse velocity change when passing through. As an example, the transfer matrix of a single focusing quadrupole magnet is given by

$$\mathcal{M}_{\mathrm{F}} = \begin{pmatrix} \cos\sqrt{k_{\mathrm{F}}}\, l_{\mathrm{F}} & \frac{1}{\sqrt{k_{\mathrm{F}}}} \sin\sqrt{k_{\mathrm{F}}}\, l_{\mathrm{F}} \\ -\sqrt{k_{\mathrm{F}}} \sin\sqrt{k_{\mathrm{F}}}\, l_{\mathrm{F}} & \cos\sqrt{k_{\mathrm{F}}}\, l_{\mathrm{F}} \end{pmatrix}, \tag{2.29}$$

where k_{F} is the focusing strength of the magnet and l_{F} is its length. The transfer matrix in Equation (2.29) can often be simplified if the focal length f of the magnet is long compared to the length of the magnet itself, $f = 1/k_{\mathrm{F}} l_{\mathrm{F}} \gg l_{\mathrm{F}}$. Then, we can let $l_{\mathrm{F}} \to 0$, perform Maclaurin expansions while only keeping linear terms, and get

$$\mathcal{M}_{\mathrm{F}} \approx \begin{pmatrix} 1 & 0 \\ -k_{\mathrm{F}} l_{\mathrm{F}} & 1 \end{pmatrix}. \tag{2.30}$$

For an initial vector $\vec{u}_0 = (u_0, u_0')$, the position and transverse velocity after the quadrupole are given by multiplication with the transfer matrix, $\vec{u}_1 = \mathcal{M}_{\mathrm{F}} \vec{u}_0$. One can also construct a transfer matrix for a larger lattice, by multiplying several individual transfer matrices.

The Twiss parameters can also be transported in a similar way. For an arbitrary transfer matrix $\mathcal{M}$ and an initial beam matrix Σ_0, the new beam matrix Σ_1 is found by the following relation,

$$\Sigma_1 = \mathcal{M} \Sigma_0 \mathcal{M}^{\mathrm{T}}. \tag{2.31}$$

2.3.2 Quadrupole scans

We will now present a method for measuring the emittance, together with the Twiss parameters, which is known as *quadrupole scans* [8]. The idea is to vary the strength of a quadrupole magnet and then measure the effect on the beam size on a downstream measurement screen.

Consider a single quadrupole magnet and a measurement screen, with an arbitrary lattice in between, as in Figure 2.3. Sometimes two quadrupoles are used in this method, but for simplicity we will focus on one. Let the transfer matrix of the arbitrary lattice be $\mathcal{M}_{\mathrm{rest}}$, with elements m_{11}, m_{12}, m_{21} and m_{22} for one transverse plane. Then, if we assume the thin-lens approximation in Equation (2.30) the total transfer matrix can be expressed

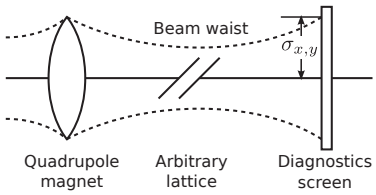

Figure 2.3: Setup for a quadrupole scan, where the variation of a quadrupole magnet is compared to beam size measurements downstream.

$$\mathcal{M} = \mathcal{M}_{\text{rest}}\mathcal{M}_{\text{F}} = \begin{pmatrix} m_{11} & m_{12} \\ m_{21} & m_{22} \end{pmatrix} \begin{pmatrix} 1 & 0 \\ -k_{\text{F}} l_{\text{F}} & 1 \end{pmatrix} = \begin{pmatrix} m_{11} - k_{\text{F}} l_{\text{F}} m_{12} & m_{12} \\ m_{21} - k_{\text{F}} l_{\text{F}} m_{22} & m_{22} \end{pmatrix} \tag{2.32}$$

This can be used together with Equation (2.31) to transport Twiss parameters to the location of the screen. There will be many terms involved on the right hand side, but for our purposes we only need the (1,1) elements of this matrix equation,

$$\begin{aligned} \varepsilon_{u1}\beta_{u1} = \varepsilon_{u0}\beta_{u0} m_{12}^2 l_{\text{F}}^2 k_{\text{F}}^2 + 2\varepsilon_{u0} l_{\text{F}} (m_{12}^2 \alpha_{u0} - m_{11} m_{12} \beta_{u0}) k_{\text{F}} \\ + m_{11}^2 \varepsilon_{u0}\beta_{u0} - 2 m_{11} m_{12} \varepsilon_{u0}\alpha_{u0} + m_{12}^2 \varepsilon_{u0}\gamma_{u0} \end{aligned} \tag{2.33}$$

The term on the left hand side is the square of the beam size at the measurement screen since $\sigma_{1u} = \sqrt{\varepsilon_{1u}\beta_{1u}}$. Therefore, as seen from this equation the square of the beam size will be a quadratic polynomial in the quadrupole focusing strength k_{F}.

Several points are measured in a quadrupole scan for different focusing strengths. For each point, a Gaussian curve can be fitted to the transverse beam profile, where each fitted standard deviation gives an estimation of the beam size σ_{1u}. Then, the collection of focusing strengths k_{F} and squared beam sizes can be fitted with a parabola, according to Equation (2.33). One parametrization for the fit is

$$\begin{aligned} \Sigma_{u1}|_{11} &= A(k_{\text{F}} - B)^2 + C \\ &= A k_{\text{F}}^2 - 2AB k_{\text{F}} + C + AB^2 \end{aligned} \tag{2.34}$$

Equating coefficients from Equations (2.33) and (2.34), and using elements from the beam matrix in Equation (2.28), we have

$$A = m_{12}^2 l_{\text{F}}^2 \Sigma_{u0,11} \tag{2.35a}$$

$$-2AB = -2 m_{12}^2 l_{\text{F}} \Sigma_{u0,12} - 2 m_{11} m_{12} l_{\text{F}} \Sigma_{u0,11} \tag{2.35b}$$

$$C + AB^2 = m_{11}^2 \Sigma_{u0,11} + 2 m_{11} m_{12} \Sigma_{u0,12} + m_{12}^2 \Sigma_{u0,22} \tag{2.35c}$$

Solving for the beam matrix elements, we get

$$\Sigma_{u0,11} = \frac{A}{m_{12}^2 l_\mathrm{F}^2} \tag{2.36a}$$

$$\begin{aligned}\Sigma_{u0,12} &= \frac{AB}{m_{12}^2 l_\mathrm{F}} - \frac{m_{11}}{m_{12}}\Sigma_{u0,11} \\ &= \frac{AB}{m_{12}^2 l_\mathrm{F}} - \frac{A m_{11}}{m_{12}^3 l_\mathrm{F}^2}\end{aligned} \tag{2.36b}$$

$$\begin{aligned}\Sigma_{u0,22} &= \frac{1}{m_{12}^2}\left(C + AB^2 - m_{11}^2\Sigma_{u0,11} - 2m_{11}m_{12}\Sigma_{u0,12}\right) \\ &= \frac{C}{m_{12}^2} + \frac{AB^2}{m_{12}^2} - \frac{A}{l_\mathrm{F}^2}\frac{m_{11}^2}{m_{12}^4} - \frac{2AB}{l_\mathrm{F}}\frac{m_{11}}{m_{12}^3} + \frac{2A}{l_\mathrm{F}^2}\frac{m_{11}^2}{m_{12}^4} \\ &= \frac{C}{m_{12}^2} + \frac{AB^2}{m_{12}^2} + \frac{A}{l_\mathrm{F}^2}\frac{m_{11}^2}{m_{12}^4} - \frac{2AB}{l_\mathrm{F}}\frac{m_{11}}{m_{12}^3}\end{aligned} \tag{2.36c}$$

As mentioned earlier, the determinant of the beam matrix is equal to the squared emittance, so that $\varepsilon_u = \sqrt{\det \Sigma_{u0}}$. The determinant is

$$\begin{aligned}\det \Sigma_{u0} &= \Sigma_{u0,11}\Sigma_{u0,22} - \Sigma_{u0,12}^2 \\ &= \frac{AC}{m_{12}^4 l_\mathrm{F}^2} + \cancel{\frac{A^2B^2}{l_\mathrm{F}^2 m_{12}^4}} + \cancel{\frac{A^2}{l_\mathrm{F}^4}\frac{m_{11}^2}{m_{12}^6}} - \cancel{\frac{2A^2B}{l_\mathrm{F}^3}\frac{m_{11}}{m_{12}^5}} - \cancel{\frac{A^2B^2}{l_\mathrm{F}^2 m_{12}^4}} + \cancel{\frac{2A^2B}{l_\mathrm{F}^3}\frac{m_{11}}{m_{12}^5}} - \cancel{\frac{A^2}{l_\mathrm{F}^4}\frac{m_{11}^2}{m_{12}^6}},\end{aligned} \tag{2.37}$$

thus the emittance can be found from the parameters of the fit as

$$\varepsilon_u = \frac{\sqrt{AC}}{l_\mathrm{F} m_{12}^2}. \tag{2.38}$$

The Twiss parameters can then be found from the elements of the beam matrix in Equation (2.28). Using Equations (2.36) and (2.38), we have

$$\beta_{u0} = \frac{\Sigma_{u0,11}}{\varepsilon_u} = \frac{1}{l_\mathrm{F}}\sqrt{\frac{A}{C}}, \tag{2.39a}$$

$$\alpha_{u0} = -\frac{\Sigma_{u0,21}}{\varepsilon_u} = \sqrt{\frac{A}{C}}\left(\frac{1}{l_\mathrm{F}}\frac{m_{11}}{m_{12}} - B\right), \tag{2.39b}$$

$$\gamma_{u0} = \frac{\Sigma_{u0,22}}{\varepsilon_u} = l_\mathrm{F}\sqrt{\frac{C}{A}} + B^2 l_\mathrm{F}\sqrt{\frac{A}{C}} + \frac{1}{l_\mathrm{F}}\frac{m_{11}^2}{m_{12}^2}\sqrt{\frac{A}{C}} - 2B\frac{m_{11}}{m_{12}}\sqrt{\frac{A}{C}}. \tag{2.39c}$$

A beam with a finite energy spread will experience chromaticity, which causes different beam focusing depending on the energies of the individual particles. The focal length of the quadrupole will therefore be smeared out, and the measured beam size will be larger than for the monoenergetic beam. In many cases, the energy spread will be small enough that chromaticity has a negligible impact on quadrupole scans. However, the CLIC drive beam has a large energy spread, especially at the end of the decelerator. The same applies for the CTF3. Therefore, chromaticity needs to be taken into account, and a model including this effect is described in detail in [9].

Chapter 3

Two-beam acceleration in CLIC

As mentioned in Chapter 1, in order to reach high energies with electrons and positrons one should build a linear collider, because the energy loss is too large when the path of these particles is bent. For a linear collider of a given collision energy, a high *accelerating gradient* is wanted in order to reduce the required length of the machine. Radiofrequency accelerators can normally achieve higher gradients for higher acceleration frequencies, and for CLIC the frequency is chosen to be 12 GHz [10]. At such a high frequency one needs a high peak power over a short pulse, and this cannot be reached efficiently with klystrons[1]. Therefore, in order to reach a high 12 GHz gradient efficiently, CLIC uses a novel two-beam scheme. This chapter presents some basic principles of two-beam technology.

Wakefields, briefly described in Section 2.2.3, is a collective effect that can be detrimental to the beam quality. This is because the strong electromagnetic fields can negatively affect the tail of the leading bunch itself or the following bunches. However, in some cases it is possible to exploit wake fields as a power source that can be used to accelerate another beam. This concept is utilized in CLIC and is called two-beam acceleration.

This chapter starts by describing Power Extraction and Transfer Structures (PETS), including a model for ohmic losses, how the high power is generated, how the beam is decelerated and how the bunch phase affects the efficiency of the structures. In Section 3.2 the concept and implications of bunch combination of a drive beam is discussed, which is necessary in order to reach high power in the PETS. Finally, Section 3.3 gives a brief presentation of the CLIC decelerators.

3.1 Power Extraction and Transfer Structures

At the heart of the two-beam scheme is the PETS [10, 11, 12], which is used to extract electromagnetic energy from the drive beam. Differently than in earlier work, most of the physics is explained in terms of the energy loss of single bunches, first derived in Section 2.2.4. This is necessary later for the derivation in Section 3.1.5, which looks at how the bunch phase affects the power production.

[1] If a pulse compressor is used together with the klystron, a higher peak power can be reached, but a large part of the power is lost.

3.1.1 Ohmic losses

Before deriving the main PETS formulae, we present a model for ohmic losses in the structures, the effect of which was neglected in the previous chapter. We first look at the longitudinal electric wake field produced by a bunch of finite size, without any ohmic losses. This will be the convolution of the charge distribution $q_\mathrm{b}\lambda(z)$ with the longitudinal wake function $W_0^{\parallel}(z)$, which is equal to the inner part of Equation (2.20),

$$E_\mathrm{b}(z)|_\mathrm{ideal} = -q_\mathrm{b}\lambda(z) * W_0^{\parallel}(z). \tag{3.1}$$

A PETS is a *constant impedance* travelling wave structure, where the geometry parameters are constant along the structure (except for special coupling cells near the entrance and exit). For this type of structure the electric field will be attenuated along the way [13], and Equation (3.1) is therefore extended as

$$E_\mathrm{b}(z) = E_\mathrm{b}(z)|_\mathrm{ideal} \exp\left(-\alpha_\Omega z\right), \tag{3.2}$$

where the attenuation parameter α_Ω is given by [13]

$$\alpha_\Omega = \frac{\omega_\mathrm{r}}{2Qv_\mathrm{g}}. \tag{3.3}$$

Since the attenuation in PETS is usually in the range of a few percent [10], instead of looking at a dynamic change along the structure we instead use the average ohmic attenuation. The longitudinal electric field is then approximated as

$$\begin{aligned} E_\mathrm{b}(z) &\approx -\int_{z'}^{\infty} \lambda(\tilde{z}) W_0^{\parallel}(z-\tilde{z})\mathrm{d}\tilde{z} \frac{1}{L_\mathrm{S}} \int_0^{L_\mathrm{S}} \exp\left(-\alpha_\Omega \tilde{z}\right) \mathrm{d}\tilde{z} \\ &= E_\mathrm{b}(z)|_\mathrm{ideal} \frac{1-\exp\left(-\alpha_\Omega L_\mathrm{S}\right)}{\alpha_\Omega L_\mathrm{S}} \\ &= E_\mathrm{b}(z)|_\mathrm{ideal}\, \eta_\Omega \end{aligned} \tag{3.4}$$

where we have defined the *Ohmic loss parameter*

$$\eta_\Omega \equiv \frac{1-\exp\left(-\alpha_\Omega L_\mathrm{S}\right)}{\alpha_\Omega L_\mathrm{S}}. \tag{3.5}$$

Consider now the energy loss per bunch. Because of energy conservation this energy is not lost, but instead stored as a field in the structure. We can therefore write the stored energy $\mathcal{E}_\mathrm{b}$ from one bunch as the negative of the energy loss in Equation (2.20), remembering to include ohmic losses which give a reduction where energy is released as heat. Because of the double integration in Equation (2.20), the ohmic losses enter twice. We still use the average attenuation over the structure, and write

$$\begin{aligned} \mathcal{E}_\mathrm{b} &= -\Delta\mathscr{E} \left[\frac{1}{L_\mathrm{S}} \int_0^{L_\mathrm{S}} \exp\left(-\alpha_\Omega z\right) \mathrm{d}z\right]^2 \\ &= q_\mathrm{b}^2 \int_{-\infty}^{\infty} \lambda(\tilde{z}) \int_{\tilde{z}}^{\infty} \lambda(z) W_0^{\parallel}(\tilde{z}-z)\mathrm{d}z\mathrm{d}\tilde{z} \left[\frac{1}{L_\mathrm{S}} \int_0^{L_\mathrm{S}} \exp\left(-\alpha_\Omega z\right) \mathrm{d}z\right]^2 \\ &= 2q_\mathrm{b}^2 k_n' F^2 \left\{\lambda(z)\right\} \eta_\Omega^2. \end{aligned} \tag{3.6}$$

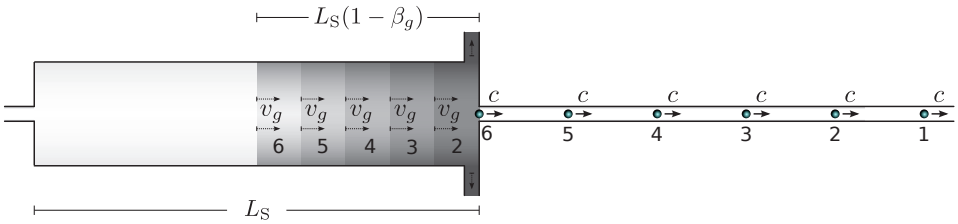

Figure 3.1: Build-up of a field inside a PETS, where the output field is the constructive total field from $N_R = 6$ bunches. $\beta_g = 0.5$ was assumed for the illustration.

3.1.2 Field build-up

A PETS is a travelling wave structure, so the wake field produced from a passing bunch will travel after the bunch and out of the structure. The group velocity v_g of the field is slower than the bunch, however, and in the current design it is approximately half the speed of light [10]. This means that the following bunch will eventually catch up with the field from the bunch in front of it. We will in the following derive a simplified model for the field build-up in PETS, that does not take into account structure bandwidth limitations.

Consider first a bunch that has passed through a PETS of length L_S and that has come to the exit of the structure, as shown by particle number 6 in Figure 3.1. At the same time the trailing field will have traveled a distance $\beta_g L_S$, where $\beta_g = v_g/c$. Thus, the field is contained in a fraction $L_S(1-\beta_g)$ inside the structure. For our model we assume that the field is constant in this part of structure and zero elsewhere.

Another, trailing bunch with index n will catch up with the field from the first bunch after the *catch-up* time $t_{c,n}$. We can also define a catch-up distance for this bunch as $d_{c,n} = c\,t_{c,n}$. Let the two bunches be separated by a distance nc/f_b, where n is an integer and $n = 1$ is the minimum distance. During the catch-up time, the field from the first bunch will have traveled a distance $d_{c,n} - \beta_g nc/f_b$, so we can write $t_{c,n} = (d_{c,n} - \beta_g nc/f_b)/v_b$. Substituting for the catch-up distance, we have

$$t_{c,n} = \frac{n}{f_b}\frac{\beta_g}{1-\beta_g}. \tag{3.7}$$

When bunches catch up with the fields from bunches in front of them, the total field will build up constructively as long as the bunches have the same phase. This is achieved by letting the bunch frequency be an integer multiple h of the mode resonant frequency, so that $2\pi f_b h = \omega_r$. For the current CLIC design, the first harmonic is used so that $2\pi f_b = \omega_r$. This will be assumed throughout the remaining derivation, but the principles will be the same for lower bunch frequencies (the main difference being a reduction of the produced field and power).

The field inside the structure from the first bunch has the largest extent once the bunch reaches the exit. The maximum build-up of the field will therefore result when the field from the first bunch reaches the output end, and is caught by a trailing bunch there. The field then travels a length $L_S(1-\beta_g)$. This defines the *ramp time* τ_R, which is the maximum possible catch-up time for constructive build-up,

$$\tau_R \equiv \frac{L_S}{v_g}(1-\beta_g). \tag{3.8}$$

The output field produced by the PETS will build up in a step-wise manner, starting with the first output field from the first bunch at time $t = 0$, before a steady-state is reached at $t = \tau_{\mathrm{R}}$. We can also calculate the number of bunches required for the ramp time N_{R}, by multiplying by the bunch frequency,

$$N_{\mathrm{R}} = \lfloor \tau_{\mathrm{R}} f_{\mathrm{b}} \rfloor \approx \frac{L_{\mathrm{S}} f_{\mathrm{b}}}{v_{\mathrm{g}}}(1 - \beta_{\mathrm{g}}) \tag{3.9}$$

The fractional part of N_{R} cannot be used for power production, since it represents extra time where the next bunch does not catch up with the field. Hence the floor function is used. However, for large N_{R} it will still be a good approximation to drop the floor function since the fractional part will be a negligible part of the whole number.

Figure 3.1 illustrates the field inside a PETS, which gets stronger towards the end of the structure. Only the fields that contribute to the total output field are shown. Since particle 6 catches up with the field from bunch 1, which is now only a thin disk at the output end, we have $N_{\mathrm{R}} = 6$.

3.1.3 Power generation

We now seek to derive an expression for the produced power in a PETS, and start from the stored energy that was expressed in Equation (2.25). However, we want to express the effective stored energy that is available for constructive build-up of power, and include two additional factors. Firstly, the field only fills a fraction $(1 - \beta_{\mathrm{g}})$ of the structure length as shown in Figure 3.1, and we therefore include a *field compression factor* [14] that expresses the energy in the relevant part, $1/(1 - \beta_{\mathrm{g}})$.

Also, the time in which a bunch is allowed to travel through the already existing field matters for how much it can contribute to the field itself. For short catch-up distances the bunch will give a significant contribution to the field, but when $t_{\mathrm{c},n} \lesssim \tau_{\mathrm{R}}$ the bunch catches up with the field at the exit of the structure and only gives a minor contribution. Therefore we also introduce a factor $(1 - t_{\mathrm{c},n}/\tau_{\mathrm{R}})$. For a single bunch n we write

$$\mathcal{E}_{\mathrm{b},n}(t_{\mathrm{c},n}) = -\frac{\Delta\mathscr{E}\eta_\Omega^2}{1 - \beta_{\mathrm{g}}}\left(1 - \frac{t_{\mathrm{c},n}}{\tau_{\mathrm{R}}}\right) = \frac{2q_{\mathrm{b}}^2 k'_n L_{\mathrm{S}}}{1 - \beta_{\mathrm{g}}} F^2 \left\{\lambda(z)\right\} \eta_\Omega^2 \left(1 - \frac{t_{\mathrm{c},n}}{\tau_{\mathrm{R}}}\right). \tag{3.10}$$

Equation (3.10) should be summed over all N_{R} bunches. For large N_{R} it is a valid approximation to instead use an integral,

$$\mathcal{E}_{\mathrm{T}}(t) \approx f_{\mathrm{b}} \int_0^t \mathcal{E}_{\mathrm{b},n}(\tilde{t})\mathrm{d}\tilde{t} = \frac{2q_{\mathrm{b}}^2 k'_n L_{\mathrm{S}} f_{\mathrm{b}}}{1 - \beta_{\mathrm{g}}} F^2 \left\{\lambda(z)\right\} \eta_\Omega^2 \int_0^t \left(1 - \frac{\tilde{t}}{\tau_{\mathrm{R}}}\right) \mathrm{d}\tilde{t}, \qquad t < \tau_{\mathrm{R}}. \tag{3.11}$$

This stored energy travels out of the PETS with every bunch passing through. We therefore find the produced power P by multiplying with the bunch frequency f_{b},

$$P(t) = \mathcal{E}_{\mathrm{T}}(t) f_{\mathrm{b}} = \frac{2q_{\mathrm{b}}^2 k'_n L_{\mathrm{S}} f_{\mathrm{b}}^2}{1 - \beta_{\mathrm{g}}} F^2 \left\{\lambda(z)\right\} \eta_\Omega^2 \left(t - \frac{t^2}{2\tau_{\mathrm{R}}}\right), \qquad 0 \le t < \tau_{\mathrm{R}}. \tag{3.12}$$

The power builds up during the ramp time, before a steady state is reached at $t = \tau_{\mathrm{R}}$. Substituting this time in Equation (3.12) and using Equation (3.8), we have

$$P = \frac{q_{\mathrm{b}}^2 k'_n L_{\mathrm{S}} f_{\mathrm{b}}^2 \tau_{\mathrm{R}}}{1 - \beta_{\mathrm{g}}} F^2 \left\{\lambda(z)\right\} \eta_\Omega^2 = \frac{q_{\mathrm{b}}^2 k'_n L_{\mathrm{S}}^2 f_{\mathrm{b}}^2}{v_{\mathrm{g}}} F^2 \left\{\lambda(z)\right\} \eta_\Omega^2, \qquad t \ge \tau_{\mathrm{R}}. \tag{3.13}$$

Finally, we can use an expression for the average beam current $I = f_\mathrm{b} q_\mathrm{b}$. Also using Equation (2.16), in terms of familiar structure parameters we can write

$$P = \frac{1}{4}(R'/Q)\frac{\omega_\mathrm{r}}{v_\mathrm{g}} L_\mathrm{S}^2 I^2 F^2 \left\{\lambda(z)\right\} \eta_\Omega^2, \qquad t \geq \tau_\mathrm{R}. \tag{3.14}$$

3.1.4 Beam deceleration

For the beam deceleration, it is convenient to use the voltage inside the PETS. This is because the maximum deceleration of certain particles in the bunch is equal to the peak voltage experienced inside the structure. First of all, we can express the longitudinal electric field *per unit length* from a single bunch as the stored energy from the bunch divided by the charge, and divided by the structure length. Since only a single integral is needed for the field as discussed in Section 3.1.1, we also divide by the form factor and the ohmic loss factor,

$$E'_{\mathrm{b},n}(t_{\mathrm{c},n}) = -\frac{\mathcal{E}_{\mathrm{b},n}}{q_\mathrm{b} F \left\{\lambda(z)\right\} \eta_\Omega L_\mathrm{S}} = -\frac{2 q_\mathrm{b} k'_n}{1-\beta_\mathrm{g}} F \left\{\lambda(z)\right\} \eta_\Omega \left(1 - \frac{t_{\mathrm{c},n}}{\tau_\mathrm{R}}\right). \tag{3.15}$$

Voltage is defined as a line integral over the electric field, and in our case the voltage from a single bunch is

$$\Delta V_{\mathrm{b},n}(t_{\mathrm{c},n}) = -\int_0^{L_\mathrm{S}} E'_{\mathrm{b},n}(t_{\mathrm{c},n}) \cdot \mathrm{d}\vec{l}. = -E'_{\mathrm{b},n}(t_{\mathrm{c},n}) L_\mathrm{S}. \tag{3.16}$$

In the same way as in the previous Section, we assume that many bunches are needed for the ramp time, and again approximate the contribution from all bunches as an integral,

$$\begin{aligned} \hat{V}(t) \approx f_\mathrm{b} \int_0^t \Delta V_{\mathrm{b},n}(\tilde{t})\, \mathrm{d}\tilde{t} &= \frac{2 q_\mathrm{b} k'_n L_\mathrm{S} f_\mathrm{b}}{1-\beta_\mathrm{g}} F \left\{\lambda(z)\right\} \eta_\Omega \int_0^t \left(1 - \frac{\tilde{t}}{\tau_\mathrm{R}}\right) \mathrm{d}\tilde{t} \\ &= \frac{2 q_\mathrm{b} k'_n L_\mathrm{S} f_\mathrm{b}}{1-\beta_\mathrm{g}} F \left\{\lambda(z)\right\} \eta_\Omega \left(t - \frac{t^2}{2\tau_\mathrm{R}}\right), \qquad 0 \leq t < \tau_\mathrm{R}. \end{aligned} \tag{3.17}$$

Steady-state is reached at $t = \tau_\mathrm{R}$, and by substitution we get

$$\hat{V} = \frac{q_\mathrm{b} k'_n L_\mathrm{S} f_\mathrm{b} \tau_\mathrm{R}}{1-\beta_\mathrm{g}} F \left\{\lambda(z)\right\} \eta_\Omega, \qquad t \geq \tau_\mathrm{R}. \tag{3.18}$$

Again using Equation (2.16) and the relation for the average beam current $I = f_\mathrm{b} q_\mathrm{b}$, the peak voltage and deceleration during the steady-state can be expressed

$$\hat{V} = \frac{1}{4}(R'/Q)\frac{\omega_\mathrm{r}}{v_\mathrm{g}} L_\mathrm{S}^2 I F \left\{\lambda(z)\right\} \eta_\Omega, \qquad t \geq \tau_\mathrm{R}. \tag{3.19}$$

Another useful relation is expressing the maximum deceleration from the produced power in the PETS, which can be measured. Comparing Equations (3.14) and (3.19), we get

$$\hat{V}(t) = \frac{P(t)}{I F \left\{\lambda(z)\right\} \eta_\Omega}, \qquad t \geq 0, \tag{3.20}$$

which is correct from a dimensionality argument involving power, voltage and current. Note that this equation is also valid during the ramp time. Alternatively, we can write an expression without the beam current,

$$\hat{V}(t) = \frac{L_\mathrm{S}}{2} \sqrt{\frac{(R'/Q)\,\omega_\mathrm{r}}{v_\mathrm{g}} P}, \qquad t \geq 0. \tag{3.21}$$

In the CLIC scheme, a constant beam current, bunch length and bunch phase are assumed, and Equations (3.19) then gives a constant value. However, as discussed in the next chapters, in the CTF3 these parameters are subject to change.

The maximum deceleration in Equations (3.19) and (3.21) is valid for infinitely thin bunches with a perfect bunch phase, and for particles inside a normal bunch that arrive with the correct phase. For longer bunches there will be a smeared out deceleration distribution, and for a changing phase there will also be a reduced deceleration. We can therefore express the *average deceleration* $\langle V \rangle$ as the maximum deceleration in Equation (3.19) multiplied with the form factor [11],

$$\langle V \rangle = \hat{V} F\left\{\lambda(z)\right\} = \frac{1}{4}(R'/Q)\frac{\omega_\mathrm{r}}{v_\mathrm{g}} L_\mathrm{S}^2 I F^2\left\{\lambda(z)\right\}\eta_\Omega, \qquad t \geq \tau_\mathrm{R} \tag{3.22}$$

or expressed from the power in Equations (3.20–3.21),

$$\langle V(t) \rangle = \frac{P(t)}{I\eta_\Omega} = \frac{L_\mathrm{S}}{2} F\left\{\lambda(z)\right\}\sqrt{\frac{(R'/Q)\,\omega_\mathrm{r}}{v_\mathrm{g}} P}, \qquad t \geq 0. \tag{3.23}$$

3.1.5 Energy loss including bunch train phase errors

For the CTF3, the normal operation of the injector leads to a change of the bunch phase over the pulse. It is therefore of interest to study how this affects the PETS power production and the deceleration of the beam. The phase contribution can be incorporated in the form factor, which was first defined in Equation (2.26), by letting the charge distribution $\lambda(z)$ involve several bunches. For every new bunch in steady-state we therefore consider the last N_R bunches, however the method still works during the ramp time by using fewer bunches. The charge distribution is still normalized so that $\int_{-\infty}^{\infty} \lambda(z)\,\mathrm{d}z = 1$.

Let us first write the total relevant charge distribution as a sum over the charge distribution of each individual bunch n, as $\lambda(z) = \sum_n \lambda_n(z)$ For having a phase reference, we define a bunch center for each bunch as

$$z_n \equiv \frac{\int_{-\infty}^{\infty} z\lambda_n(z)\,\mathrm{d}z}{\int_{-\infty}^{\infty} \lambda_n(z)\,\mathrm{d}z}, \tag{3.24}$$

and the bunch phase ϕ_n can then be defined

$$\phi_n \equiv \frac{\omega_\mathrm{r} z_n}{c}, \tag{3.25}$$

where the resonant frequency is $\omega_\mathrm{r} = 2\pi f_\mathrm{b}$ in our case.

We can now rewrite the form factor in Equation (2.26) for the steady state

$$\begin{aligned} F\left\{\lambda(z)\right\} &= \left| \int_{-\infty}^{\infty} \sum_{n=1}^{N_\mathrm{R}} \lambda_n(z)\, \exp\left[i\frac{\omega_\mathrm{r} z_n}{c}\right] \exp\left[i\frac{\omega_\mathrm{r}(z-z_n)}{c}\right] \mathrm{d}z \right| \\ &= \left| \int_{-\infty}^{\infty} \sum_{n=1}^{N_\mathrm{R}} \lambda_n(z)\, e^{i\phi_n} e^{i\theta_n(z-z_n)}\, \mathrm{d}z \right|, \end{aligned} \tag{3.26}$$

where in the last step we have defined an intra-bunch phase $\theta_n(z - z_n)$,

$$\theta_n(z - z_n) \equiv \frac{\omega_\mathrm{r}(z - z_n)}{c}. \tag{3.27}$$

Next we introduce a change of variables $z' = z - z_n$, and rewrite Equation (3.26) as

$$F\left\{\lambda(z')\right\} = \left| \int_{-\infty}^{\infty} \sum_{n=1}^{N_\mathrm{R}} \lambda_n(z' + z_n)\, e^{i\phi_n} e^{i\theta_n(z')}\, \mathrm{d}z' \right|. \tag{3.28}$$

Note that the variable z' is different for each bunch n, and the origin is located in the middle of the bunch.

Consider equal charge distributions for each bunch, $\lambda_\mathrm{b}(z') = \lambda_n(z' + z_n)$. The bunch charge distribution, which was originally centered around $z = z_n$, is effectively moved to $z = 0$ with the new function and variable. The intra-bunch phase $\theta_n(z')$ is also independent of the bunch number n, and is renamed $\theta_\mathrm{b}(z')$. This allows us to write

$$F\left\{\lambda(z')\right\} = \left| \int_{-\infty}^{\infty} \sum_{n=1}^{N_\mathrm{R}} \lambda_\mathrm{b}(z')\, e^{i\phi_n} e^{i\theta_\mathrm{b}(z')}\, \mathrm{d}z' \right|. \tag{3.29}$$

In this version, the charge distribution and the intra-bunch phase are independent of the bunch number, while the inter-bunch phase ϕ_n is independent of the longitudinal coordinate z'. It is therefore possible to separate the sum and the integral,

$$F\left\{\lambda(z')\right\} = \left| \left(\sum_{n=1}^{N_\mathrm{R}} e^{i\phi_n} \right) \int_{-\infty}^{\infty} \lambda_\mathrm{b}(z')\, e^{i\theta_\mathrm{b}(z')}\, \mathrm{d}z' \right|. \tag{3.30}$$

Next, consider equal bunch charge distributions that strictly decrease when $|z'|$ moves away from zero,

$$\frac{\mathrm{d}}{\mathrm{d}z'}\lambda(z') < 0, \qquad z' > 0, \tag{3.31a}$$

$$\frac{\mathrm{d}}{\mathrm{d}z'}\lambda(z') > 0, \qquad z' < 0. \tag{3.31b}$$

Also, if the bunch length is short compared to the bunch separation, the following relation holds,

$$\int_0^{c/4f_\mathrm{b}} \lambda_\mathrm{b}(z')\, \mathrm{d}z' \geq \int_{c/4f_\mathrm{b}}^{3c/4f_\mathrm{b}} \lambda_\mathrm{b}(z')\, \mathrm{d}z', \tag{3.32}$$

Under these conditions, the integral will be real and positive, and can be moved out of the modulus in Equation (3.30),

$$F\left\{\lambda(z')\right\} = \left| \sum_{n=1}^{N_\mathrm{R}} e^{i\phi_n} \right| \times \int_{-\infty}^{\infty} \lambda_\mathrm{b}(z')\, e^{i\theta_\mathrm{b}(z')}\, \mathrm{d}z'. \tag{3.33}$$

The sum and the integral can be normalized separately, by multiplying Equation (3.33) with $N_\mathrm{R}/N_\mathrm{R}$,

$$\begin{aligned} F\left\{\lambda(z')\right\} &= \frac{1}{N_\mathrm{R}} \left| \sum_{n=1}^{N_\mathrm{R}} e^{i\phi_n} \right| \times N_\mathrm{R} \int_{-\infty}^{\infty} \lambda_\mathrm{b}(z')\, e^{i\theta_\mathrm{b}(z')}\, \mathrm{d}z' \\ &\equiv \Phi(\{\phi_n\})\, F_\mathrm{b}\left\{\lambda_\mathrm{b}(z')\right\}. \end{aligned} \tag{3.34}$$

Here we have defined a functional that is a *single-bunch form factor*,

$$F_\mathrm{b}\left\{\lambda_\mathrm{b}(z')\right\} \equiv N_\mathrm{R}\int_\infty^\infty \lambda_\mathrm{b}(z')\, e^{i\theta_\mathrm{b}(z')}\,\mathrm{d}z', \tag{3.35}$$

as well as a function that we call the *multi-bunch form factor*,

$$\Phi(\{\phi_n\}) \equiv \frac{1}{N_\mathrm{R}}\left|\sum_{n=1}^{N_\mathrm{R}} e^{i\phi_n}\right|. \tag{3.36}$$

Because of normalization both of these form factors have the same normalization as the original in Equation (2.26),

$$0 \leq F_\mathrm{b}\left\{\lambda_\mathrm{b}(z')\right\} \leq 1, \tag{3.37a}$$

$$0 \leq \Phi(\{\phi_n\}) \leq 1. \tag{3.37b}$$

For Gaussian bunches we can further simplify the single-bunch form factor. Consider a normalized longitudinal Gaussian bunch distribution

$$\lambda_\mathrm{b}(z') = \frac{1}{N_\mathrm{R}\sqrt{2\pi}\sigma_z}\exp\left(-\frac{z'^2}{2\sigma_z^2}\right), \tag{3.38}$$

where σ_z is the bunch length standard deviation. By properties of the Fourier transform of a Gaussian, the single-bunch form factor in Equation (3.35) evaluates to

$$F_\mathrm{b}\left\{\lambda_\mathrm{b}(z')\right\} = F_\mathrm{b}(\sigma_z) = \exp\left(-\frac{\omega_\mathrm{b}^2\sigma_z^2}{2c^2}\right), \tag{3.39}$$

only dependent on the bunch length σ_z. This single-bunch form factor will in fact also follow a bell curve as a function of the bunch length. It will evaluate to one for infinitely short bunches, and longer bunches will give smaller single-bunch form factors and eventually less produced power in the PETS. It is therefore important to use short bunches in the drive beam.

Another important point is that the multi-bunch form factor in Equation (3.36) only depends on the relative phase change over a time equal to the ramp time. It will evaluate to one when the bunches have had the same phase over this time, regardless of their absolute phase values. Any change of phase will lead to a smaller multi-bunch form factor and less produced power.

3.2 Bunch combination

For achieving a high accelerating gradient for the main beam in CLIC, it is vital to reach a high power in the PETS, since each PETS will feed two accelerating structures [10]. By looking at Equation (3.14), we see that the power is affected by both beam and structure parameters. As already discussed in the previous Section, the bunch length should be short and the bunch phase should be constant in order to give a form factor close to one. For a given structure design, the only remaining parameter is then the beam current, which must be high since $P \propto I^2$.

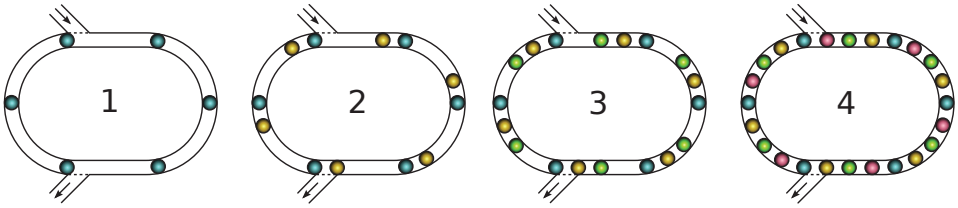

Figure 3.2: Bunch combination in a combiner ring, where bunches are interleaved by a factor of four (through four time steps). The dimensions are not to scale, and a small number of bunches is shown for illustrational purposes. Also, only half of the CLIC combiner ring will be filled, as opposed to this illustration.

The average beam current during the bunch train in CLIC is 101 A [10], which allows a very high power of 135 MW to be produced per PETS. However, the initial beam current from the injector is only 4.2 A, with a 0.5 GHz bunch structure. In order to produce the higher beam current, *bunch combination* is performed with the help of three rings after the injector. This can be seen in the upper part of Figure 1.1.

Firstly, the beam enters one *delay loop* that delays a 244 ns *sub-train* and interleaves it with the next sub-train that has a shorter path. Because of the chosen length of the delay loop, the total bunch train now has 244 ns sub-trains with twice the bunch frequency, and 244 ns holes in between. Next, the sub-trains are interleaved by a factor of three in the first combiner ring, which creates 244 ns sub-trains with 6 times the initial bunch frequency. Finally, there is a second combiner ring made for a factor of four bunch combination. In total, the bunch frequency and the average beam current are multiplied by a factor of 24 after all three rings. A simplified illustration of the combination process in the second combiner ring is shown in Figure 3.2.

Ideally, all bunches should arrive with the same phase to maximize PETS power production, as discussed in the previous Section. However, there may be a undesired change of phase over the pulse, as is the case in the CTF3 injector. In this case, the combination process will modify the incoming phase signal by shuffling (interleaving) the bunches, and this is illustrated in Figure 3.3 for a factor of four combination. The bunch-to-bunch phase change is much larger after combination, which can result in a smaller multi-bunch form factor. However, a measurement of the phase signal after combination may give a smeared-out signal, so the signal appears to have less variation than the uncombined version. This is because the sampling frequency of the measurement electronics is typically much lower than the bunch frequency, and therefore only an average over many bunches is obtained. In order to measure the phase of each bunch, the sampling frequency would need to be larger than twice the bunch frequency, in order to satisfy the Nyquist-Shannon sampling theorem.

If the transverse bunch trajectory through a ring is not properly closed, so that the trajectory is different for each revolution, there will be a transverse mismatch of the individual beamlets. This is illustrated in Figure 3.4 for a factor of four combination. The beamlets will then move differently through the rest of the lattice, instead of being united into a single beam. This can be detected on a measurement screen inserted into the beamline. However, this effect can sometimes still not be seen on a screen if the beamlets happen to be close together at that point. A transverse mismatch is normally not detectable by a BPM, which

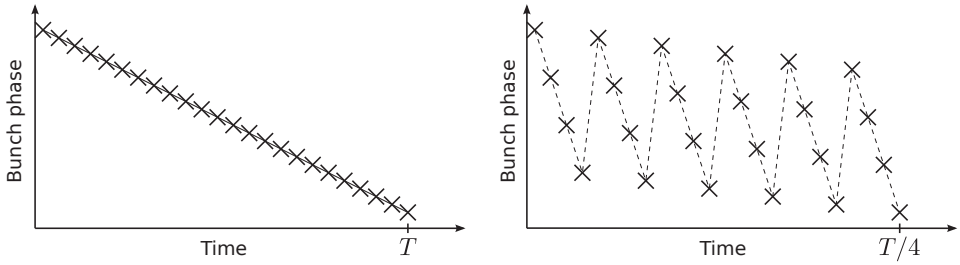

Figure 3.3: The effect of combination on the bunch phase. Left: An unwanted linear change of the phase over the pulse, for an uncombined beam. Right: Interleaving of bunch phases after a factor of four combination. Note that the time scale to the right is a factor of four shorter.

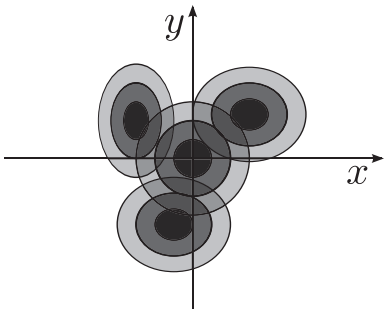

Figure 3.4: Transverse mismatch during a factor of four combination process, where the four beamlets are located at different positions in the (x,y) phase space.

only measures the average beam position. The error leads to a larger emittance of the whole beam, and a higher probability of beam loss downstream. Since the beam occupies a large part of the vacuum pipe at the end of the CLIC and CTF3 decelerators [10, 11], it is important to ensure a good transverse bunch combination.

3.3 Decelerators

The energy used for acceleration in CLIC will be extracted in decelerators running in parallel to the main beam, as shown in Figure 1.1. The decelerators are divided into 24 sectors, each of which receives a portion of the drive beam and extracts 90 % of its beam energy. The decelerator sectors are efficient power sources for the main beam due to the large energy extraction, and also because of the fully loaded drive beam accelerators upstream (the drive beam receives almost all the energy provided by its own accelerator). A selection of parameters relevant for the CLIC decelerators is shown in Table 3.1.

The decelerator sectors are around 1 km long, with the longest sector being 1053 m. They mainly consist of FODO lattices, which provide a good energy acceptance and tight focus-

Table 3.1: Beam, lattice and PETS structure parameters for the CLIC decelerators. The first four PETS parameters refer to the preferred synchronous mode used for power production.

Symbol	**Beam and lattice parameters**	**CLIC design**
–	Total length of lattice [m]	≤ 1053
$\mathscr{E}_0$	Initial energy [MeV]	2,370
$\mathscr{E}_{\min}$	Minimum final energy [MeV]	240
η_{extr}	Energy extraction, $(\mathscr{E}_0 - \mathscr{E}_{\min})/\mathscr{E}_0$ [%]	90
σ_z	Bunch length, RMS [mm]	1.0
$F\{\lambda_{\text{b}}(z')\}$	Single-bunch form factor	0.969
$\Phi(\{\phi_n\})$	Multi-bunch form factor	1.0
q_{b}	Bunch charge [nC]	8.4
f_{b}	Bunch frequency [GHz]	11.994
–	Bunch train length [ns]	244
I	Average beam current [A]	101
$\varepsilon_{\text{N}x,y}$	Initial normalized transverse emittances, RMS [μm]	150
–	Number of PETS [–]	1492
–	Vacuum chamber inner radius [mm]	11.5
–	Repetition rate [Hz]	50
Symbol	**PETS parameters**	**CLIC design**
$\omega_{\text{r}}/2\pi$	Synch. mode frequency [GHz]	11.994
R'/Q	Synch. mode impedance per meter [linac-Ω/m]	2,290
v_{g}	Synch. mode group velocity, $\beta_{\text{g}}c$ [c]	0.45
η_Ω	Synch. mode ohmic loss factor [–]	0.996
L_{S}	Structure length [m]	0.235
P	Power production per structure [MW]	134
$\hat{V}$	Max. deceleration per structure [MeV]	1.45
τ_{R}	Ramp time [ns]	0.9
N_{R}	Bunches required for field build-up [–]	10

ing. Between the quadrupoles there is space for PETS, each of which feeds two accelerating structures in the main beam via waveguides.

The PETS have a preferred synchronous mode at 12 GHz, which is the same as the bunch frequency and is the mode used for power production. Because of the high beam current of 101 A together with the short drive beam bunches, each structure can produce 135 MW of rf power. This allows an accelerating gradient for the main beam of 100 MV/m. Because of the rather short structure length of 23.5 cm, the ramp time is fairly short at 0.9 ns out of the 244 ns bunch train. In order to avoid higher-order modes (HOMs) that can be detrimental to the beam quality (e.g., dipole modes that can kick the beam), the structures will be equipped with HOM dampers.

A prototype decelerator has been constructed at CERN in order to test the novel technology. This is called the Test Beam Line, and will be described in detail in Chapter 4.

Chapter 4

The decelerator Test Beam Line

At full energy, CLIC will be a 48 km long machine that uses novel technologies. Before building such a machine it is essential that all technological aspects are understood and feasible. An important asset for the CLIC project has been the CLIC Test Facility 3 (CTF3), which was built at CERN as part of a large international collaboration. The CTF3 is essentially a drive beam complex, that also includes a small main beam used for two-beam acceleration.

The Test Beam Line (TBL) is one of the core experiments of the facility, where an electron beam is decelerated through a series of PETS. This beamline is the first prototype of a CLIC decelerator, and at nominal parameters it will be able to decelerate the beam by 55 %.

This chapter first presents some information about the experimental setup in the CTF3 in Section 4.1. Then some information on the TBL is provided in Section 4.2, including how the PETS measurements are performed.

4.1 The CLIC Test Facility 3

The CTF3 is the third generation of the CLIC Test Facility at CERN, that was built by the efforts of a large international collaboration [10, 15]. The machine reuses many components from older machines, including the Large Electron Positron (LEP) Pre-Injector, but some are also specifically built for the CTF3. The machine was first commissioned in 2001 [16], with an electron injector and two rings for bunch combination. Later, the facility was extended to include the CLIC Experimental area (CLEX) that houses the two experiments for two-beam acceleration technology, including the TBL [17, 18].

The main focus of the CTF3 is to study aspects related to the CLIC drive beam, and therefore a low-energy beam of relatively high intensity is used. The beam is produced by a thermionic gun. After that it is sent through a bunching system consisting of three sub-harmonic bunchers, one S-band pre-buncher, one travelling-wave buncher and two travelling-wave accelerating sections, which together create the necessary longitudinal profile of the bunch train [15]. The bunching system can be set up for either 1.5 GHz or 3 GHz beams. The former is used when the full bunch combination potential of the CTF3 is utilized, while the latter is used when a lower beam current is sufficient. In either case, the combined beam reaches a bunch frequency of 12 GHz (which is the same frequency as the preferred synchronous PETS mode used for power production). A drawing of the whole facility is shown in Figure 4.1.

The bunched beam is sent through a fully loaded linear accelerator with travelling-wave

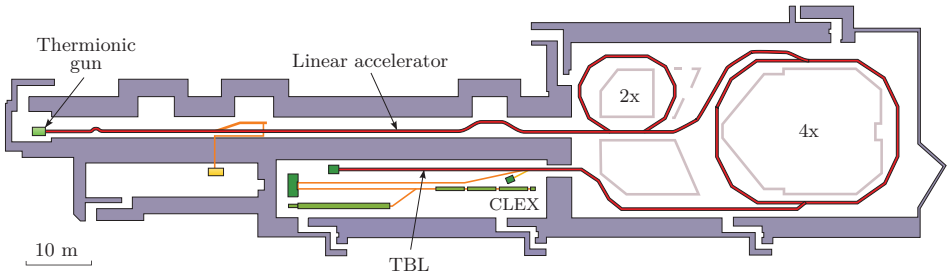

Figure 4.1: A sketch of the CTF3. The electron beam is produced by a thermionic gun, accelerated in a linac, combined in one delay loop and one combiner ring and finally sent to CLEX, which houses the TBL experiment.

structures (the beam receives all the energy of the accelerating field), and after that through a bunch-compressing chicane. At nominal operation this should bring the beam up to an energy of $\mathscr{E}_0 = 150$ MeV, with a bunch length of $\sigma_z = 1$ mm and an average beam current of around $I = 3.5$ A during the 1.2 μm long bunch train.

Next, the beam enters a room containing one delay loop and one combiner ring. The delay loop can combine bunches with a factor of two, and the combiner ring can combine bunches with a factor of four. When both rings are used, the beam therefore reaches a beam current of 28 A during a 244 ns long bunch train.

For the fully combined beam, there are usually some beam losses along the transfer line leading from the rings to the experimental area (CLEX). This is believed to originate from a non-perfect bunch combination, which was discussed in Section 3.2. The beam that enters the experimental area is therefore in the range of 20–24 A. Because of this, and because of the somewhat less stable beam of the full recombination scheme, for some experiments it is desirable to use a lower combination factor. The CTF3 can then be set up for a factor of four combination, using the combiner ring only and bypassing the delay loop, which provides a beam current of 14 A to CLEX. Alternatively, the combiner ring can also be bypassed so that an uncombined beam with a bunch frequency of either 1.5 or 3 GHz is sent to CLEX.

The experimental area consists of two main experiments, namely the Test Beam Line that will be elaborated on in the next section, and the Two-Beam Test Stand. For the latter, an additional *probe beam* is created and runs along the drive beam. The drive beam enters a single PETS, which extracts a portion of its energy. This is transferred via waveguides to two accelerating structures in the probe beam. The energy of the probe beam is measured before and after the two-beam setup, and an accelerating gradient of up to 150 MV/m has been measured [19], which is 50 % higher than the requirements for CLIC.

4.1.1 Particularities of the injector

The CTF3 has 10 klystrons installed that are used for the bunching system and the linac, which is two less than in the design [15]. The klystron output power is around 30 MW over a 6 μs pulse [20]. In order to reach a higher output power over a shorter time period, CTF3 uses *pulse compressors*. The pulse compressors store the rf power from the klystrons and release it shortly before the end of the pulse time, by flipping the phase 180 degrees. This produces about twice the amount of power towards the end of the pulse, however not at a

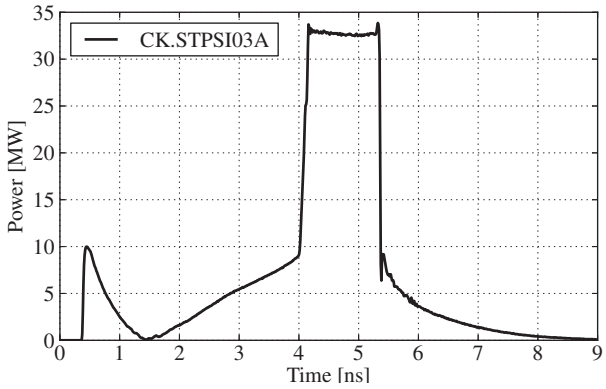

Figure 4.2: Measured output power from a klystron with pulse compressor, where the flat-top of around 1.5 μs is achieved by using a phase modulator.

constant amplitude by default.

In order to produce a flat-top during the end of the pulse, a *phase modulator* is also needed as input to each klystron. This produces a smooth phase transition from 0 to 180 degrees, and by that allows it allows a flat-top during the last part of the pulse. A measured output pulse from one klystron is shown in Figure 4.2. The pulse of the uncombined beam is 1.2 μs long, as is synchronized to fit inside the flat-top of the klystron pulse.

A drawback to using this scheme to increase the available power amplitude, is that the phase changes along the flat-top. An example phase measurement is shown in Figure 4.3. Here we see a *phase sag* with a change of around 10°. This phase sag can also be seen in the bunch phase of the uncombined beam, in phase measurements downstream. This effectively reduces the multi-bunch form factor given by Equation (3.36), and consequently the power production in the PETS.

Pulse compression is used in the CTF3, and introduces a phase variation over the bunch train. In the CLIC drive beam, klystrons will also be used for acceleration of the drive beam. The same scheme will not be used, however, mainly because of the loss in efficiency when using pulse compressors. Also, the tolerance for the klystron phase stability[1] is 0.05° [10] (any phase jitter leads to the wrong acceleration energy for the bunches and consequently to a luminosity loss). The significant phase change along the bunch train is therefore a particularity of the CTF3 machine.

4.2 TBL Experimental setup

The TBL is the first, and so far the only, prototype of a CLIC decelerator. The main goal of the experiment is to study the evolution of a drive beam undergoing strong deceleration in PETS, and the production of 12 GHz rf power. At nominal conditions, the most decelerated

[1]The change over the pulse can in principle be corrected using a phase program, and the main issue will then be the pulse-to-pulse stability.

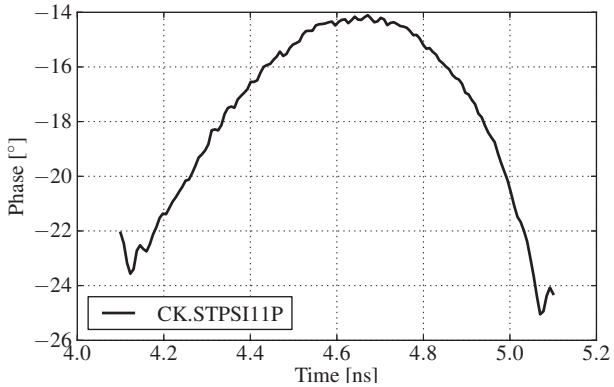

Figure 4.3: Phase measurement of a klystron output pulse, which is the result of using a phase modulator to achieve a flat pulse like that shown in Figure 4.2.

particles will lose around half of their initial energy of 150 MeV, which is converted into 12 GHz rf power. A photo of the current installation is shown in Figure 4.4.

Looking at Table 3.1 for the CLIC decelerators, we see that both the initial and the final energy of CLIC (2.4 GeV and 240 MeV, respectively) are higher than the starting energy of the TBL, for the same aperture. In some ways the TBL can therefore be considered more challenging than the CLIC declerators, since the beams will occupy a larger portion of the vacuum pipe due to adiabatic undamping. At nominal conditions, the beam at the end of the TBL will occupy 2/3 of the available aperture, counting three standard deviations of a transverse Gaussian distribution [11].

Just like the CLIC decelerators, the TBL also mainly consists of a FODO lattice, with PETS placed between the quadrupole magnets. An illustration of the current lattice is shown in Figure 4.5. At the very start of the beam line, a dipole magnet can send the beam into a spectrometer for measuring the beam energy, or send it to the other main experiment in CLEX, namely the Two-Beam Test Stand. In normal operation the beam travels through the FODO lattice with a 90° betatron phase advance per cell. However, since the beam is decelerated and develops a large energy spread, this phase advance is applied to the most decelerated particles, as proposed in [21]. The higher-energy particles are then contained in the envelope of the low-energy particles. In practice this involves a linear tapering of the quadrupole strengths to the beam energy along the line.

Each quadrupole is mounted on moving tables developed by CIEMAT Madrid [22], that can move the quadrupoles horizontally and vertically with a precision of 5 μm. This allows for a manual correction of the beam trajectory along the line, or the use of more advanced beam-based alignment schemes [23]. The TBL also includes three conventional corrector magnets for steering.

The main part of the beamline contains beam position monitors (BPMs) developed by IFIC Valencia and UPC Madrid [24, 25, 26]. They are inductive pick-up wall current monitors, that are a scaled and revised version of the BPMs in the CTF3 linac. The BPMs are also used for intensity diagnostics, and the main error contribution to the beam current measurements

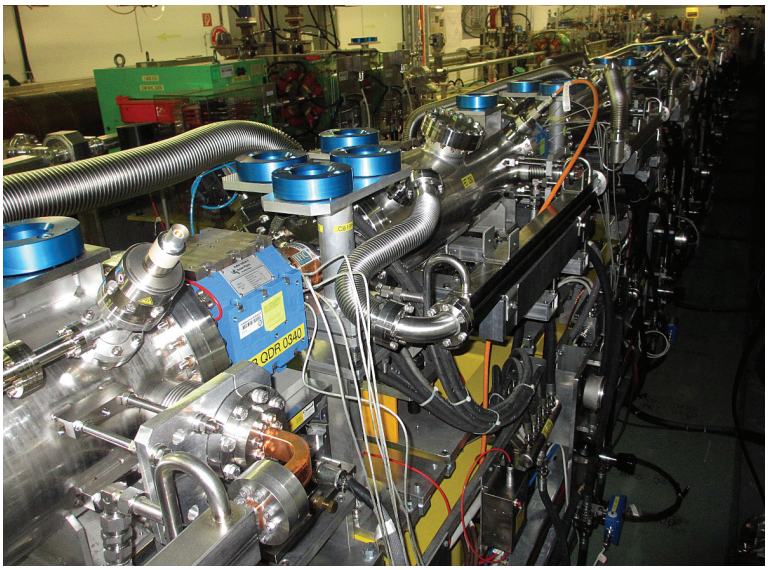

Figure 4.4: A photo of the Test Beam Line, from the FODO lattice with PETS structures.

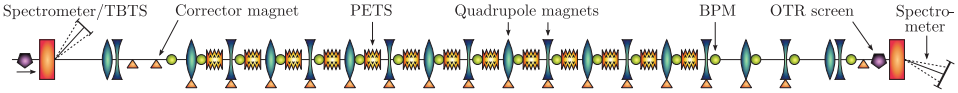

Figure 4.5: The current TBL lattice with 13 PETS installed (not to scale). The electron drive beam enters from the left. Quadrupole magnets are shown as lenses, dipole magnets as rectangles, corrector devices as triangles, BPMs as circles, screens as pentagons, and PETS as corrugated structures.

is the resolution of the ADCs, that is relatively worse at lower beam currents.

Throughout the CTF3 are also some button BPMs with resonant pick-up, and these are called BPRs. In addition to measuring beam position and beam current, these are also equipped with a WR-28 waveguide connected to the beam pipe, which picks up high-frequency content from the bunch train and can be used to measure the bunch length [27]. As a fourth measurement, the signals from the BPR electrodes are mixed with a 3 GHz reference signal with a phase shifter [28]. The mixed signal provides a measurement that is related to the bunch phase. Because of the multi-bunch form factor described in Section 3.1.5, phase measurements are important in order to understand the PETS power production.

The spectrometer at the end of the TBL is a specially designed segmented dump that contains 32 equally spaced tungsten segments [29, 30, 31]. This allows for time-resolved, single-shot spectrometry with a resolution of 1 %. The final energy measurement is compared to the incoming energy measured with the spectrometer at the start of the beam line. This is of a more simple type and is equipped with a single slit, which allows time-resolved spectrometry with a scan.

The transverse beam distribution is monitored with the aid of optical transition radiation (OTR) screens [31, 32]. These are imaged by charge-coupled device (CCD) cameras, and are inserted into the beamline when needed. One screen is located before the dipole magnet at the entry to the beamline, while another is located before the dipole magnet at the end of the beamline. These two screens are used for emittance measurements as described in Section 2.3.2, by changing the strength of the quadrupole doublet located before the screen that is used. In addition, one screen is placed between each dipole and spectrometer, primarily for beam steering into the spectrometer. Finally, the bunch length can be monitored by a streak camera imaging the OTR screen at the start of the beamline.

A collection of beam, lattice and PETS parameters are given in Table 4.1. Some of the nominal parameters have not yet been reached in the CTF3, therefore we specify both nominal and currently achieved numbers. The beam current is lower than nominal because of losses in the upstream transfer line, which can possibly be attributed to errors in the bunch combination process. This affects the PETS power production and deceleration as explained in Section 3.1. When the full factor of 8 combination is used in the CTF3, the horizontal emittance in the TBL is higher than nominal, possibly due to spurious dispersion and a horizontal mismatch during the bunch combination. As mentioned earlier, the incoming energy is lower than nominal. Table 4.1 should be compared to Table 3.1, which shows parameters for the future CLIC decelerators.

The TBL uses a dedicated graphical user interface for operation and PETS measurements [33]. During the work of this thesis, the program was extended with an operation mode for deceleration measurements, which can be seen in Figure 4.6. This program shows the measured and the estimated power production and deceleration in each PETS. Also, the total power and deceleration according to formulae from Section 3.1 is displayed. The totals can be compared for different estimated average form factors $F\{\lambda(z)\}$, until an agreement is found. This tool has proved useful during beam optimization in CTF3, where machine controls are varied to maximize the form factor, and consequently the achievable PETS power and deceleration in the TBL. The program also features an automatic matching of the beamline through an interface to the MAD-X code [34, 33], which calculates optimal optics based on the results of quadrupole scans.

Table 4.1: Beam, lattice and PETS structure parameters. Nominal parameters are given for both the TBL and one CLIC decelerator, in addition to currently achieved numbers for the TBL.

Symbol	**Beam and lattice parameters**	**Current TBL**	**Nominal TBL**
–	Total length of lattice [m]	40	40
$\mathscr{E}_0$	Initial energy [MeV]	120–125	150
$\mathscr{E}_{\min}$	Minimum final energy [MeV]	75–118	67
η_{extr}	Energy extraction, $(\mathscr{E}_0 - \mathscr{E}_{\min})/\mathscr{E}_0$ [%]	6–37	55
σ_z	Bunch length, rms [mm]	1.0–2.5	1.0
$F\{\lambda(z')\}$	Single-bunch form factor	0.75–0.98	0.969
$\Phi(\{\phi_n\})$	Multi-bunch form factor	0.85–0.98	1.0
q_{b}	Bunch charge [nC]	2.3	2.3
f_{b}	Bunch frequency [GHz]	1.499–11.994	11.994
–	Bunch train length [ns]	140–1120	140
I	Beam current [A]	3.5–22	28
$\varepsilon_{\text{N}_{x,y}}$	Norm. trans. emittances, rms [μm]	150–500	150
–	Number of PETS [–]	13	16
–	Vacuum chamber inner radius [mm]	11.5	11.5
–	Repetition rate [Hz]	0.83–1.67	0.83–5.0
Symbol	**PETS parameters**	**Current TBL**	**Nominal TBL**
$\omega_{\text{r}}/2\pi$	Synch. mode frequency* [GHz]	11.994	11.994
R'/Q	Impedance/meter* [linac-Ω/m]	2,222	2,222
v_{g}	Group velocity*, $\beta_{\text{g}}c$ [c]	0.46	0.46
η_Ω	Ohmic loss factor* [–]	0.985	0.985
L_{S}	Structure length [m]	0.8	0.8
P	Power production per structure [MW]	2–70	135
$\hat{V}$	Max. deceleration per structure [MeV]	0.6–3.3	5.2
τ_{R}	Ramp time [ns]	3.1	3.1
N_{R}	Bunches required for field build-up [–]	37	37

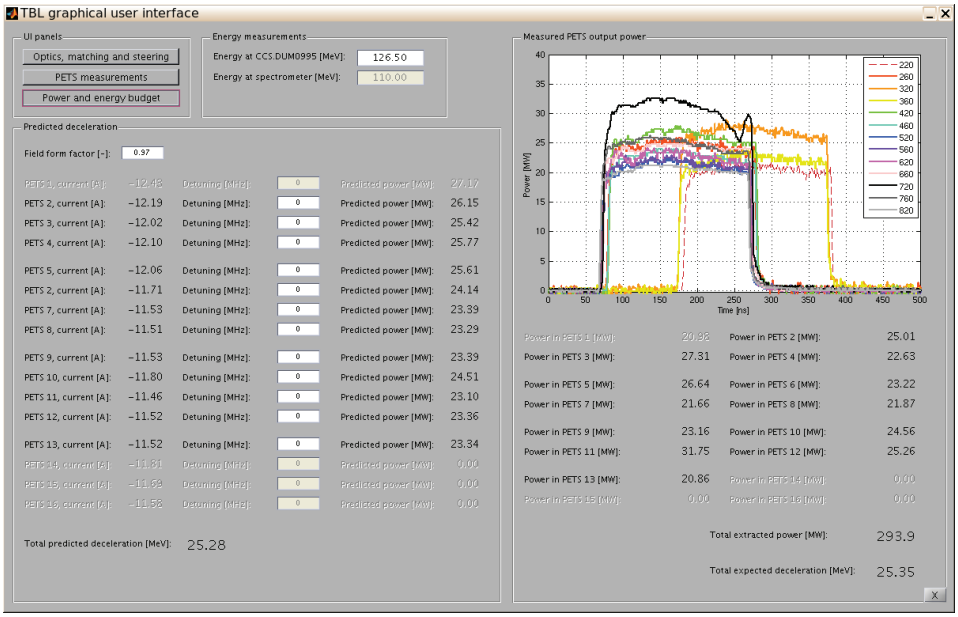

Figure 4.6: The TBL graphical user interface, with the operation mode for power and deceleration in PETS. The measured and estimated power and deceleration in each PETS is shown, together with a total for the whole beamline. The estimation on the left depends on the input form factor, which provides a method for an online estimation of the form factor.

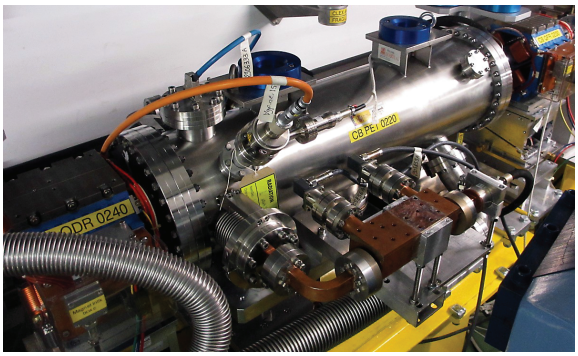

Figure 4.7: A PETS vacuum tank installed in the Test Beam Line. In front one can see a PETS arm, where the produced power is measured in dissipated in an rf load.

4.2.1 PETS and power measurements

The TBL was designed as a prototype decelerator with 16 PETS, and currently 13 are built and installed. Four of the structures were constructed by CIEMAT, Madrid [35, 36], and the remaining 9 were constructed at CERN. The design of the structures is fairly similar to the CLIC PETS, as can be seen by comparing Tables 3.1 and 4.1. This includes the power production mode frequency, R'/Q and group velocity.

One major difference, however, is the length of the PETS. Because the drive beam current in the CTF3 is about a factor of 4 lower than that in CLIC, the PETS length is about a factor 4 longer for compensation. The TBL PETS can therefore produce roughly the same amount of rf power, and needs a longer ramp time to reach steady-state.

The PETS are made of copper, and all except one are equipped with higher-order mode (HOM) dampers made of silicon carbide. These are installed to damp transverse modes, which can be detrimental to the beam quality. The full structures are placed inside vacuum tanks and are water-cooled to avoid thermal deformations. A photo of one of the tanks is shown in Figure 4.7.

The power produced in the PETS is coupled out in two output couplers on the sides, called PETS *arms*. Since the raw power is much too high to be measured with normal electronics, most of it is dissipated in water-cooled loads. Some of the forward power travels via a directional coupler to measurement electronics. One of the PETS arms including the directional coupler can be seen in the front in Figure 4.7.

An illustration of the measurement setup for one PETS is shown in Figure 4.8. The majority of the output power on both sides of the PETS is dissipated in rf loads. An rf choke at the PETS exit prevents the power from travelling into the vacuum pipe. Some of the produced power is coupled out in a directional coupler with an attenuation of approximately -50 dB. It then travels through a long cable from CLEX to the klystron gallery in the floor above for measurements, since this area has significantly less radiation. The attenuation in these cables is on the order of -20 dB, and there is also a fixed attenuator of -20 dB placed before the measurement electronics. The power produced in the PETS is therefore attenuated by around -90 dB in total, and is in an acceptable range of tens of mW when entering the

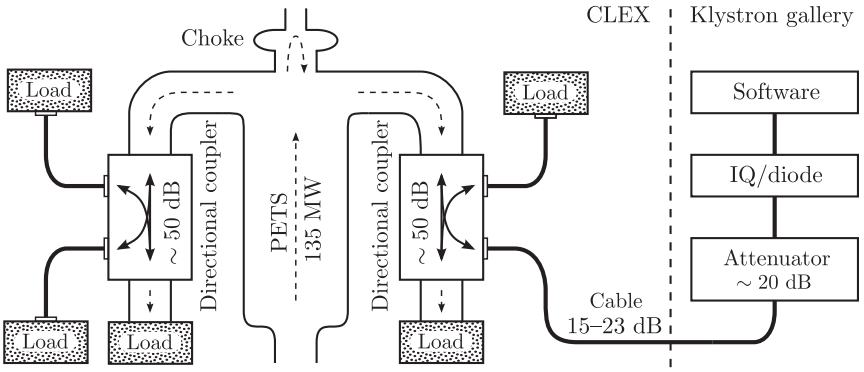

Figure 4.8: The PETS signal chain. The power produced in a PETS is coupled out in a directional coupler, attenuated by around 90 dB and measured.

electronics.

In some cases, some of the produced PETS power may be reflected by the load, and will also be coupled out through the directional coupler. The reflected power can be measured in the same way as the forward power. However, due to a limited amount of ADC channels, only the forward power is measured for the time being. For the same reason, only the power from one arm is measured for each PETS. The reflected power has previously been measured, and has been negligible under normal circumstances. The difference in power on each side of the PETS has previously also been measured, and a small asymmetry was found that depended on the horizontal beam position inside the structure [33].

An issue with the measurement setup in Figure 4.8 is that the calibration must be done piecewise – that is, for the attenuation the long cable is measured separately from the directional coupler, and so on. When the equipment is reconnected, there can be an attenuation difference of the order of 0.2 dB in each location, which leads to an uncertainty in the total absolute attenuation. We estimate a total attenuation error of up to 0.8 dB, which corresponds to 20 % in the measured power amplitude. In the data analysis this must be taken into consideration. However, the attenuation is the same for the whole signal, so one can correct for the error by fitting the shape of the power signals to other, more accurate, measurements.

The forward power amplitude from each PETS is currently measured with Schottky diodes, and digitized for use with the CTF3 control system. The diodes do not provide information about the rf phase, however, and therefore the first PETS is also measured with IQ (in-phase/quadrature) demodulators, which mixes the PETS signal with a 12 GHz reference signal. The produced rf phase signal is related to the bunch phase, and is important in order to understand the power production as described in Section 3.1.5.

4.2.2 A brief experimental history of the TBL

The TBL was constructed around 2008, with a single PETS installed from the start [17]. The beamline was commissioned with one PETS until the end of 2010 [37, 38]. Some PETS measurements were performed, including the study of the rf power output in the two PETS

arms as a function of the beam position inside the structure [33].

The following year, a total of 4 PETS was installed. This allowed the first measurements of a significant beam deceleration, and up to 55 MW of rf power was produced per structure. In 2012 the number of PETS was increased to nine, and up to 26 % beam deceleration was reported [39]. During this run, a beam-based steering campagin was also carried out, that provided a significant improvement of the beam trajectory in both planes.

In 2013, the total number of PETS was increased to 12. During this run, there were some problems with the bunch combination with a factor of 8 in the CTF3, mainly due to repairs of the power sources for the CTF3 injector. Therefore a factor of 4 bunch combination was used most of the time [40, 41, 42]. Still, this allowed a maximum beam deceleration of 27 %, together with a factor of 8 record during unstable conditions with 36 % deceleration.

Currently, 13 PETS are installed in the TBL. The factor of 8 bunch combination is again more reliable, which has allowed for a stable deceleration measurement of 37 %, described in Chapter 5. Around 70 MW of rf power is produced in each structure, which amounts to more than 900 MW in total for the whole beamline.

In addition to beamtime provided for the experiments, a major effort has been done the last years in the CTF3 to improve the beam quality, machine alignment, klystron stability, water cooling temperature stabilization and more [19, 41, 43]. Still, the beam reaching the TBL is not yet of nominal parameters. In particular, if a higher beam current could be transported to and through the TBL, a deceleration of around 45 % would be achievable with the current number of PETS.

Chapter 5

Experimental deceleration studies and simulations

This chapter presents experimental results from the Test Beam Line, on a beam undergoing significant deceleration. Many results have already been published, and can be found in Appendix A. In particular we point to the article in Appendix A.1 [42], and some key results of this article will also be summarized at the end of this chapter. Most of the previous work has used data with a factor of 4 bunch combination in the CTF3, because of more stable conditions than for the fully combined beam. In this chapter, however, we present some newer deceleration measurements with a beam combined with a factor of 8. The analyzed data set contains 88 consecutive pulses (bunch trains), where the beam entering the TBL had an initial energy of 119 MeV.

5.1 Form factor estimations

The charge distribution form factor plays an important role in the PETS power production and in the beam deceleration, as shown by Equations (3.12–3.14) and (3.17–3.22). In order to reach consistency between the measurements in BPMs, PETS and in the spectrometers, it is therefore important to estimate the form factor along the bunch train. The form factor cannot be measured directly, but can be estimated from bunch length and bunch phase measurements.

A measurement of the bunch lengths using the streak camera in the TBL is performed by instrumentation experts, and needs to be planned in advance. Unfortunately these measurements do not always coincide with the good runs of the TBL experiment. Therefore the analyzed dataset does not have a streak camera measurement, as is the case for the dataset presented in the article in Appendix A.1. However, as will be seen later, the phase variation along the bunch train can explain most of the contribution to the form factor.

A measurement of the bunch phase of an uncombined beam is shown in Figure 5.1, and has a similar shape as that shown in Figure 4.3. The measurement was taken during the same run as the analyzed dataset, at a location in the CTF3 machine before bunch combination took place. The measurement was performed using a BPR, and Figure 5.1 shows the signal that was used in the analysis, where large phase jumps close to the pulse edges were omitted.

Initially the BPR signal had some noise, so a finite impulse response smoothening filter

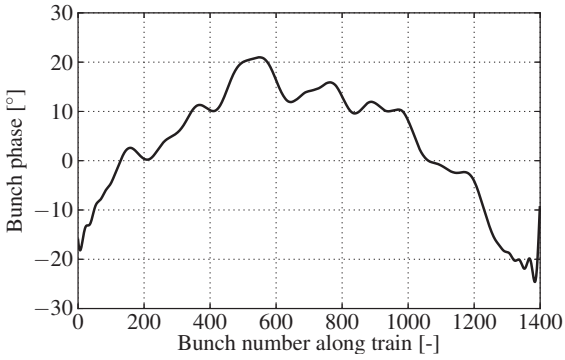

Figure 5.1: Bunch phase of the uncombined beam, measured before the delay loop in CTF3. The signal was interpolated to the corresponding number of bunches in the same time interval.

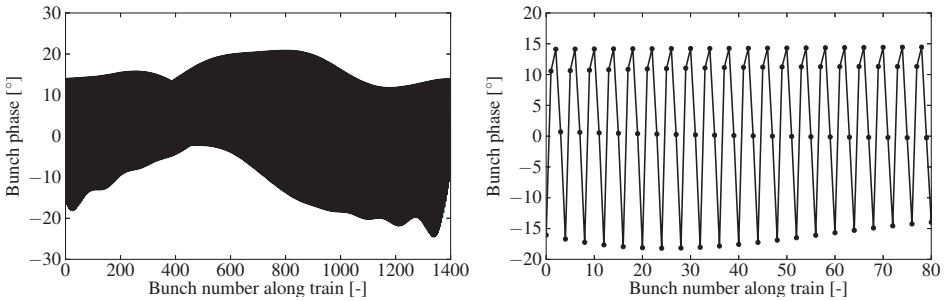

Figure 5.2: Calculated bunch phase of a factor of 8 combined beam, based on the measurement in Figure 5.1. The left plot shows the whole signal with exactly 1400 bunches, while the right plot shows the first 81 bunches.

with 5 coefficients was applied. The signal was then interpolated to the number of bunches corresponding to the time duration. Note that the the analysis in Appendix A.1 uses the rf phase measured in a PETS instead of a BPR signal. In that case the machine was changed to send an uncombined beam to the TBL.

As explained in Section 3.2, the phase of the uncombined beam should be used in the analysis, instead of the measured phase of the combined beam. This is because the high frequency content of the phase signal of the combined beam will be lost due to the Nyquist-Shannon sampling theorem. The phase of the uncombined beam can instead be interleaved to simulate the bunch combination process. This combined phase is shown in Figure 5.2, and features large phase jumps due to the combination process. Even though the number of bunches are the same as in Figure 5.1, the bunches are here concentrated in 1/8 of the time.

A multi-bunch form factor $\Phi(\{\phi_n\})$ can be constructed by using Equation (3.36). Since each sample of the phase signal corresponds to one bunch due to the signal interpolation, $N_{\mathrm{R}} = 37$ phase samples are used for each sample of the constructed multi-bunch form factor.

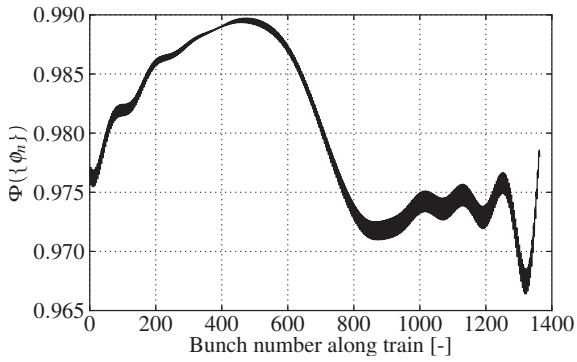

Figure 5.3: Calculated multi-bunch form factor $\Phi(\{\phi_n\})$ along the pulse, based on the phase signal in Figure 5.2 with Equation (3.36).

The result is shown in Figure 5.3, which like Figure 5.2 features some smaller sample-to-sample jumps. For an ideal machine $\Phi(\{\phi_n\})$ equals 1 everywhere, but in our measurements the PETS field is reduced by up to 3.3 % due to the phase variation.

5.2 Correlation between beam current and PETS power

The power produced in the PETS can be predicted based on the beam current measured in the BPMs, by using the formulae in Section 3.1.3. Since the transient of the pulse is very short and difficult to measure in practice, we concentrate on the steady-state part of the bunch train and use Equation (3.14). We continue to use the dataset with 88 pulses combined with a factor of 8.

The measured beam current in all 13 BPMs placed immediately before the 13 PETS is shown to the left in Figure 5.4. The first BPM in the line is plotted in black, and the curves are gradually more red and orange for each BPM down the beamline. The curves show averages over all 88 pulses. The average beam current in the first of these BPMs was 22.9 A, and the average at the location of the 13^{th} BPM was 19.2 A, implying an 84 % transmission. The beam loss can most likely be attributed to a transverse mismatch during the bunch combination, as explained in Section 3.2. The signals feature a small, non-zero amplitude starting around -50 ns. This is due to satellite bunches that are outside the main bunch train.

The right part of Figure 5.4 shows the corresponding rf pulses measured in the PETS, again as averages over the data set. Here, we also see a gradual decrease of power along the beamline, which can mostly be attributed to beam loss. The variation in power is more significant than the variation in current, since $P \propto I^2$. For the power there is also a larger uncertainty in the calibration, as explained in Section 4.2.1. This leads to a less accurate measurement of the absolute power amplitude in each PETS.

There is a variation in the shape of both the current and power signals, in addition to beam loss. The prediction of the produced rf power was therefore performed with averages over all the BPM pulses and all the PETS pulses, and the results are shown in Figure 5.5. The

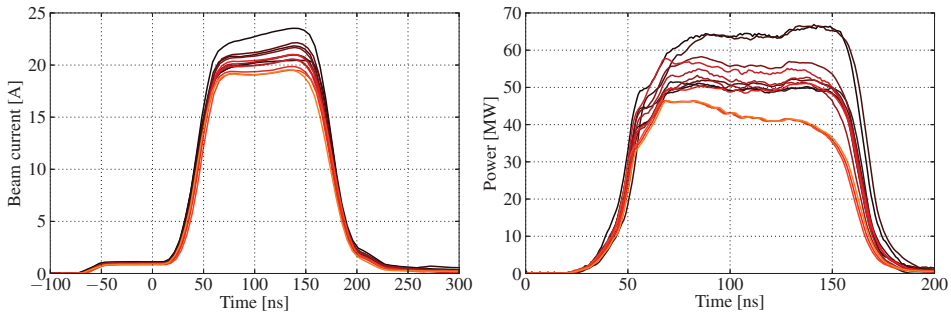

Figure 5.4: Left: Beam current measured in BPMs close to the 13 PETS. The first BPM is shown in black and the last is shown in bright orange. As can be seen, there were some losses along the beamline. Right: Corresponding power measurements for the 13 PETS. All curves display averages over the 88 pulses in the data set.

average PETS pulses are shown with blue dots, and the predicted power based on the BPM measurements together with Equation (3.14) is shown as a red stapled line. In the prediction of the power, the single-bunch form factor was used as an empirically derived scaling factor, with $F_{\mathrm{b}}(\lambda(z')) = 0.82$. Note that because of the uncertainty of the PETS calibration, this number should be seen as a guideline rather than an accurate estimation. As can be seen from Figure 5.5, the two curves discussed this far are somewhat different, and more careful analysis is therefore needed.

The electronics used for the BPM signals have less bandwidth than the PETS signals, and therefore the rising times and falling times are different for the two. The power measurement in blue was treated with a low-pass finite impulse response filter, to match the bandwidth of the BPM electronics. The resulting signal is shown in green in Figure 5.5, and the pulse edges match the BPM pulse more closely.

There is still a discrepancy during the steady-state of the pulse, and we therefore apply the multi-bunch form factor $\Phi(\{\phi_n\})$ from Figure 5.3 to the power prediction. The result is shown as a black line with dots in Figure 5.5. The treated beam current signal is closer to the filtered power in green, as expected. The remaining deviation can be due to a variation of the bunch length, and measurement noise (strongest in the rf signals).

5.3 Deceleration results

The beam in the analyzed data set had an initial energy of 119 MeV. This energy is an estimation based on upstream spectrometer measurements performed earlier, as well as the field strength of upstream dipole magnets. The energy spread at the start of the TBL was unfortunately not recorded for this run, and is instead estimated in the proceeding analysis.

The full energy spectrum of the decelerated beam (at the end of the beamline) is shown in Figure 5.6. This plot is again an average over the dataset. The contour lines indicate 10 % increments of the signal, compared to its maximum value. As seen from the figure, the spectrum features a very large energy spread, estimated to 21 % FWHM. This is partly due

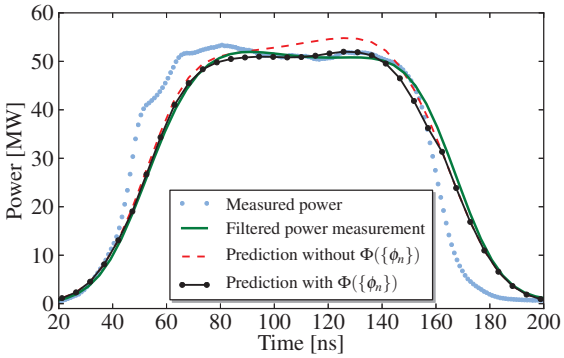

Figure 5.5: Predicted power in PETS based on the measured beam current in BPMs. The measured power is shown in blue, and the power treated with a low-pass filter is shown in green. The predicted power without application of the multi-bunch form factor is shown in red, and the prediction including $\Phi(\{\phi_n\})$ is in black. All curves are averages between the 13 corresponding signals, averaged over the dataset.

to the deceleration process, but likely also because of a large incoming energy spread into the beamline.

The average measured energy is indicated by crosses in Figure 5.6, and is calculated to around 85 MeV during most of the pulse. For the maximum deceleration we define a threshold of 10 % of the maximum signal. At 125 ns we find the lowest energy, which is 74.9 MeV. This corresponds to a maximum deceleration of 37 %.

5.3.1 Comparison between measurements and simulations

The measured final energy spectrum including the energy spread can be compared to simulations. We use the PLACET [44] tracking code, which simulates both single-bunch and multi-bunch wakefields and therefore provides a good model of the beam energy spread.

Figure 5.7 again shows the energy profile from Figure 5.6, as black dots. The dots show averages over the time period of the pulse that is fairly constant, and the error bars show the statistical uncertainty during this time period. A simulation performed with PLACET is shown as a histogram in Figure 5.7. Since the incoming energy spread was unknown for the dataset, it had to be estimated. The measured energy profile from 86 to 100 MeV was higher than all simulations performed with reasonable numbers for the energy spread. A reasonable agreement was found for an incoming energy spread of $\frac{\sigma_E}{E} = 6$ %, which is shown in the figure. However, this is higher than common measurements at the entrance to the beamline, which normally lie in the range from 1 % to 3 %.

Another unknown parameter for the dataset was the bunch length, which affects the deceleration through the single-bunch form factor in accordance with Equations (3.35) and (3.39). In the simulations, a value of $F_\mathrm{b}\{\lambda(z')\} = 0.82$ gave the closest result, corresponding to bunch lengths of $\sigma_z = 2.5$ mm.

One possible reason for the discrepancy in Figure 5.7 is non-Gaussianity in the incoming energy profile. This was seen in the measurements reported in the article in Appendix A.1,

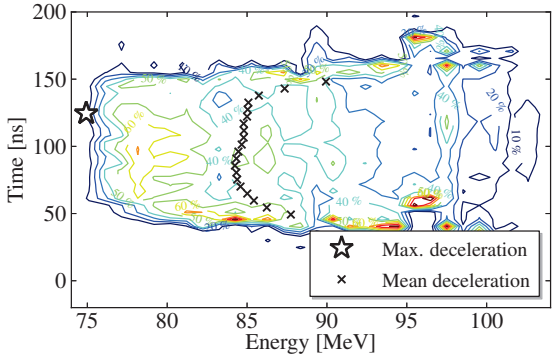

Figure 5.6: Spectrometer measurement from the segmented dump spectrometer at the end of the TBL, averaged over the data set. The maximum deceleration is indicated by a star, and the average deceleration over the pulse is shown with crosses.

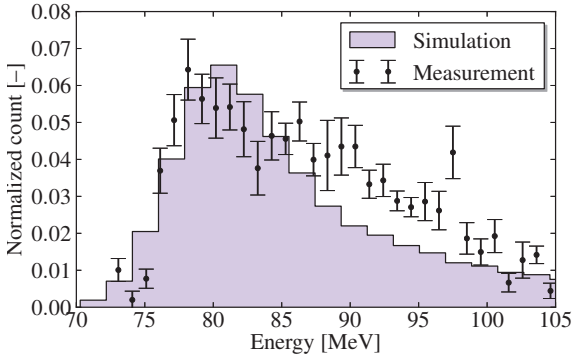

Figure 5.7: A comparison of the measured energy profile from Figure 5.6 (black dots) with a simulation performed with the PLACET tracking code (histogram). A bunch length of $\sigma_z = 2.5$ mm and an incoming energy spread of 6 % was assumed in the simulation, while the remaining simulation parameters correspond to those measured in the TBL.

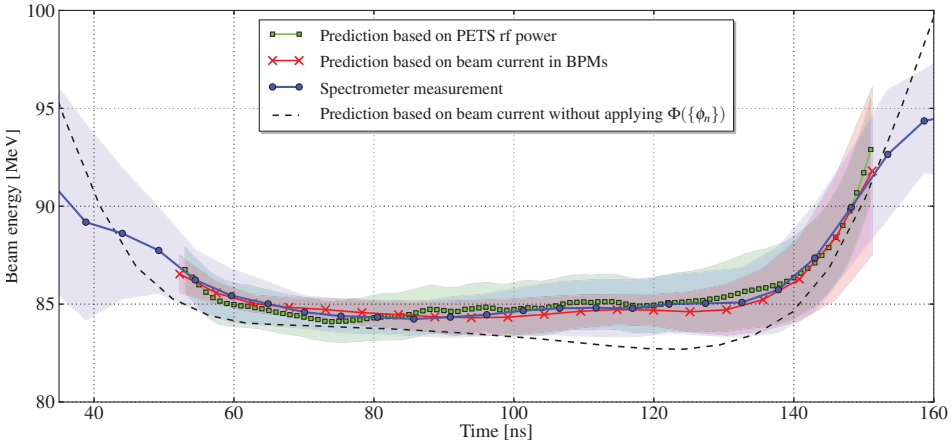

Figure 5.8: Average measured energy (blue circles), together with predicted deceleration based on the beam current (red crosses) and the PETS rf power (green squares). The calculated multi-bunch form factor shown in Figure 5.3 was applied along the pulse, while the single-bunch form factor and the rf calibration uncertainty were chosen as empirically derived scaling factors. A prediction based on the beam current, but without the inclusion of the multi-bunch form factor, is shown with a black stapled line.

where the non-perfect energy profile propagated down to the final spectrometer measurement.

5.3.2 Experimental predictions

We now correlate the measured energy with predictions based on measurements in BPMs and PETS. For this we use average energy measurement, indicated by crosses in Figure 5.6, as a reference. This is shown with blue squares in Figure 5.8. The energy outside the pulse edges was measured to around 95 MeV, as seen in the figure. This is an artifact of the measurement, and will not be considered in the analysis.

Firstly, we correlate the measurement of the beam current to the energy measurement. This is because the main contribution to the deviation between the two should be the form factor, in addition to measurement noise and small calibration errors. The rf power measurements from the PETS has a large calibration error in the power amplitude, as explained in Section 4.2.1. It therefore has a larger uncertainty, and we need an additional parameter in the analysis.

The predicted deceleration from the beam current during steady-state can be found with Equation (3.22) and the BPM signals. The predicted deceleration in each PETS was calculated from the BPM immediately in front of it, and the signals were added together to find the total deceleration. In this analysis, the calculated multi-bunch form factor shown in Figure 5.3 was decimated to the BPM sampling frequency, squared and multiplied with each BPM signal. Since bunch length measurements were not available together with this dataset, the single-bunch form factor was estimated as an empirically derived scaling factor. A value of $F_\mathrm{b}\{\lambda(z')\} = 0.85$ gave a result close to the spectrometer measurement, corresponding

to Gaussian bunch lengths of $\sigma_z = 2.3$ mm. This prediction is shown with red crosses in Figure 5.8.

For reference we have also plotted the prediction based on the beam current without inclusion of the multi-bunch form factor. This is shown as a black stapled line, and we see the importance of calculating the multi-bunch form factor for the CTF3 machine.

Next, we predict the beam deceleration from the power measured in all PETS, by using Equation (3.23). For consistency, we use the same values for $F_\mathrm{b}\{\lambda(z')\}$ and $\Phi(\{\phi_n\})$ as calculated for the BPM signals. Because of the uncertainty of the power amplitudes because of the calibration, a global scaling parameter of the power amplitudes was applied. A reduction of the raw rf signals by 5 % gave the best result, which is shown with green squares in Figure 5.8.

Both predictions of the beam deceleration are quite consistent with the energy measurement, and the deviations can possibly be explained by a change in the bunch lengths over the pulse, and by measurement noise. The estimated single-bunch form factor is slightly different here than for the previous Section. One reason for this can be a slightly wrong calibration of the BPM amplitudes. Also, the PLACET simulation in Section 5.3.1 does not include beam losses, and consequently a reduced deceleration is compensated by a lower form factor. Finally, the procedure is somewhat different, since in this Section we focus on the average deceleration, while in Section 5.3.1 we look at the entire energy spectrum.

5.4 Other measurements

The article in Appendix A.1 mostly presents experimental data from a beam combined with a factor of four, and some of the analysis is similar to that presented so far in this chapter. However, the article also includes some other measurements that will be summarized here.

In CTF3 it is possible to use a lower combination scheme than a factor of four in the combiner ring. This can be done by removing a part of the bunch train, so that only 2 or 3 out of 4 bunches get combined. Also, the combiner ring can be bypassed, so that a long bunch train of either 1.5 or 3 GHz is sent directly to the TBL. This in effect corresponds to a 'factor of 1' combination. For the factors 1, 2 and 3, not all buckets of the preferred synchronous mode in the PETS will be filled, which leads to a reduction of the produced power.

By using different combination schemes, one can study how the amount of beam current affects the deceleration. In accordance with Equation 3.22, we expect a linear relation between beam current and deceleration. The TBL was set up for combination factors of 1, 2, 3 and 4 using the combiner ring, and for each setting the final energy was measured. 60 pulses were used at each point, and the resulting distributions are shown in Figure 5.9. The linear correlation coefficient amounts to -0.986, indicating a strong negative correlation.

A linear fit to the data points is also shown in Figure 5.9. This can be extrapolated to zero beam current, to obtain an estimation of the beam energy without deceleration. However, because of the extrapolation the intercept has a large error bar. For our measurements, the initial energy was measured to $E_0 = 123.5$ MeV, which is well within the 95 % confidence interval of the fit.

Drive beams experience heavy deceleration and develop a large energy spread. For CLIC it is important to know that such a beam can be transported through the 1 km decelerators. One key aspect is the evolution of the transverse emittance during deceleration. Ideally, the only increase in transverse emittance is due to adiabatic undamping. The TBL is a

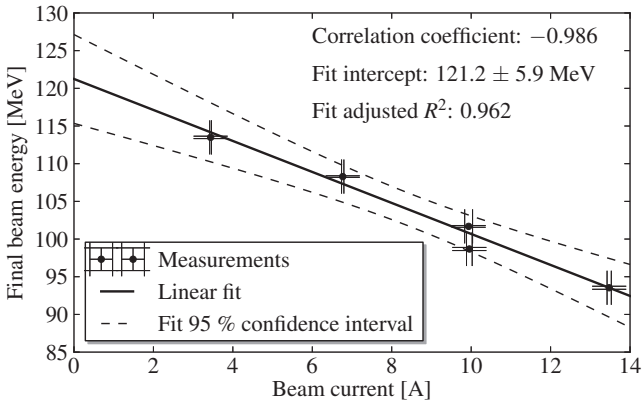

Figure 5.9: Measured final energy in the TBL as a function of the beam current. There is a strong negative correlation between the two, as expected.

decelerator prototype, and an experiment was carried out to study the emittance evolution from the beginning of the beamline to the end.

As described in Section 2.3.2, in TBL the transverse emittance and the Twiss parameters are measured using quadrupole scans. These are performed both at the beginning and at the end of the beamline, and are used to estimate the mentioned parameters. An example of a quadrupole scan at the end of the TBL is shown in Figure 5.10, together with a fit to the data. The data points are averages between four consecutive scans, and the measurement was taken for the horizontal emittance.

For comparing the data points in Figure 5.10 to measurements at the beginning of the TBL, three quadrupole scans were first carried out there. The measurements were averaged to find estimates for the Twiss parameters and the emittance. Then, these parameters were used as input to the PLACET tracking code, and particles were tracked through the beamline. A quadrupole scan was simulated in PLACET, by varying the strength of a quadrupole and recording the rms of the horizontal beam distribution at the location of the downstream screen. The simulated quad scan at the end of the line is shown with green squares in Figure 5.10.

Since the three measurements at the beginning of the TBL were slightly different, and because of the error bars of the measurements themselves, the incoming parameters had some uncertainty. Therefore, a scan of simulations were performed with PLACET, that took this spread into account. At the location of the quadrupole scan at the end of the line, this also resulted in a spread of simulated beam sizes. The spread is shown in Figure 5.10 by a light green band. When comparing measurements and simulations of the emittance evolution, there is an excellent agreement, meaning that the change in geometrical emittance can be attributed to adiabatic undamping alone.

For drive beams such as that in the TBL, quadrupole scans can be strongly affected by chromaticity [9], where particles of different energies experience different focusing. With nominal conditions in the TBL this contributes a 20 % error to the measured emittance [31]. However, for this measurement with less deceleration and a smaller energy spread, the error was estimated to 1.7 %.

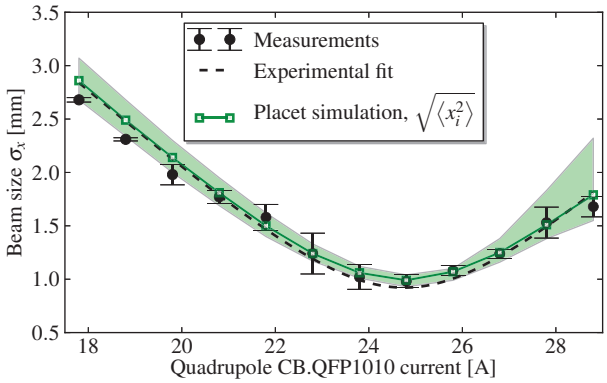

Figure 5.10: Quadrupole scan performed at the end of the TBL (black dots) for the horizontal emittance, with an experimental fit to the data (black stapled line). The quadrupole scan was also simulated with PLACET, using incoming parameters measured at the beginning of the beamline. The simulation is shown with green squares, and its uncertainty is shown with a light green band.

Chapter 6

CLIC Drive beam space charge

This chapter discusses longitudinal space charge in the CLIC decelerators. In particular, we describe a simulation program that was developed from scratch during the thesis work. This code was written in Octave [45] within the Particle-in-Cell framework, and obtained simulation results of space charge effects in the drive beam are discussed. Some results are also given for the Test Beam Line for comparison.

Firstly, we discuss the motivation for studying longitudinal space charge in the drive beam in Section 6.1. Next, the Particle-in-Cell framework is presented in Section 6.2, within the context that was used for the developed program. Benchmarking of the code against some analytical models is discussed in Section 6.3 and simulation results of the CLIC decelerators are given in Section 6.4. Finally, in Section 6.4.2 we look at a hypothetical decelerator regime with even stronger deceleration, and the space charge effects there.

6.1 Motivation

As discussed in Section 2.1, the space charge effect is proportional to $1/\gamma^2$, where γ is the relativistic Lorentz factor. Space charge is therefore normally a concern at low energies, where the particle velocities are non-relativistic. The CLIC drive beam, however, enters the decelerators with an initial energy of $\mathscr{E}_0 = 2.4$ GeV, and has a final energy of 240 MeV after the energy extraction. This gives Lorentz factors of $\gamma \in [470, 4700]$, well into the relativistic domain, and space charge effects would normally not be considered.

However, in the CLIC main beams there is a strict tolerance on the acceptable luminosity loss, since a high collision frequency is needed in order to produce the necessary statistics for the detectors. An energy spread of $\frac{\Delta\mathscr{E}}{\mathscr{E}} < 7 \times 10^{-4}$ in the main beam is required to get an acceptable luminosity loss of less than 1 % [46]. One factor that affects the beam energy of the main beam is the drive beam bunch length, which contributes to the single-bunch form factor in accordance with Equation (3.39) for Gaussian bunches. This leads to a tolerance for a *coherent* change of the drive beam bunch length of 1.1 % [46]. For an incoherent variation over the bunch train the tolerance is more relaxed at 3.3 %, since the error is more randomly distributed. There has been some concern that, during the significant deceleration over the 1 km decelerators, longitudinal space charge may violate the coherent bunch length tolerance. A small increase in the transverse bunch size would not affect the power production in PETS, and is not of concern.

Before studying simulations, we can look at where the space charge effects are the strongest.

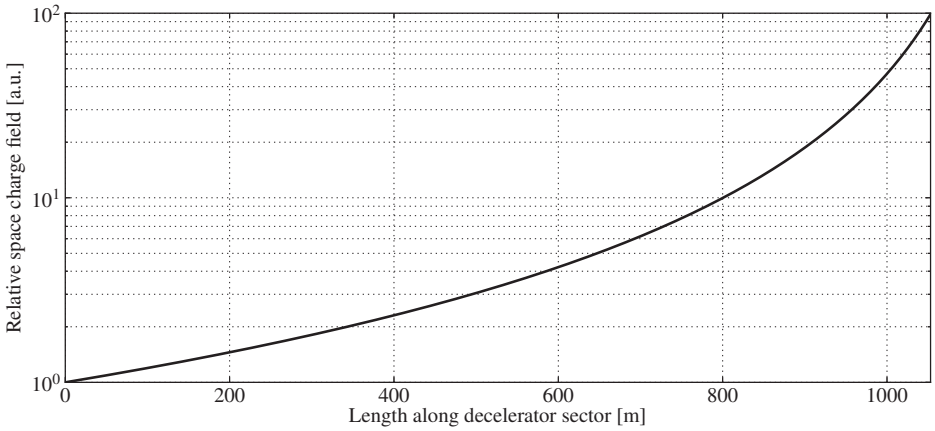

Figure 6.1: Analytical space charge field along a decelerator sector, normalized to the field at the beginning of the beamline.

Equations (2.5–2.6) describe analytical formulae, and show that the electric field is proportional to $1/\gamma^2$. Using this, we can plot the space charge field in a bunch along a decelerator sector, as shown in Figure 6.1. The curve is normalized to the field at the start of the decelerator. In the beam frame, the force on the particles in a bunch is proportional to the electrostatic field because the Lorentz force is simply $\vec{F} = q\vec{E}$ without a magnetic field. In the laboratory frame, the situation is a little more complicated because of the magnetic field induced by the moving bunch. The electric and magnetic field are almost equal at high energies, which leads to the strong suppression at the start of the beamline in Figure 6.1. As can be seen from the plot, the largest contribution to space charge occurs during the last 10–20 % of the length of the beamline.

6.2 Applied Particle-in-Cell framework

To study longitudinal space charge in the CLIC decelerators, a new simulation code was developed. This was partly due to the complexity and licence requirements of other existing codes. However, the main reason from the start was that the developed code should be added as a module to the already existing PLACET [44] code. PLACET is the main simulation tool used for CLIC beam dynamics. The space charge module was developed in OCTAVE, but due to time constraints it has not yet been integrated with PLACET, and is rather a stand-alone code.

The OCTAVE code was written using a Particle-in-Cell (PIC) framework, because PIC is a well-known scheme, that is intuitive and can be integrated with PLACET. In PIC, the physical volume under consideration is divided into a number of *cells*, that together make up a *grid*. The fields and forces are calculated on the grid points, and the particles are then moved accordingly around the grid. The next sections detail how this is done in the developed code. Some preliminary results were presented in [47], which is included in Appendix A.3.

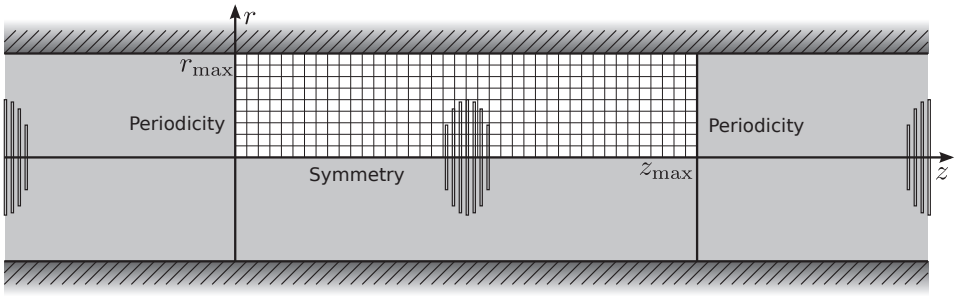

Figure 6.2: The model used in the simulation code, which uses a cylindrical (r, z) coordinate system. The code uses a symmetric boundary condition on the axis, a metallic boundary condition on the vacuum pipe, and periodic boundary conditions in the longitudinal dimension.

6.2.1 Model

In the PIC model, the number of physical dimensions is important, and influences the physical model and the computation time of the code. A 1-dimensional code is the simplest, and to simulate longitudinal space charge one could choose a code using the longitudinal z-coordinate. Such a code can be computationally fast, but it has some shortcomings. First of all, the results for a particle bunch of finite transverse size can be inaccurate, since the force on the particles only considers their longitudinal positions, and not their transverse separations. Also, 1-dimensional codes have unphysical long-range Coulomb forces [48], where the field does not decrease with distance from the particles.

On the other side of the spectrum is 3-dimensional codes, which could use either cartesian coordinates or other coordinates such as cylindrical. These should provide the most physically accurate solutions, but the computational requirements are high. The computer memory requirements are proportional to the square of the number of grid points, and CPU requirements can also be significantly higher because of the more complex computations.

Between the two extremes discussed are 2-dimensional codes. These can serve as a tradeoff between accuracy and computational requirements. Because the Octave code was originally made to be integrated with Placet, this compromise was seen as a reasonable choice. The choice of coordinates was one longitudinal coordinate z, together with one radial coordinate r, that together give a cylindrical coordinate system. Because of the single radial coordinate one has to assume an axisymmetric bunch, but this was seen as a valid approximation for the CLIC drive beam decelerator that consists of a FODO lattice. The (r, z) system also provides an intuitive way to implement boundary conditions, given that bunches stay close to the vacuum pipe axis.

An illustration of the 2-dimensional model is shown in Figure 6.2. The r coordinate spans from the axis to the edge of the vacuum pipe, which in the CLIC case is at a radius of 11.5 mm. The z coordinate spans a total length equal to the bunch spacing, which in CLIC is 25 mm. The bunch itself is placed on axis, in the middle of the longitudinal space.

In all electromagnetic codes it is important to set reasonable boundary conditions (BCs). In our code these come into play during the calculation of the potential. For the four boundaries in the model, the BCs were chosen as follows,

- For $r = 0$ (on the vacuum pipe axis), a symmetric BC was chosen. This boundary acts like a 'mirror', where imaginary grid points outside the model would be equal to the grid points inside, an equal distance from the boundary.
- The maximum r coordinate, $r = r_{\max}$, is placed at the vacuum pipe radius. Here a Dirichlet BC was chosen, where the potential is forced to zero. This means that the metallic vacuum pipe is grounded. One reason for this choice is that the potential must always be fixed somewhere on the grid, to ensure a single solution to the partial differential equations.
- The two longitudinal boundaries, at $z = 0$ and $z = z_{\max}$, have periodic BCs. This means that any grid points outside the system would be taken from the other side of the grid. In this case, a bunch placed outside the center of the system will not change the solution significantly, since the 'mirror bunches' outside the system would move with it.

The model is set up at the start of a simulation, including a grid of a specified size with a number of macro particles inside. However, because of length contraction the longitudinal dimension is scaled with the Lorentz factor along the beamline. After that the code iterates over a number of timesteps necessary for numerical stability. The calculation during each timestep is performed in the beam frame, in order to reduce the system to an electrostatic problem, and avoid the magnetic fields associated with a relativistic bunch. The necessary number of timesteps is given in the beam frame by the Courant-Levy stability criterion [49, 50]. For our 2-dimensional problem the longest possible timestep is

$$\delta_t \leq \frac{1}{c}\left(\frac{1}{\Delta_r^2} + \frac{1}{\Delta_z^2}\right)^{-1/2}. \tag{6.1}$$

The number of timesteps depends on the traveling time of the bunch in the beam frame. Since the Lorentz factor changes significantly along a decelerator, the number of timesteps will change along the machine, as described later.

The following sections walk through some of the main calculations performed during each timestep.

6.2.2 Charge assignment to the grid

The macro particles of the bunch are generally not placed exactly on the grid points of the model, but rather somewhere in between. In order to solve the partial differential equations during the calculations of potential and electric field, it is necessary to first interpolate the charge of the particles onto the grid points. For our code a linear interpolation scheme was chosen, which provides a good tradeoff between accuracy and numerical complexity.

An illustration of the linear weighting scheme is shown in Figure 6.3. Here a single particle is shown, surrounded by the four closest grid points. The distances to the lines between the grid points are calculated, and from that the four areas A_1, A_2, A_3 and A_4 can be calculated. Then, each of the four grid points gets assigned a fraction of the particle charge corresponding to the area farthest away from it. For example, the lower left grid points is assigned a fraction $A_2/(A_1 + A_2 + A_3 + A_4)$ of the particle charge. It will therefore have the highest charge out of the four grid points, which is reasonable since it is the closest to the particle.

The linear weighting shown in Figure 6.3 is performed for all macro particles in the bunch, and therefore the total charge assigned to the grid is the same as the total bunch charge. The

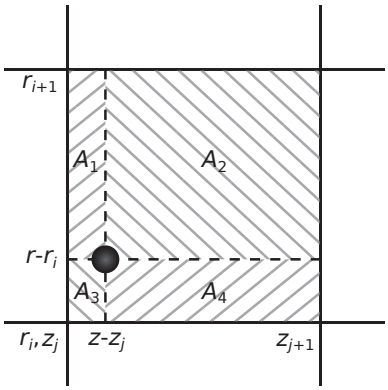

Figure 6.3: Linear weighting of electric charge onto grid points. Each of the four grid points receives a fraction of the macro particle charge corresponding to the area farthest away.

charge on the grid at the beginning of a CLIC decelerator is shown in Figure 6.4, calculated with the OCTAVE code. Even though the calculation is performed in the beam frame, the figure shows the longitudinal coordinate in the laboratory frame.

6.2.3 Calculating charge density

An important part of the calculation during each timestep is to solve Poisson's equation, and for this we need to know the charge density everywhere on the grid. Charge density is here defined as charge divided by volume, since each grid point in the 2-dimensional model corresponds to a volume in 3D space.

We will in the following denote grid points along the r dimensions with the index i, and grid points along the z dimension with the index j. The separations between grid points in each dimension will be denoted Δ_r and Δ_z. Following [51], a grid point at $r = r_i$, $z = z_j$ corresponds to the following volume,

$$\mathscr{V}_{i,j} = L_{r_i} L_{z_j}, \tag{6.2}$$

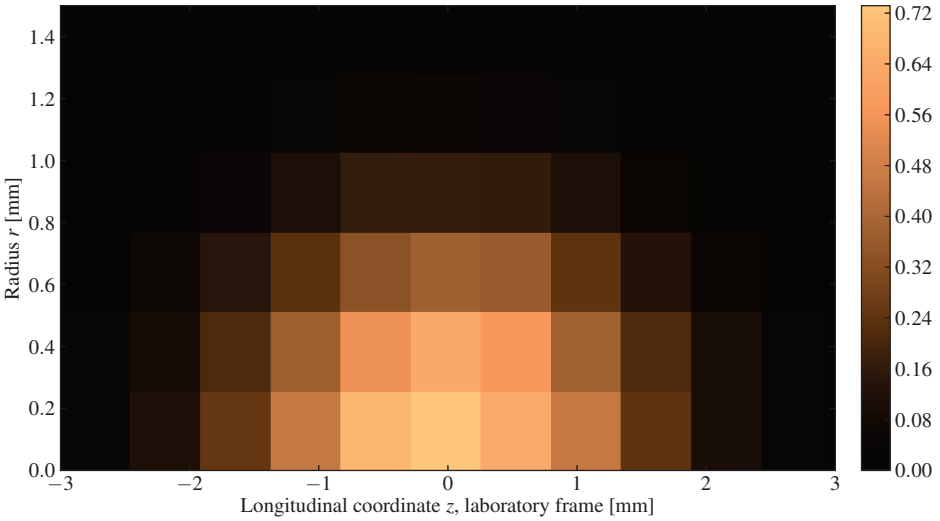

Figure 6.4: Charge on the grid points close to a bunch at the beginning of a CLIC decelerator, in nC. Only the area close to the bunch is shown, and the longitudinal coordinate has been changed from the beam frame to the laboratory frame.

where the radial length is

$$
\begin{aligned}
L_{r_i} &= \frac{2\pi}{\Delta_r}\left(\int_{r_{i-1}}^{r_i} r(r-r_{i-1})\,\mathrm{d}r + \int_{r_i}^{r_{i+1}} r(r_{i+1}-r)\,\mathrm{d}r\right) \\
&= \frac{2\pi}{\Delta_r}\left(\left[\frac{r^3}{3}-\frac{r^2}{2}r_{i-1}\right]_{r_{i-1}}^{r_i} + \left[\frac{r^2}{2}r_{i+1}-\frac{r^3}{3}\right]_{r_i}^{r_{i+1}}\right) \\
&= \frac{2\pi}{\Delta_r}\left(\frac{2}{3}r_i^3 + \frac{1}{6}r_{i-1}^3 + \frac{1}{6}r_{i+1}^3 - \frac{1}{2}r_i^2(r_{i-1}+r_{i+1})\right) \\
&= \frac{2\pi}{\Delta_r}\left(\frac{2}{3}r_i^3 + \frac{1}{6}(r_i-\Delta_r)^3 + \frac{1}{6}(r_i+\Delta_r)^3 - \frac{1}{2}r_i^2(r_i-\cancel{\Delta_r}+r_i+\cancel{\Delta_r})\right) \\
&= \frac{2\pi}{\Delta_r}\left(\cancel{\frac{2}{3}r_i^3} + \frac{1}{6}(\cancel{r_i^3} - \cancel{3r_i^2\Delta_r} + 3r_i\Delta_r^2 - \cancel{\Delta_r^3}) + \frac{1}{6}(\cancel{r_i^3} + \cancel{3r_i^2\Delta_r} + 3r_i\Delta_r^2 + \cancel{\Delta_r^3}) - \cancel{r_i^3}\right) \\
&= 2\pi r_i\Delta_r,
\end{aligned}
\tag{6.3}
$$

and the longitudinal length is

$$\begin{aligned}
L_{z_j} &= \frac{1}{\Delta_z}\left(\int_{z_{j-1}}^{z_j}(z-z_{j-1})\,\mathrm{d}z + \int_{z_j}^{z_{j+1}}(z_{j+1}-z)\,\mathrm{d}z\right)\\
&= \frac{1}{\Delta_z}\left(\left[\frac{z^2}{2}-z_{j-1}z\right]_{z_{j-1}}^{z_j} + \left[z_{j+1}z-\frac{z^2}{2}\right]_{z_j}^{z_{j+1}}\right)\\
&= \frac{1}{\Delta_z}\left(z_j^2-\frac{1}{2}z_{j-1}^2-z_jz_{j-1}+z_{j-1}^2+z_{j+1}^2-z_jz_{j+1}-\frac{1}{2}z_{j+1}^2\right)\\
&= \frac{1}{\Delta_z}\left(z_j^2+\frac{1}{2}(z_j-\Delta_z)^2-z_j(z_j-\Delta_z)+\frac{1}{2}(z_j+\Delta_z)^2-z_j(z_j+\Delta_z)\right)\\
&= \frac{1}{\Delta_z}\left(\cancel{z_j^2}+\frac{1}{2}\cancel{z_j^2}-\cancel{z_j\Delta_z}+\frac{1}{2}\Delta_z^2-\cancel{z_j^2}+\cancel{z_j\Delta_z}+\frac{1}{2}\cancel{z_j^2}+\cancel{z_j\Delta_z}+\frac{1}{2}\Delta_z^2-\cancel{z_j^2}-\cancel{z_j\Delta_z}\right)\\
&= \Delta_z.
\end{aligned} \tag{6.4}$$

The volume element for the grid point is therefore

$$\mathscr{V}_{i,j} = L_{r_i}L_{z_j} = 2\pi r_i\Delta_r\Delta_z. \tag{6.5}$$

This volume element can be seen as a torus of radius r_i, where the cross-section is specified by the rectangle $\Delta_r\Delta_z$.

The volume element in Equation (6.5) is valid inside the grid, but the edge points need special treatment. For the $r=0$ axis we get [51], for the radial length,

$$L_{r_0} = \frac{2\pi}{\Delta_r}\int_0^{r_1} r(r_1-r)\,\mathrm{d}r = \frac{2\pi}{\Delta_r}\left[\frac{r^2}{2}r_1-\frac{r^3}{3}\right]_0^{r_1} = \frac{2\pi}{\Delta_r}\left(\frac{r_1^3}{2}-\frac{r_1^3}{3}\right) = \frac{2\pi}{\Delta_r}\frac{\Delta_r^3}{6} = \frac{\pi\Delta_r^2}{3}. \tag{6.6}$$

This expression should again be multiplied with Equation (6.4). The resulting volume element is a cylinder with radius $\Delta_r/\sqrt{3}$ and length Δ_z.

For the pipe wall, where $r = r_{\max}$, we get

$$\begin{aligned}
L_{r_{\max}} &= \frac{2\pi}{\Delta_r}\int_{r_{\max-1}}^{r_{\max}} r(r-r_{\max-1})\,\mathrm{d}r\\
&= \frac{2\pi}{\Delta_r}\left[\frac{r^3}{3}-\frac{r^2}{2}r_{\max-1}\right]_{r_{\max-1}}^{r_{\max}}\\
&= \frac{2\pi}{\Delta_r}\left(\frac{r_{\max}^3}{3}-\frac{r_{\max-1}^3}{3}-\frac{r_{\max}^2}{2}r_{\max-1}+\frac{r_{\max-1}^3}{2}\right)\\
&= \frac{2\pi}{\Delta_r}\left(\frac{r_{\max}^3}{3}+\frac{r_{\max-1}^3}{6}-\frac{r_{\max}^2}{2}r_{\max-1}\right)\\
&= \frac{2\pi}{\Delta_r}\left(\frac{1}{3}r_{\max}^3+\frac{1}{6}(r_{\max}-\Delta_r)^3-\frac{1}{2}r_{\max}^2(r_{\max}-\Delta_r)\right)\\
&= \frac{2\pi}{\Delta_r}\left(\cancel{\frac{1}{3}r_{\max}^3}+\cancel{\frac{1}{6}r_{\max}^3}-\cancel{\frac{1}{2}r_{\max}^2\Delta_r}+\frac{1}{2}r_{\max}\Delta_r^2-\frac{1}{6}\Delta_r^3-\cancel{\frac{1}{2}r_{\max}^3}+\cancel{\frac{1}{2}r_{\max}^2\Delta_r}\right)\\
&= \frac{2\pi}{\Delta_r}\left(\frac{1}{2}\Delta_r^2\left(r_{\max}-\frac{\Delta_r}{3}\right)\right)\\
&= \pi\Delta_r\left(r_{\max}-\frac{\Delta_r}{3}\right).
\end{aligned} \tag{6.7}$$

When multiplying Equation (6.7) with Equation (6.4), we get less than half the volume found in Equation (6.5), as expected from a geometry standpoint.

At the left boundary in the longitudinal dimension we get

$$L_{z_0} = \frac{1}{\Delta_z}\int_0^{z_1}(z_1 - z)\,\mathrm{d}z = \frac{1}{\Delta_z}\left[z_1 z - \frac{z^2}{2}\right]_0^{z_1} = \frac{1}{\Delta_z}(z_1^2 - \frac{z_1^2}{2}) = \frac{z_1^2}{2\Delta_z} = \frac{\Delta_z}{2}, \tag{6.8}$$

and at the right boundary we get

$$\begin{aligned} L_{z_{\max}} &= \frac{1}{\Delta_z}\int_{z_{\max-1}}^{z_{\max}}(z - z_{\max-1})\,\mathrm{d}z \\ &= \frac{1}{\Delta_z}\left[\frac{z^2}{2} - z_{\max-1}\,z\right]_{z_{\max-1}}^{z_{\max}} \\ &= \frac{1}{\Delta_z}\left(\frac{z_{\max}^2}{2} - \frac{z_{\max-1}^2}{2} - z_{\max}z_{\max-1} + z_{\max-1}^2\right) \\ &= \frac{1}{\Delta_z}\left(\frac{z_{\max}^2}{2} + \frac{z_{\max-1}^2}{2} - z_{\max}z_{\max-1}\right) \\ &= \frac{1}{2\Delta_z}\left(z_{\max} - z_{\max-1}\right)^2 \\ &= \frac{\Delta_z}{2}. \end{aligned} \tag{6.9}$$

When one of Equations (6.8) or (6.9) is multiplied with Equation (6.3), the resulting volume element is half that of Equation (6.5), as would be expected.

The volume elements for the four corners of the grid are found by multiplying the two nearby boundary expressions, given in Equations (6.6–6.9). Finally, the charge density is found everywhere on the grid by dividing the charge assigned on the grid points by the respective volume elements.

6.2.4 Solving Poisson's equation

One of the major functions of the PIC code that was developed in Octave is the fieldsolver, which solves Poisson's equation everywhere on the grid. If the potential is ϕ, the charge density ρ, and the electric permittivity in vacuum ϵ_0, Poisson's equation is generally given by $\nabla^2\phi = -\rho/\epsilon_0$. In cylindrical coordinates we can write the Laplacian

$$\nabla^2\phi = \left[\frac{1}{r}\frac{\partial}{\partial r}\left(r\frac{\partial}{\partial r}\right) + \frac{1}{r^2}\frac{\partial^2}{\partial\theta^2} + \frac{\partial^2}{\partial z^2}\right]\phi = \left[\frac{1}{r}\frac{\partial}{\partial r} + \frac{\partial^2}{\partial r^2} + \frac{1}{r^2}\frac{\partial^2}{\partial\theta^2} + \frac{\partial^2}{\partial z^2}\right]\phi. \tag{6.10}$$

This expression also includes the azimuthal coordinate θ. However, since we assume axisymmetry, $\partial\phi/\partial\theta = 0$ and we write Poisson's equation as

$$\nabla^2\phi = \left[\frac{1}{r}\frac{\partial}{\partial r} + \frac{\partial^2}{\partial r^2} + \frac{\partial^2}{\partial z^2}\right]\phi = -\frac{\rho}{\epsilon_0}. \tag{6.11}$$

In the finite difference approximation, the partial derivatives in Equation (6.11) can be expressed by numerical equivalents. As an example, the simplest form of the first derivative in

the radial direction at the coordinate $(i,\, j)$ on the grid can be written

$$\left.\frac{\partial\phi}{\partial r}\right|_{i,j} \approx \frac{\phi_{i+1,j} - \phi_{i-1,j}}{2\Delta_r}. \tag{6.12}$$

Here $\phi_{i,j}$ is the yet unknown potential at grid point $(i,\, j)$. As will be shown later, the type of numerical differentiation in Equation (6.12) did not give satisfactory accuracy for some particle distributions. Therefore, a more advanced numerical differentiation was employed, that depends on more grid points. Poisson's equation is therefore approximated as

$$\begin{aligned}\left.\nabla^2\phi\right|_{i,j} \approx \frac{1}{r_i}&\frac{\phi_{i-2,j} - 8\phi_{i-1,j} + 8\phi_{i+1,j} - \phi_{i+2,j}}{12\Delta_r} \\ &+ \frac{-\phi_{i-2,j} + 16\phi_{i-1,j} - 30\phi_{i,j} + 16\phi_{i+1,j} - \phi_{i+2,j}}{12\Delta_r^2} \\ &+ \frac{-\phi_{i,j-2} + 16\phi_{i,j-1} - 30\phi_{i,j} + 16\phi_{i,j+1} - \phi_{i,j+2}}{12\Delta_z^2},\end{aligned} \tag{6.13}$$

everywhere inside the grid.

The four boundaries require special treatment, given by the BCs in Equations (6.6–6.9). Firstly, for $r = 0$ we have a symmetric boundary condition where $\phi_{-i,j} = \phi_{i,j}, \forall i$. This reduces Equation (6.13) to

$$\left.\nabla^2\phi\right|_{0,j} \approx \frac{-30\phi_{0,j} + 32\phi_{1,j} - 2\phi_{2,j}}{12\Delta_r^2} + \frac{-\phi_{0,j-2} + 16\phi_{0,j-1} - 30\phi_{0,j} + 16\phi_{0,j+1} - \phi_{0,j+2}}{12\Delta_z^2}. \tag{6.14}$$

At the vacuum pipe where $r = r_{\max}$, the potential is forced to zero, $\phi_{r_{\max},j} = \phi_{r_{\max+1},j} = \cdots = 0$. Equation (6.13) is then reduced to

$$\begin{aligned}\left.\nabla^2\phi\right|_{r_{\max},j} \approx \frac{1}{r_i}&\frac{\phi_{r_{\max}-2,j} - 8\phi_{r_{\max}-1,j}}{12\Delta_r} + \frac{-\phi_{r_{\max}-2,j} + 16\phi_{r_{\max}-1,j} - 30\phi_{r_{\max},j}}{12\Delta_r^2} \\ &+ \frac{-\phi_{r_{\max},j-2} + 16\phi_{r_{\max},j-1} - 30\phi_{r_{\max},j} + 16\phi_{r_{\max},j+1} - \phi_{r_{\max},j+2}}{12\Delta_z^2}.\end{aligned} \tag{6.15}$$

For $z = 0$ we have periodicity, which causes $\phi_{i,-j} = \phi_{i,z_{\max}-j}, \forall j$. Poisson's equation is then

$$\begin{aligned}\left.\nabla^2\phi\right|_{i,0} \approx \frac{1}{r_i}&\frac{\phi_{i-2,0} - 8\phi_{i-1,0} + 8\phi_{i+1,0} - \phi_{i+2,0}}{12\Delta_r} \\ &+ \frac{-\phi_{i-2,0} + 16\phi_{i-1,0} - 30\phi_{i,0} + 16\phi_{i+1,0} - \phi_{i+2,0}}{12\Delta_r^2} \\ &+ \frac{-\phi_{i,z_{\max}-2} + 16\phi_{i,z_{\max-1}} - 30\phi_{i,0} + 16\phi_{i,1} - \phi_{i,2}}{12\Delta_z^2},\end{aligned} \tag{6.16}$$

and similarly for the $z = z_{\max}$ boundary,

$$\begin{aligned}\left.\nabla^2\phi\right|_{i,z_{\max}} \approx \frac{1}{r_i}&\frac{\phi_{i-2,z_{\max}} - 8\phi_{i-1,z_{\max}} + 8\phi_{i+1,z_{\max}} - \phi_{i+2,z_{\max}}}{12\Delta_r} \\ &+ \frac{-\phi_{i-2,z_{\max}} + 16\phi_{i-1,z_{\max}} - 30\phi_{i,z_{\max}} + 16\phi_{i+1,z_{\max}} - \phi_{i+2,z_{\max}}}{12\Delta_r^2} \\ &+ \frac{-\phi_{i,z_{\max}-2} + 16\phi_{i,z_{\max}-1} - 30\phi_{i,z_{\max}} + 16\phi_{i,1} - \phi_{i,2}}{12\Delta_z^2}\end{aligned} \tag{6.17}$$

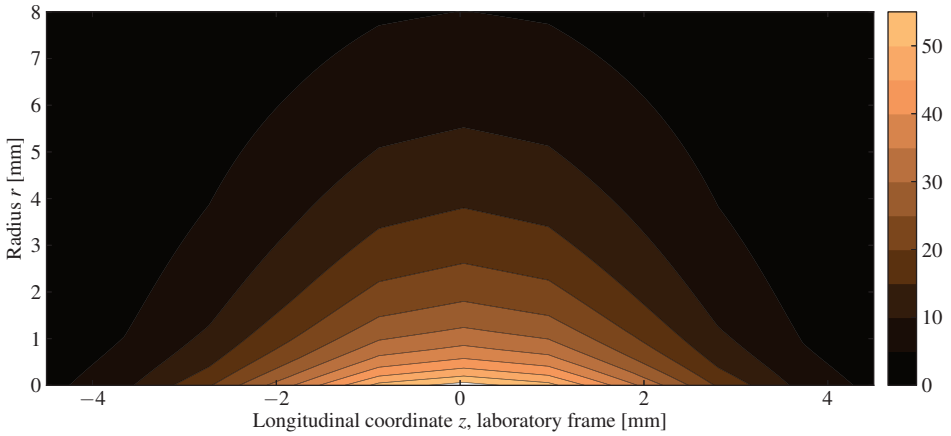

Figure 6.5: The potential ϕ in V close to a bunch at the beginning of a CLIC decelerator sector, calculated with the Poisson field solver from the OCTAVE code.

The four corners will use a combination of terms from Equations (6.14–6.17). Also all grid points right next to the boundaries will use similar terms, because of the advanced numerical differentiation scheme.

For each point on the grid, one numerical Poisson equation needs to be solved, that depends on the potential on the nearby grid points. If the total number of grid points is N_G, we therefore have N_G equations and N_G unknowns. This allows us to write the whole system as a matrix equation $\mathbf{A}\,\vec{\phi} = -\vec{\rho}/\epsilon_0$, where $\vec{\phi}$ and $\vec{\rho}$ are vectors containing the potential and the charge density on all grid points, respectively. The matrix $\mathbf{A}$ contains all coefficients from Equations (6.13–6.17), and is a square matrix with $N_\mathrm{G} \times N_\mathrm{G}$ elements.

The coefficient matrix is stored in memory, and we see that a large grid leads to a very large memory requirement. As an example, when the number of grid points in each dimension is doubled, N_G will be quadrupled, which finally leads to a 16-fold increase of $\mathbf{A}$. However, since each row of the matrix contains at most 9 coefficients, the matrix is sparse. This will therefore reduce the memory requirements in programming languages like OCTAVE, when exploited with specific commands.

The unknown in the matrix equation is $\vec{\phi}$, which means that $\mathbf{A}$ must be inverted in order to solve the equation. A large grid therefore also affects the computation time significantly. Fortunately, the sparsity of $\mathbf{A}$ again helps since fast numerical algorithms can be applied. In the OCTAVE code, a number of possible algorithms were identified and analyzed for speed. For large grids, one method significantly outperformed the others, and was therefore chosen[1]. This was the *incomplete LU decomposition* of the coefficient matrix.

The calculated potential from the field solver is shown in Figure 6.5. The potential was calculated from the charge in Figure 6.4, on a grid with 61×51 grid points (representing the dimensions r and z, respectively). The Gaussian CLIC bunch center is placed at $r = z = 0$, and the potential is zero at the grounded vacuum pipe, as it should be.

[1]If small grids would be needed, other algorithms can be faster. However, since the computation time in that case is much shorter, the choice of algorithm will not matter to the same degree.

6.2.5 Solving for the electric field

The space charge effect depends on the electric self-field of a bunch, as discussed in Section 2.1. The electric field can be expressed from the potential as $\vec{E} = -\nabla\phi$. Since we assume axisymmetry, $\frac{\partial\phi}{\partial\theta} = 0$ and we generally express the electric field as

$$\vec{E} = -\nabla\phi = -\frac{\partial\phi}{\partial r}\hat{r} - \frac{\partial\phi}{\partial z}\hat{z}, \tag{6.18}$$

where $\hat{r}$ and $\hat{z}$ denote unit vectors in the two dimensions.

Again using the finite difference approximation, the two field components inside the grid, for a point $(i,\, j)$, are then

$$E_r|_{i,j} \approx \frac{-\phi_{i-2,j} + 8\phi_{i-1,j} - 8\phi_{i+1,j} + \phi_{i+2,j}}{12\Delta_r}, \tag{6.19a}$$

$$E_z|_{i,j} \approx \frac{-\phi_{i,j-2} + 8\phi_{i,j-1} - 8\phi_{i,j+1} + \phi_{i,j+2}}{12\Delta_z}. \tag{6.19b}$$

Since these are only first derivatives, the radial field at the axis is zero. For the vacuum pipe, which has a Dirichlet BC, we have

$$E_r|_{r_{\max},j} \approx \frac{-\phi_{r_{\max}-2,j} + 8\phi_{r_{\max}-1,j}}{12\Delta_r}. \tag{6.20}$$

For the two longitudinal boundaries, we get

$$E_z|_{i,0} = E_z|_{i,z_{\max}} \approx \frac{-\phi_{i,z_{\max}-2} + 8\phi_{i,z_{\max}-1} - 8\phi_{i,1} + \phi_{i,2}}{12\Delta_z}. \tag{6.21}$$

For each of the two field components, we again get one equation and one unknown per grid point. This means that we can write everything as matrix equations,

$$\mathbf{D}_r\vec{\phi} = \vec{E}_r, \tag{6.22a}$$

$$\mathbf{D}_z\vec{\phi} = \vec{E}_z, \tag{6.22b}$$

where $\mathbf{D}_r$ and $\mathbf{D}_z$ are coefficient matrices of size $N_\mathrm{G} \times N_\mathrm{G}$, and $\vec{E}_r$ and $\vec{E}_z$ are vectors containing the field components on all the grid points. Note that in Equation (6.22), the field components are the unknowns. Therefore, no matrix inversions are needed for solving the equations, and the computation is significantly faster than for solving Poisson's equation.

The longitudinal and the radial electric field components for a bunch in a CLIC decelerator are shown in Figures 6.6 and 6.7, respectively. The longitudinal field is strongest on axis, around one standard deviation from the bunch center ($\sigma_z = 1$ mm). Also, it has opposite signs on each side of the bunch, as it should. The radial field is zero on axis, and is strongest about one standard deviation of the bunch distribution from the axis.

Once the electric field is known everywhere on the grid, a linear interpolation is done to find the electric field on the position of each particle. Since the distances from the particles to the grid points were calculated earlier, together with the areas shown in Figure 6.3, we simply need to apply the same numbers in order to find the electric field on the particles. This is needed for calculating the force, as described below.

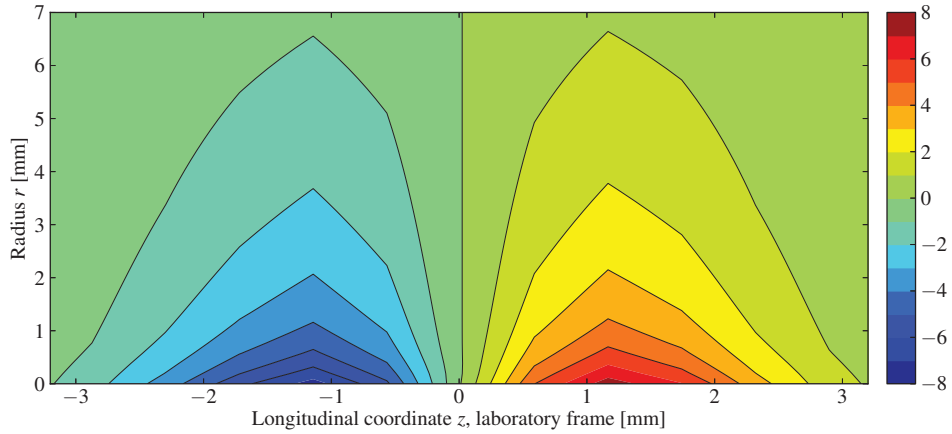

Figure 6.6: Longitudinal electric field in V/m close to a bunch at the beginning of a CLIC decelerator. The abscissa has been scaled to the laboratory frame.

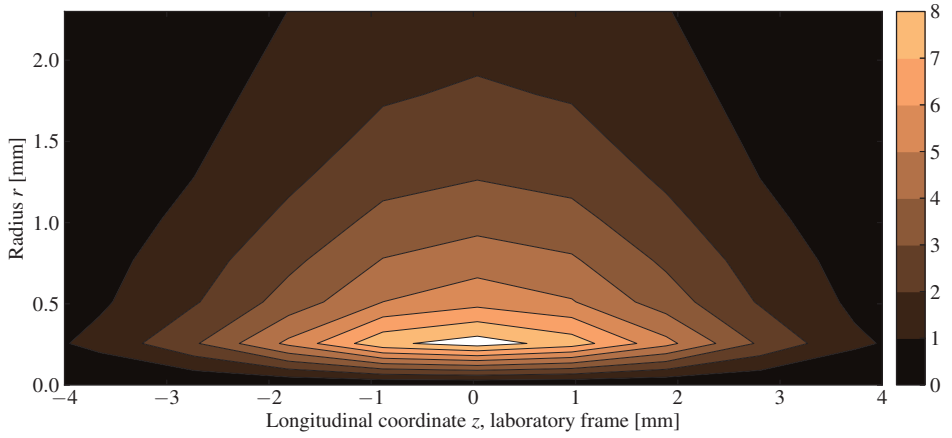

Figure 6.7: Radial electric field in V/m (in the laboratory frame) close to a bunch at the beginning of a CLIC decelerator. The abscissa has been scaled to the laboratory frame.

6.2.6 Calculating particle kicks

In order to calculate the influence of space charge on the particles, we first need to know the force on each particle. Since the code operates in the beam frame, the Lorentz force is simply proportional to the electric field there,

$$\vec{F} = q_\mathrm{p}(\vec{E} + \vec{\beta}c \times \cancelto{0}{\vec{B}}) = q_\mathrm{p}\vec{E}, \tag{6.23}$$

where q_p is the charge of a macro particle.

Since we already know the electric field at all the particle positions, the two components F_r and F_z of the force on each particle are found simply by multiplying with the macro particle charge. Using Newton's second law, the acceleration a_r and a_z in the two dimensions is then given by

$$a_r = \frac{F_r}{m_\mathrm{p}} = \frac{q_\mathrm{p}}{m_\mathrm{p}} E_r, \tag{6.24a}$$

$$a_z = \frac{F_z}{m_\mathrm{p}} = \frac{q_\mathrm{p}}{m_\mathrm{p}} E_z, \tag{6.24b}$$

where m_p is the macro particle mass.

The OCTAVE code uses the *Leapfrog algorithm*, which is a symplectic integrator. The main feature of this integrator is that it updates particle velocities and positions alternatively, with positions updated at integer timesteps and velocities updated at half timesteps in between.

The acceleration in Equation (6.24) can be written as the derivative of the velocity. Using the finite difference method, in the longitudinal plane we can write

$$\frac{v_r(t_n + \delta_t/2) - v_r(t_n - \delta_t/2)}{\delta_t} = \frac{q_\mathrm{p}}{m_\mathrm{p}} E_r, \tag{6.25a}$$

$$\frac{v_z(t_n + \delta_t/2) - v_z(t_n - \delta_t/2)}{\delta_t} = \frac{q_\mathrm{p}}{m_\mathrm{p}} E_z, \tag{6.25b}$$

where v_r and v_z are the velocities in the two dimensions in the beam frame, t_n is the time at the arbitrary timestep number n and δ_t is the timestep length. Note that the velocities in Equation (6.25) are expressed at timesteps $t_n + \delta_t/2$ and $t_n - \delta_t/2$, and therefore not at integer timesteps, in accordance with the leapfrog scheme.

Rearranging Equation (6.25), we have

$$v_r(t_n + \delta_t/2) = \frac{q_\mathrm{p}}{m_\mathrm{p}} \delta_t E_r + v_r(t - \delta_t/2), \tag{6.26a}$$

$$v_z(t_n + \delta_t/2) = \frac{q_\mathrm{p}}{m_\mathrm{p}} \delta_t E_z + v_z(t - \delta_t/2). \tag{6.26b}$$

The velocities at time $t_n + \delta_t/2$ can therefore be expressed as the velocities at the previous timestep, $t_n - \delta_t/2$, plus an additional kick based on the electric field.

The particle positions can be expressed as derivatives of the velocities. Again using the finite difference approximation, we have

$$v_r(t_n + \delta_t/2) \approx \frac{x_r(t_n + \delta_t) - x_r(t_n)}{\delta_t} \tag{6.27a}$$

$$v_z(t_n + \delta_t/2) \approx \frac{x_z(t_n + \delta_t) - x_z(t_n)}{\delta_t}, \tag{6.27b}$$

where x_r and x_z are the particle positions in the two dimensions. Note that the positions use the integer timesteps t_n and $t_n + \delta_t$. Rearranging, the positions at timestep $t_n + \delta_t$ can also be expressed as an iterative relation, in the same way as for the velocity in Equation (6.26),

$$x_r(t_n + \delta_t) = v_r(t_n + \delta_t/2)\ \delta_t + x_r(t_n), \tag{6.28a}$$
$$x_z(t_n + \delta_t) = v_z(t_n + \delta_t/2)\ \delta_t + x_z(t_n). \tag{6.28b}$$

At certain timesteps, the code also gives the particles kicks from quadrupole focusing. Longitudinal space charge is stronger when particles are closer together transversally, since the magnitude of the Coulomb force is stronger and its direction is aimed more towards the longitudinal direction. This is an important reason for implementing focusing in the code. Calculations are performed at the start of the code, for which timesteps the particles encounter quadrupole magnets. During these timesteps, a thin lens approximation based on Equation (2.30) is used to either focus or defocus the bunch. Since the code assumes axisymmetry, the focusing scheme is the same in both planes, unlike a real decelerator FODO lattice in which the focusing alternates between the two transverse planes. The beta functions are therefore equal in the x and y planes in the PIC code.

Throughout the last sections we have described the operations performed during each timestep of the code, and they can be summarized as follows:

1. Interpolate charge from the macro particles to the grid.
2. Solve Poisson's equation everywhere on the grid, taking into account the four boundary conditions, to find the potential ϕ.
3. Calculate electric field components from the potential.
4. Interpolate the electric field components back to the particle positions.
5. Update the particle velocities at time $t_n + \delta_t/2$, based on the calculated fields with Equation (6.26).
6. For certain timesteps, add the kicks from quadrupole magnets to the space charge kicks as a superposition.
7. Update the particle positions at time $t_n + \delta_t$, based on the calculated velocities and Equation (6.28).

When particles are moved to the other side of the vacuum pipe axis, their transverse positions and velocities change sign, which corresponds to particles moving away from the bunch center on the other side of the bunch.

This cycle is iterated over a number of timesteps necessary to satisfy the Courant-Levy criterion in Equation (6.1). Each timestep takes around 3 seconds on the development computer, after the code was optimized for speed.

6.3 Code benchmarking

The Octave code has so far been benchmarked against some analytical models, and the results will be described below.

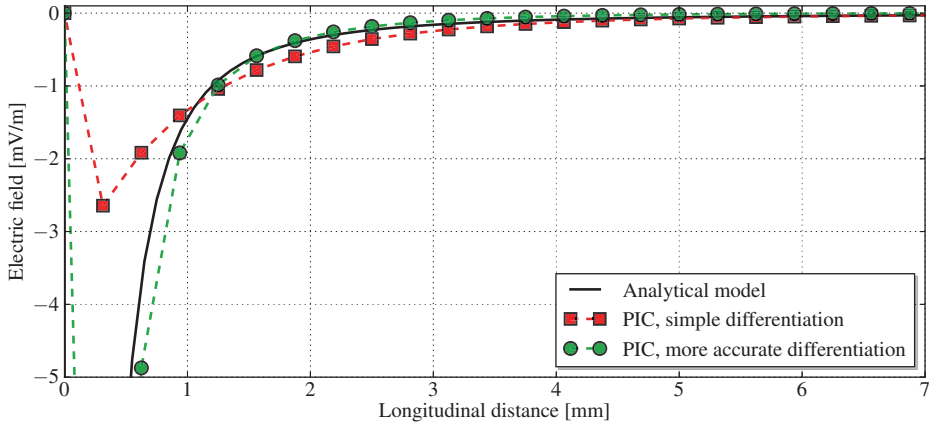

Figure 6.8: Longitudinal electric field of a point charge. The analytical model based on Coulomb's law is shown in black, and the result from the current version of the code is shown with green circles. The simple differentiation scheme discussed earlier is shown in red, and is less accurate.

Firstly, the case of a point charge was studied. The electric field from a point charge follows Coulomb's law, and is inversely proportional to the square of the distance to the particle. The analytical field from a stationary point particle is shown as a black line in Figure 6.8. The calculated field from the current version of the simulation code (for the same conditions) is shown in green. In this plot we also show the field calculated with the simpler differentiation scheme based on e.g. Equation (6.12). As seen from the figure, the more simple differentiation is not sufficient for abrupt changes in the potential and field. For this reason the more advanced differentiation scheme was chosen, as discussed in Section 6.2.4. This scheme is more accurate, and the largest deviation is close to the particle. Since the normal bunches should be more smooth than the point particle in this example, the deviation close to the asymptote should not be an issue.

Next, a continuos beam was studied, placed on axis. In this case, the chosen analytical model was the electric field from a wire, which is inversely proportional to the distance to the particle. The analytical model is shown in black in Figure 6.9. For comparison, the radial electric field calculated with the PIC code is shown with blue stars. We see that the deviation is largest closest to the beam, in the same way as in Figure 6.8.

The last analytical model was that of a Gaussian bunch distribution in the longitudinal dimension. In order to find a proper analytical model for this case, we started with a Gaussian curve, sliced it and performed a numerical integration based on the Coulomb field from each slice. This model is shown in black in Figure 6.10. In the PIC simulations, 10 000 macro particles were sampled from a Gaussian distribution. The accuracy of the result was found to depend on the radial resolution of the grid. As an example, the electric field calculated with a 41×51 grid in the code (corresponding to radial grid lengths of 0.29 mm) was inaccurate inside the bunch, although it converged outside. This can be seen with red squares in Figure 6.10.

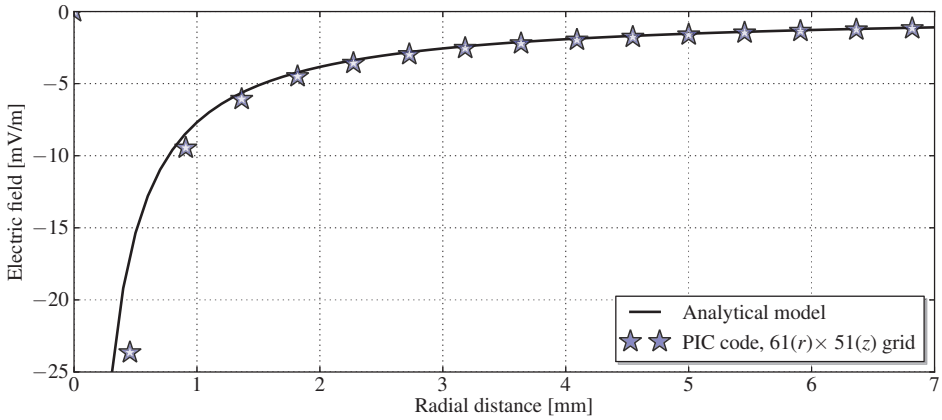

Figure 6.9: Radial electric field of a continuos beam. The analytical model (black) is based on the electric field from a wire and is shown in black, while the PIC code result is shown with blue stars.

A 61×51 grid gave a more accurate result[2], which is shown with green circles in Figure 6.10. The 61×51 grid was used in all simulations of the CLIC decelerator, discussed below.

6.4 Simulation results for the CLIC decelerators

We now turn our eyes to simulation results obtained for the CLIC decelerator. During these simulations, the model parameters were similar to those used previously in this chapter. A Gaussian bunch was simulated based on parameters in [10], and placed on a 61×51 grid in the PIC code. 10 000 macro particles were used for the bunch. As a worst-case scenario, we simulated the longest decelerator sector of 1053 m.

Firstly, the code calculated the number of timesteps needed for each energy step of the decelerator. In the beam frame, at the start of the decelerator, the minimum timestep length is found from Equation (6.1) and amounts to 0.64 ps. In principle this number is reduced along the decelerator, but because of length contraction in the z dimension the change is very small. Therefore, this number was kept constant throughout the simulation.

The time of flight of the bunch through each energy step can easily be calculated from the beam energy, and the code therefore calculates the number of timesteps needed per energy step. Each timestep is then never longer than 0.64 ps. The number of timesteps needed per energy steps is shown to the left in Figure 6.11, and we see that this number increases due to time dilation. The corresponding timestep lengths in the beam frame are shown to the right in the same figure, and feature a zig-zag pattern. This is because of the step-wise increase of the number of timesteps, and because the maximum timestep length is 0.64 ps.

With this simulation, the longitudinal bunch profile at the end of the decelerator sector

[2]One may think that an even higher radial resolution can lead to an overestimation of the field, based on the trend in Figure 6.10. However, within the possible grid size in OCTAVE, which used all allocatable memory, this was not found to be the case.

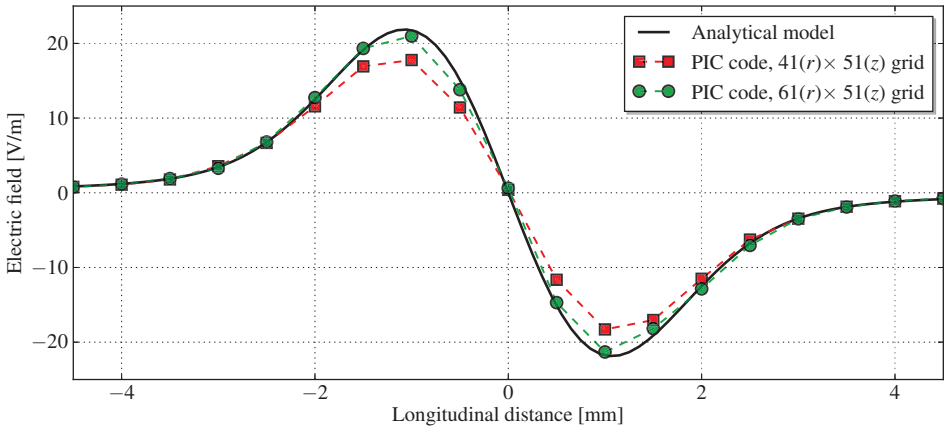

Figure 6.10: Longitudinal electric field of a gaussian bunch. The analytical model (black) was found by numerically integrating a Gaussian distribution. The PIC results are shown in red and green, for different radial grid resolutions. It was found that around 61 radial grid points were needed for sufficient accuracy.

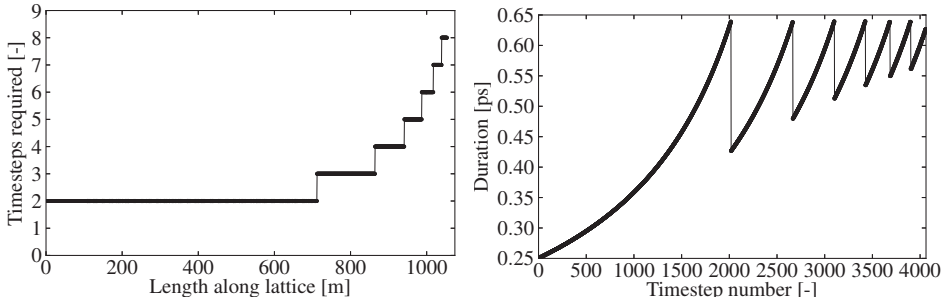

Figure 6.11: Left: The number of timesteps required for each energy step along a CLIC decelerator. Right: The corresponding lengths of each timestep in the beam frame.

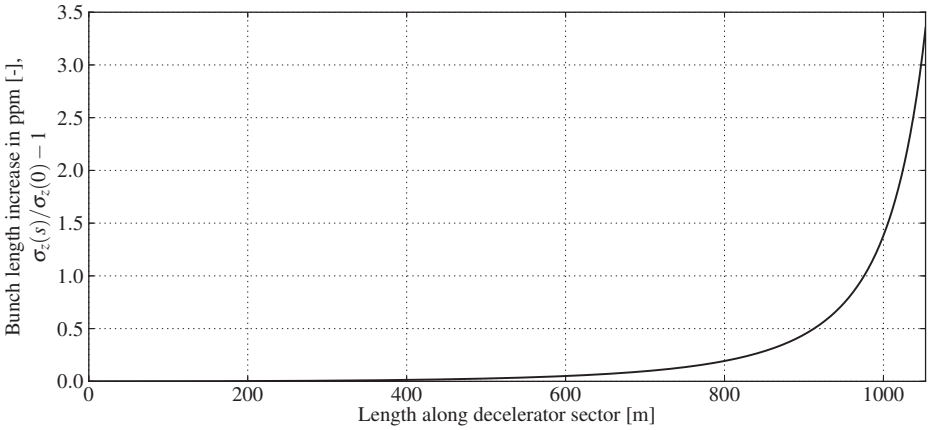

Figure 6.12: The increase in bunch length σ_z along a decelerator sector, normalized to the bunch length at the beginning of the beamline.

is very similar to that at the beginning of the beamline. The rms bunch length had only increased by 3.4 ppm at the end of the decelerator sector. This is likely due to the very high beam energy, and the number is well within the coherent bunch length tolerance of 1 %. The evolution of the bunch length along a decelerator sector is shown in Figure 6.12, and we see that the main contribution to the change is at the end, similarly to Figure 6.1.

Even though the main concern for CLIC is longitudinal space charge, we also show the transverse beam size σ_r along the decelerator sector, in Figure 6.13. Even though the transverse space charge is mostly kept in check by the thin lens quadrupole focusing, there is an increase in the transverse size because of adiabatic undamping. From the figure we can also see the periodic change of the transverse size that comes from the FODO lattice. Note that because we only have one transverse coordinate, the size changes equally in both cartesian transverse planes.

6.4.1 Comparison with the Test Beam Line

Even though it is not a feasibility issue, we can also study the effects of longitudinal space charge in the TBL. In this simulation we used the same PIC model, but beam and lattice parameters from Table 4.1. The result was an rms bunch length increase of 36 ppm, which is an order of magnitude higher than for the CLIC decelerator sector. This means that even for the significantly shorter beamline in the TBL, the lower energy is enough to make the bunch lengthening more compelling.

6.4.2 CLIC decelerator space charge limits

Since the simulation results in Section 6.4 show a very small effect from space charge, we can also study if a decelerator sector with more deceleration would violate the tolerances. In this simulation, we increased the deceleration of each PETS by 10 %, but kept the same length of the beamline. The energy was therefore reduced from 2.4 GeV to 24 MeV over 1053 m,

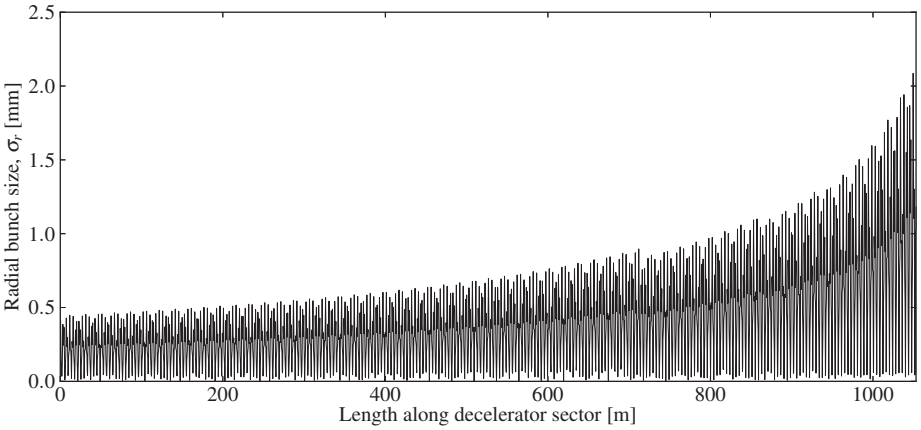

Figure 6.13: Transverse beam size σ_r along a decelerator sector. The increase in size at the end mainly comes from adiabatic undamping.

which led to a final Lorentz factor ten times lower than nominal. The resulting increase in bunch length was 0.37 ‰. Even though this is 2 orders of magnitude stronger than for the real decelerator, it is still more than an order of magnitude away from the tolerance.

The transverse beam distribution, however, changes much more than for the nominal decelerator. The radial bunch size σ_r is shown in Figure 6.14, and this can be compared to Figure 6.13. In the case with stronger deceleration, the adiabatic undamping is too severe for the available aperture, and the $3\,\sigma_r$ envelope starts to scrape the vacuum pipe 60 m before the end of the beamline. Therefore, we conclude that the maximum power extraction and therefore the efficiency of the drive beam scheme is not limited by longitudinal space charge, but rather by the transverse beam dynamics of the decelerator.

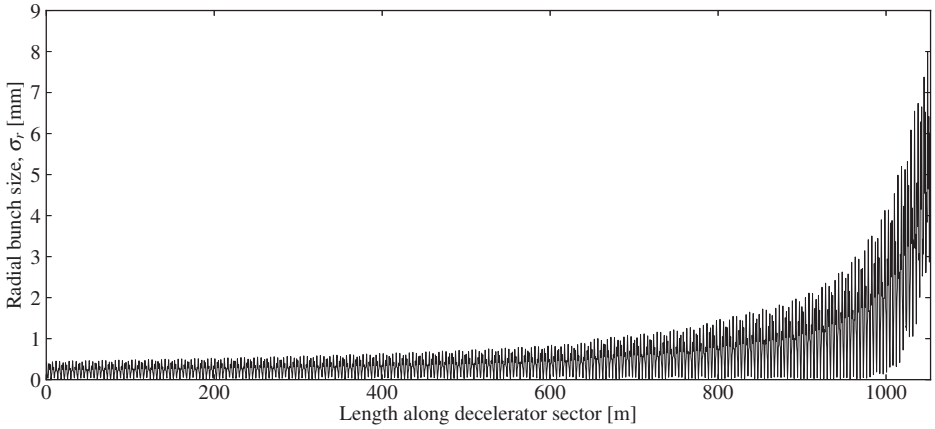

Figure 6.14: Transverse beam size σ_r along a decelerator sector, when the beam energy ends at 24 MeV. The beam size at the end is unacceptable and leads to a large loss of particles. Therefore, the limitation of the CLIC decelerator is transverse beam dynamics rather than longitudinal space charge.

Chapter 7

Conclusions and outlook

This thesis has presented research related to the heart of the CLIC scheme – the energy extraction from an electron drive beam, and the behavior of a beam undergoing strong deceleration. The results are part of the feasibility demonstration of the CLIC scheme.

Experiments performed at the Test Beam Line were presented, where an electron drive beam was decelerated through a series of PETS. Here, the most decelerated particles experienced up to 37 % deceleration from initial beam energies of 119 and 123.5 MeV. Two main data sets were discussed, where one was taken with the full bunch combination setup in the CTF3 and the other was taken at a lower combination setting.

The energy measurements were compared to predictions based on theoretical formulae together with measurements of the beam current and the power produced in the PETS. There was an excellent agreement between measurements and predictions of the energy. The same was the case for the power produced in the PETS, which was predicted based on beam current measurements.

In order to reach the good consistency between the different measurements, we have seen the importance of taking the bunch phase into account. The bunch phase affects the produced field in the PETS through the multi-bunch form factor, a quantity which was derived in the thesis. The CTF3 features a significant phase change over the bunch train because of its injector setup. Therefore, a reduction in PETS power and in deceleration must be expected, that also changes along the bunch train. When measurements are performed on a combined beam, the multi-bunch form factor must still be constructed from uncombined phase measurements, because information is otherwise lost.

The energy profile of the decelerated beam has also been found to agree with particle tracking simulations performed with PLACET, except from some deviation in the high-energy part of the spectrum. In one measurement the difference was explained from an artifact in the incoming energy spread, however this was unfortunately not measured for the other data set.

The change in horizontal emittance after deceleration was studied in the Test Beam Line. Quadrupole scans performed both before and after deceleration were compared with particle tracking simulations based on the initial parameters. An emittance estimation error of 1.7 %, originating from chromaticity because of the large beam energy spread, was found from simulations. No deviations between measurements and simulations were found apart from this, and we conclude that the change in geometrical emittance can be attributed to adiabatic undamping.

We have also studied longitudinal space charge in the CLIC drive beam decelerator. A new PIC code was developed in Octave, that is based on cylindrical coordinates in two dimensions and assumes an axisymmetric beam. When a bunch was tracked through a decelerator sector, the bunch length was only found to increase by 3.4 ppm, which is negligible even when compared to the strict bunch length tolerance of 1.1 %. When the PETS deceleration was scaled up 10 %, so that 99 % of the beam energy was extracted in the decelerator sector, the bunch lengthening was still more than an order of magnitude lower than the tolerance. However, a large part of the beam was lost in the vacuum pipe because of adiabatic undamping.

In the Test Beam Line one can still reach a higher deceleration than what has been measured until now, since the experiment has not yet reached its full potential. In particular, if the nominal beam current can be transported through the line, and if the three last PETS structures are installed in the beamline, a deceleration of more than 50 % can be achieved. The beamline is currently being equipped with an additional PETS with recirculation, which can feed a portion of the produced field back into the structure, thereby reaching an even higher output power. This will also allow the exploration of an even stronger deceleration regime.

CLIC is now a mature option for the next generation particle collider. The major feasibility issues have been resolved, and we hope this thesis has contributed to the understanding of the decelerator and its current prototype. Based on the experimental results and the simulations presented in this thesis, we consider the theoretical models used to design the CLIC decelerators as validated.

Bibliography

[1] D. J. Griffiths, *Introduction to Elementary Particles*. Wiley, second ed., 2008.

[2] "Planck information by ESA." Online at `http://sci.esa.int/planck/51551-simple-but-challenging-the-universe-according-to-planck/`.

[3] "Search for supersymmetry in events with four or more leptons in $\sqrt{s} = 8$ TeV pp collisions with the ATLAS detector," *Submitted to Phys. Rev. D*, no. CERN-PH-EP-2014-074. arXiv:1405.5086, 2014.

[4] Y. Alexahin, C. M. Ankenbrandt, D. B. Cline, A. Conway, M. A. Cummings, *et al.*, "Muon Collider Higgs Factory for Snowmass 2013," 2013.

[5] H. Wiedemann, *Particle Accelerator Physics*. Springer, third ed., 2007.

[6] A. Chao, *Physics of Collective Beam Instabilities in High Energy Accelerators*. Wiley-Interscience, 1993.

[7] T. P. Wangler, *RF Linear Accelerators*. Wiley VCH, second ed., 2008.

[8] M. G. Minty and F. Zimmermann, *Measurement and Control of Charged Particle Beams*. Springer, 2003.

[9] M. Olvegård and V. Ziemann, "Effect of large momentum spread on emittance measurements," *Nuclear Instruments and Methods in Physics Research A*, vol. 707, pp. 114–119, 2013.

[10] M. Aicheler, P. Burrows, M. Draper, T. Garvey, P. Lebrun, K. Peach, N. Phinney, H. Schmickler, D. Schulte, and N. Toge, eds., *A Multi-TeV Linear Collider Based on CLIC Technology*. CERN, 2012.

[11] E. Adli, *A Study of the Beam Pysics in the CLIC Drive Beam Decelerator*. PhD thesis, University of Oslo, Oslo, Norway, 2009.

[12] E. Adli, R. Ruber, V. Ziemann, R. Corsini, A. Dubrovskiy, and I. Syratchev, "X-band rf power production and deceleration in the two-beam test stand of the Compact Linear Collider test facility," *Physical Review Letters Special Topics – Accelerators and Beams*, vol. 14, no. 081001, 2011.

[13] P. B. Wilson, "High energy electron linacs: Application to storage rings rf systems and linear colliders." SLAC-PUB-2884 (Rev.), 1991.

[14] A. Millich and L. Thorndahl, "Loss factor Dependence on Group Velocity in Disk-Loaded Travelling-Wave Structures," Tech. Rep. CERN-OPEN-99-003. CLIC-Note-366, CERN, Geneva, Jan 1999.

[15] G. Geschonke and A. Ghigo, eds., *CTF3 Design Report.* CERN, 2002.

[16] R. Corsini, B. Dupuy, L. Rinolfi, P. Royer, and F. Tecker, "Commissioning of the CLIC Test Facility 3 preliminary phase in 2001." CERN CLIC Note 507, 2002.

[17] G. Geschonke, "Results from the CLIC Test Facility CTF3 and update on the CLIC design," in *Proceedings of the 11th biennial European Particle Accelerator Conference, EPAC'08*, pp. 2912–2916, 2008.

[18] R. Ruber, "CLIC feasibility demonstration at CTF3," in *Proceedings of the 1st International Particle Accelerator Conference, IPAC'10*, pp. 36–40, 2010.

[19] "The CLIC feasibility demonstration in CTF3," in *Proceedings of the 2nd International Particle Accelerator Conference, IPAC'11*, pp. 1042–1044, 2011.

[20] S. H. Shaker, *Longitudinal Beam Dynamics Studies at CTF3 And Pulse Compressor Controlling.* PhD thesis, Institute for studies in Theoretical Physics and Mathematics (IPM), Tehran, Iran, 2009.

[21] J. A. Riche, "Maximum energy transfer efficiency in CLIC drive beam and proposal for a method of focusing, derived from a very general discussion on focusing in linacs." CERN CLIC Note 266, 1994.

[22] F. Toral, C. Burgos, D. Carrillo, J. L. Gutierrez, I. Rodriguez, E. Rodríguez, S. Sanz, C. Vazquez, J. Calero, L. García-Tabarés, E. Adli, N. Chritin, S. Doebert, and J. A. Rodriguez, "Design, manufacturing and tests of a micrometer precision mover for CTF3 quadrupoles," in *Proceedings of the 11th biennial European Particle Accelerator Conference, EPAC'08*, pp. 1517–1519, 2008.

[23] G. Sterbini, S. Döbert, E. Marín, R. L. Lillestøl, D. Schulte, and E. Adli, "Beam-based alignment in CTF3 test beam line," in *Proceedings of the 3rd International Particle Accelerator Conference, IPAC'12*, pp. 1894–1896, 2012.

[24] J. J. García-Garrigós, A. Faus-Golfe, and J. V. Civera-Navarrete, "Design and construction of an inductive pick-up for beam position monitoring in the test beam line of the CTF3," in *Proceedings of the 11th biennial European Particle Accelerator Conference, EPAC'08*, pp. 1110–1112, 2008.

[25] J. J. García-Garrigós, "Design and construction of a beam position monitor prototype for the Test Beam Line of the CTF3," Master's thesis, Universidad Politécnica de Valéncia, 2008.

[26] J. J. García-Garrigós, *Development of the Beam Position Monitors for the Diagnostics of the Test Beam Line in the CTF3 at CERN.* PhD thesis, Universidad Politécnica de Valéncia, 2013.

[27] A. Dabrowski, M. Velasco, H. H. Braun, R. Corsini, S. Döbert, T. Lefèvre, F. Tecker, and P. Urschütz, "Non-destructive single shot bunch length measurements for the CLIC Test Facility 3," in *Proceedings of the 2007 IEEE Particle Accelerator Conference, PAC'07*, 2007.

[28] A. Dabrowski. Private communication.

[29] M. Olvegård, E. Bravin, F. Carra, N. Chritin, A. Dabrowski, A. Dallocchio, S. Döbert, T. Lefèvre, and E. Adli, "Spectrometry in the Test Beam Line at CTF3," in *Proceedings of the 1st International Particle Accelerator Conference, IPAC'10*, pp. 1113–1115, 2010.

[30] M. Olvegård, E. Adli, H. H. Braun, E. Bravin, N. Chritin, R. Corsini, A. E. Dabrowski, S. Döbert, C. Dutriat, D. Egger, T. Lefèvre, O. Mete, P. K. Skowronski, and F. Tecker, "High intensity profile monitor for time resolved spectrometry at the CLIC test facility 3," *Nuclear Instruments and Methods in Physics Research A*, vol. 683, pp. 29–39, 2012.

[31] M. Olvegård, E. Adli, W. Andreazza, B. Bolzon, E. Bravin, N. Chritin, A. Dabrowski, S. Döbert, M. Duraffourg, T. Lefèvre, R. Lillestøl, and V. Ziemann, "Beam profile monitoring at the test beam line at the Compact Linear Collider test facility," *Physical Review Special Topics – Accelerators and Beams*, vol. 16, no. 082802, 2013.

[32] M. Olvegård, B. Bolzon, E. Bravin, S. Burger, A. Dabrowski, T. Lefèvre, and C. P. Welsch, "Performance of parabolic and diffusive OTR screens at the CLIC test facility 3," in *Proceedings of the 10th European Workshop on Beam Diagnostics and Instrumentation for Particle Accelerators, DIPAC'11*, pp. 382–384, 2011.

[33] R. L. Lillestøl, "Power production experiments at the test beam line in the CLIC test facility 3," Master's thesis, Norwegian University of Science and Technology, 2010.

[34] "MAD – methodical accelerator design." Online at `http://madx.web.cern.ch/madx/`.

[35] D. Carrillo, J. L. Gutiérrez, I. Rodríguez, E. Rodríguez, S. Sanz, F. Toral, J. Calero, L. García-Tabarés, N. Chritin, S. Doebert, G. Riddone, I. Syratchev, M. Taborelli, and G. Arnau, "Engineering design of a PETS tank prototype for CTF3 test beam line," in *Proceedings of the 11th biennial European Particle Accelerator Conference, EPAC'08*, pp. 739–741, 2008.

[36] F. Toral, D. Carrillo, P. Abramian, F. Aragon, J. Calero, L. Garcia-Tabares, J. L. Gutierrez, A. Lara, E. Rodriguez, L. Sanchez, S. Doebert, and I. Syratchev, "Manufacturing and testing of a TBL PETS prototype," in *Proceedings of the 1st International Particle Accelerator Conference, IPAC'10*, pp. 3768–3770, 2010.

[37] E. Adli, A. E. Dabrowski, S. Döbert, M. Olvegård, D. Schulte, I. Syratchev, and R. L. Lillestøl, "Experimental program for the CLIC Test Facility 3 Test Beam Line," in *Proceedings of the 1st International Particle Accelerator Conference, IPAC'10*, 2010.

[38] E. Adli, S. Döbert, R. Lillestol, M. Olvegaard, I. Syratchev, D. Carrillo, F. Toral, A. Faus-Golfe, J. J. Garcia-Garrigos, Y. Kubyshin, and G. Montoro, "Commissioning status of the decelerator test beam line in CTF3," in *Proceedings of the 25th Linear Accelerator Conference, LINAC'10*, 2010.

[39] R. L. Lillestøl, S. Döbert, M. Olvegård, A. N. Rabiller, G. Sterbini, and E. Adli, "Experimental verification of the CLIC decelerator with the test beam line in the CLIC Test Facility 3," in *Proceedings of the 3rd International Particle Accelerator Conference, IPAC'12*, 2012.

[40] R. L. Lillestol, S. Doebert, M. Olvegaard, and E. Adli, "Experimental restults from the test beam line in the CLIC Test Facility 3," in *Proceedings of the 4th International Particle Accelerator Conference, IPAC'13*, 2013.

[41] B. Constance, A. Andersson, J. Barranco, R. Corsini, S. Doebert, A. Dubrovskiy, P. K. Skowroński, F. Tecker, W. Farabolini, T. Persson, R. L. Lillestol, E. Ikarios, M. Jacewicz, A. Palaia, and R. Ruber, "Experimental verifiction of the CLIC two-beam acceleration technology in CTF3," in *Proceedings of the 4th International Particle Accelerator Conference, IPAC'13*, pp. 1436–1438, 2013.

[42] R. L. Lillestøl, S. Döbert, E. Adli, and M. Olvegård, "Electron beam deceleration measurements using the decelerator test beam line in the Compact Linear Collider test facility," *Physical Review Special Topics – Accelerators and Beams*, vol. 17, no. 031003, 2014.

[43] T. Persson, P. Skowronski, and R. Corsini, "Drive beam stability studies and stabilization algorithms in CLIC Test Facility 3," *Nuclear Instruments and Methods in Physics Resarch A*, vol. 735, pp. 152–156, 2014.

[44] "The tracking code PLACET." Online at `https://savannah.cern.ch/projects/placet/`.

[45] "GNU Octave." Online at `http://www.gnu.org/software/octave/`.

[46] E. Adli. Private communication.

[47] R. L. Lillestol, S. Doebert, A. Latina, D. Schulte, E. Adli, and K. N. Sjobak, "Longitudinal space charge effects in the CLIC drive beam," in *Proceedings of the 4th International Particle Accelerator Conference, IPAC'13*, 2013.

[48] S. M. Lund, A. Friedman, and G. Bazouin, "Sheet beam model for intense space charge: Application to Debye screening and the distribution of particle oscillation frequencies in a thermal equilibrium beam," *Physical Review Special Topics – Accelerators and Beams*, vol. 14, no. 054201, 2011.

[49] A. Taflove and M. Brodwin, "Numerical solution of steady-state electromagnetic scattering problems using the time-dependent maxwell's equations," *IEEE Trans. Microwave Theory & Techniques*, vol. MTT-23, no. 623, 1975.

[50] J. P. Verboncoeur, "Particle simulation of plasmas: review and advances," *Plasma Physics and Controlled Fusion*, vol. 47, pp. A231–A260, 2005.

[51] J. P. Verboncoeur, "Symmetric spline weighting for charge and current density in particle simulation," *Journal of Computational Physics*, vol. 174, pp. 421–427, 2001.

Appendix A

Collection of publications

This appendix presents the articles that the author has contributed during the thesis work. The articles are included in reverse chronological order, and a summary is given for each of them including the title, abstract, the author's contribution and other information.

A.1 Electron beam deceleration measurements

- **Title**: Electron beam deceleration measurements using the decelerator test beam line in the Compact Linear Collider test facility
- **Abstract**: We discuss beam deceleration through a series of 12 Power Extraction and Transfer Structures, at the CLIC Test Facility 3 at CERN, as a proof-of-principle of the CLIC deceleration scheme. Up to 36 % of the kinetic energy of an electron drive beam is extracted and converted to 12 GHz RF power. We look at the average and maximum energy loss of the particles, and compare with simulations performed with the PLACET tracking code. The measured final energy is also compared to predictions based on the measured beam current and RF power in the structures. In the analysis we make use of the charge distribution form factor, taking into account the bunch length and the bunch phase. Finally, we look at the evolution of the transverse emittance with deceleration, and compare the measured emittance with simulations.
- **Where**: Physical Review Letters Special Topics – Accelerators and Beams **17**, 031003
- **When**: 24 March 2014
- **Contribution**: Reidar was the main author and wrote the entire journal article. He conducted all experiments in cooperation with S. Döbert. All the simulations and all data analysis was carried out by Reidar, with one exception – the simulations of chromaticity in quadrupole scans in the TBL. When published, the article received the *Editor's Suggestion* mark, as the only article in that issue of the journal.
- **Authors**: R. L. Lillestøl, S. Döbert, E. Adli and M. Olvegård
- **Bibliography entry**: [42]

Electron beam deceleration measurements using the decelerator test beam line in the Compact Linear Collider test facility

R. L. Lillestøl,[1,2*] S. Döbert,[1] E. Adli,[2] and M. Olvegård[3]
[1]*CERN, CH-1211 Geneva 23, Switzerland*
[2]*Department of Physics, University of Oslo, 0316 Oslo, Norway*
[3]*Department of Physics and Astronomy, Uppsala University, 75120 Uppsala, Sweden*
(Received 29 October 2013; published 24 March 2014)

We discuss beam deceleration through a series of 12 power extraction and transfer structures, at the CLIC test facility 3 at CERN, as a proof-of-principle of the CLIC deceleration scheme. Up to 36% of the kinetic energy of an electron drive beam is extracted and converted to 12 GHz rf power. We look at the average and maximum energy loss of the particles, and compare them with simulations performed with the PLACET tracking code. The measured final energy is also compared to predictions based on the measured beam current and rf power in the structures. In the analysis we make use of the charge distribution form factor, taking into account the bunch length and the bunch phase. Finally, we look at the evolution of the transverse emittance with deceleration and compare the measured emittance with simulations.

DOI: 10.1103/PhysRevSTAB.17.031003 PACS numbers: 41.75.Ht, 29.27.−a, 29.20.Ej

I. INTRODUCTION

The proposed future e^+e^- collider CLIC [1] will use a two-beam scheme, in which an electron drive beam running in decelerators parallel to the main beam acts as a power source for accelerating the main beam to the final energy of 3 TeV. This allows a very high accelerating gradient for the main beam of 100 MV/m using normal conducting technology with a high efficiency.

Energy is extracted from the drive beam using power extraction and transfer structures (PETS), which are passive, periodically loaded microwave structures with a preferred synchronous mode at $\omega_{\mathrm{rf}}/2\pi = 12$ GHz [1]. The resonating wakefield in the PETS builds up constructively from the passing bunch train, which has a 12 GHz bunch frequency. The rf power travels down the structures with a group velocity of $0.46c$, where c is the speed of light and is extracted via output couplers. Finally, waveguides guide the power to the accelerating structures of the main beam for acceleration. The drive beam loses kinetic energy from the extraction in the PETS, and at the end of the decelerators the most decelerated particles will have lost 90% of their initial energy of 2.4 GeV. Due to the field buildup of the PETS, the produced rf power has a short transient at the start of the bunch train [2]. The beam also develops a large energy spread. The beam dynamics of a decelerated beam has previously been studied in detail for relativistic klystron two-beam accelerators in [3] for a lower beam energy than the CLIC drive beam will have.

An important challenge for CLIC is to transport the heavily decelerated drive beam, with its large energy spread, through the 1 km long decelerators. The transverse beam size will increase because of adiabatic undamping from the deceleration, and at the end of the decelerators the beam will fill a large part of the aperture. It is therefore important to ensure that the transverse phase space does not increase significantly due to other effects like higher-order modes in the PETS. The structures will be equipped with higher-order mode absorbers to counteract this. There is also a strict tolerance on quadrupole magnet misalignment, and advanced beam-based alignment schemes and precise alignment techniques will be needed.

At CERN, the CLIC test facility 3 was set up to verify and demonstrate key concepts of the CLIC scheme [4]. Most of the facility consists of a drive beam complex, where an electron beam is created, bunched, accelerated, and interleaved in a delay loop and a combiner ring, similar to the future CLIC machine. One of the main experiments is the decelerator test beam line (TBL), which is a prototype decelerator where the electron beam is decelerated through a series of PETS. The energy extracted in the TBL is measured and dissipated in rf loads. The main focus of the experiment is to demonstrate low-loss transport of a heavily decelerated beam, to benchmark PETS power production with theory, and to operate a small-scale decelerator.

For reference, a simulation of the particle energies at the end of the TBL is shown in Fig. 1, performed with the PLACET tracking code [5]. The simulation assumes nominal conditions with all PETS installed, where the most decelerated particles will have lost 55% of the initial energy of 150 MeV. The figure shows the high-energy transient at the

*reidar.lunde.lillestol@cern.ch

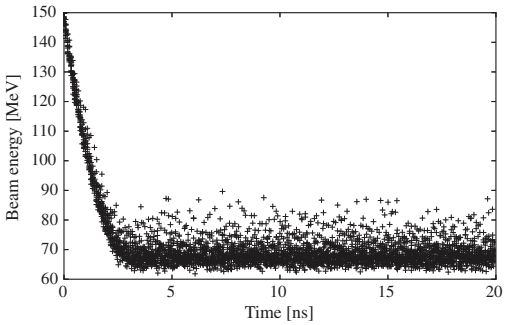

FIG. 1. Energies of simulated particles in the TBL from the PLACET tracking code. Nominal beam parameters were used in the simulation, and the plot shows the first 20 ns out of the 140 ns bunch train. At the start one can easily see the high-energy transient time that occurs due to the field buildup in the PETS.

beginning of the pulse, and a significant energy spread of 14% (FWHM) in the steady state. Particles of all energies, undergoing different levels of deceleration, must be transported to the end of the line.

In this paper we present a detailed analysis of the relation between drive beam parameters, power production, and energy loss. Some preliminary results were reported in [6]. We demonstrate that all aspects of the CLIC drive beam deceleration and rf power production are well understood. Key formulas are presented in Sec. II, and one parameter is elaborated on in Sec. III, with derivations of new equations. In Sec. IV we describe the experimental setup of the TBL. Finally we present the experimental results, focusing on deceleration results in Sec. V and the evolution of the transverse emittance in Sec. VI.

II. BEAM DECELERATION

The power P produced in a PETS at steady state is given by [2,7]

$$P = \frac{1}{4}(R'/Q)\frac{\omega_{\mathrm{rf}}}{v_g}L^2I^2F^2\{\lambda(z)\}\eta_\Omega^2, \tag{1}$$

where R'/Q is proportional to the structure impedance per meter, ω_{rf} the synchronous frequency, v_g the group velocity, L the structure length, I the beam current, η_Ω an ohmic loss factor, and $F\{\lambda(z)\}$ the charge distribution form factor. The parameters R'/Q, ω_{rf}, v_g, and η_Ω all refer to the preferred synchronous PETS mode used for power production. The charge distribution form factor will be discussed in detail in the next section.

The maximum energy loss of a steady-state particle in one PETS is equivalent to the peak voltage $\hat{V}$ seen by the particle in the structure,

$$\hat{V} = \frac{L}{2}\sqrt{\frac{(R'/Q)\omega_{\mathrm{rf}}}{v_g}P}. \tag{2}$$

Combining this with Eq. (1), the maximum energy loss can also be written

$$\hat{V} = \frac{L^2}{4}(R'/Q)\frac{\omega_{\mathrm{rf}}}{v_g}IF\{\lambda(z)\}\eta_\Omega. \tag{3}$$

We can further express the mean energy loss in one structure as

$$\langle V\rangle = \hat{V}F\{\lambda(z)\} = \frac{L^2}{4}(R'/Q)\frac{\omega_{\mathrm{rf}}}{v_g}IF^2\{\lambda(z)\}\eta_\Omega. \tag{4}$$

Using Eqs. (2)–(4), it is possible to predict the deceleration from either the form factor and the measured power, or from the form factor and the measured beam current.

It is vital to use a high average beam current in order to produce high power in accordance with Eq. (1). In CLIC, drive beam bunches are interleaved in one delay loop and two combiner rings, which together increase the bunch frequency and the average beam current by a factor of 24 while shortening the bunch train. After combination, the average beam current will be 101 A. The CTF3 has one delay loop and one combiner ring, which together can produce a maximum beam current of 28 A.

III. THE FORM FACTOR

We now turn our eyes to the charge distribution form factor $F\{\lambda(z)\}$ that appears in Eqs. (1)–(4), and derive an equation where the contributions from the bunch phase and the bunch lengths are separated. This is relevant for the CLIC scheme because of the complex bunch interleaving process which can result in systematic bunch phase errors. $F\{\lambda(z)\}$ will simply be referred to as "the form factor."

The power in a PETS depends on the wakefields from the last N_{b} bunches, where N_{b} is the number of bunches required for the field buildup in the structure that causes a transient as shown in Fig. 1. This number is given by

$$N_{\mathrm{b}} = Lf_{\mathrm{b}}\left(\frac{1}{v_g} - \frac{1}{c}\right), \tag{5}$$

where f_{b} is the bunch frequency.

At a given time we consider the longitudinal charge distribution $\lambda(z)$ of the last N_{b} bunches, and normalize it so that $\int_{-\infty}^{\infty}\lambda(z)dz = 1$. Then, the form factor is defined as the absolute value of its Fourier transform evaluated at the bunch frequency f_{b},

$$F\{\lambda(z)\} \equiv \left|\int_{-\infty}^{\infty}\lambda(z)e^{i2\pi f_{\mathrm{b}}z/c}\mathrm{d}z\right|, \tag{6}$$

and we have the constraint $0 \le F\{\lambda(z)\} \le 1$. The upper bound would apply for pointlike bunches that arrive with no deviation from the correct bunch frequency.

We write the total effective charge distribution as a sum over the charge distribution $\lambda_n(z)$ of each individual bunch, $\lambda(z) = \sum_{n=1}^{N_b} \lambda_n(z)$. The center of each of these bunches is defined as

$$z_n \equiv \frac{\int_{-\infty}^{\infty} z\lambda_n(z)\mathrm{d}z}{\int_{-\infty}^{\infty} \lambda_n(z)\mathrm{d}z}, \tag{7}$$

and we define a phase ϕ_n for each bunch as

$$\phi_n = \exp\left(\frac{i2\pi f_b z_n}{c}\right). \tag{8}$$

The form factor can then be written

$$\begin{aligned} F\{\lambda(z)\} &= \left| \int_{-\infty}^{\infty} \sum_{n=1}^{N_b} \lambda_n(z) \exp\left(\frac{i2\pi f_b z_n}{c}\right) \right. \\ &\quad \left. \times \exp\left[\frac{i2\pi f_b (z - z_n)}{c}\right] \mathrm{d}z \right| \\ &= \left| \int_{-\infty}^{\infty} \sum_{n=1}^{N_b} \lambda_n(z) e^{i\phi_n} e^{i\theta_n(z-z_n)} \mathrm{d}z \right|, \end{aligned} \tag{9}$$

where $\theta_n(z - z_n) = 2\pi f_b(z - z_n)/c$ is an interbunch phase relative to the bunch center.

By introducing a change of variables $z' = z - z_n$, we rewrite Eq. (9) as

$$\begin{aligned} F\{\lambda(z')\} &= \left| \int_{-\infty}^{\infty} \sum_{n=1}^{N_b} \lambda_n(z' + z_n) e^{i\phi_n} e^{i\theta_n(z')} \mathrm{d}z' \right| \\ &= \left| \int_{-\infty}^{\infty} \sum_{n=1}^{N_b} \lambda_0(z') e^{i\phi_n} e^{i\theta_0(z')} \mathrm{d}z' \right|, \end{aligned} \tag{10}$$

where in the last step we utilize a new function $\lambda_0(z') = \lambda_n(z' + z_n)$. Since $\lambda_n(z)$ is symmetric around z_n, the new function $\lambda_0(z')$ is symmetric around 0. If we consider equal bunch charge distributions, $\lambda_0(z')$ is not dependent on the bunch number n. In addition, the function $\theta_n(z')$ now has no dependence on n, and is renamed $\theta_0(z')$. Both $\lambda_0(z')$ and $\theta_0(z')$ can therefore be moved out of the summation. The bunch phase ϕ_n has no z' dependence, and can be taken out of the integral. Thus, we can separate Eq. (10) into

$$F\{\lambda(z')\} = \left| \left(\sum_{n=1}^{N_b} e^{i\phi_n} \right) \int_{-\infty}^{\infty} \lambda_0(z') e^{i\theta_0(z')} \mathrm{d}z' \right|. \tag{11}$$

We also assume that the charge distribution $\lambda_0(z')$ is an even function around 0 (a symmetric bunch) that is strictly decreasing when $|z'|$ moves away from zero,

$$\frac{\mathrm{d}}{\mathrm{d}z'} \lambda_0(z') < 0, \qquad z' > 0, \tag{12}$$

$$\frac{\mathrm{d}}{\mathrm{d}z'} \lambda_0(z') > 0, \qquad z' < 0. \tag{13}$$

If we also only consider relatively short bunches, i.e., that the charge distribution follows the criterion

$$\int_0^{c/4f_b} \lambda_0(z')\mathrm{d}z' \ge \int_{c/4f_b}^{3c/4f_b} \lambda_0(z')\mathrm{d}z', \tag{14}$$

the integral in Eq. (11) will be real and positive, and we can write

$$F\{\lambda(z')\} = \left| \sum_{n=1}^{N_b} e^{i\phi_n} \right| \times \int_{-\infty}^{\infty} \lambda_0(z') e^{i\theta_0(z')} \mathrm{d}z'. \tag{15}$$

The sum and the integral can be normalized separately by multiplying Eq. (15) with N_b/N_b,

$$\begin{aligned} F\{\lambda(z')\} &= \frac{1}{N_b} \left| \sum_{n=1}^{N_b} e^{i\phi_n} \right| N_b \int_{-\infty}^{\infty} \lambda_0(z') e^{i\theta_0(z')} \mathrm{d}z' \\ &\equiv \Phi(\{\phi_n\}) F_b\{\lambda_0(z')\}. \end{aligned} \tag{16}$$

Here we have introduced the functional

$$F_b\{\lambda_0(z')\} \equiv N_b \int_{-\infty}^{\infty} \lambda_0(z') e^{i\theta_0(z')} \mathrm{d}z' \tag{17}$$

which defines the single-bunch form factor, and the function

$$\Phi(\{\phi_n\}) \equiv \frac{1}{N_b} \left| \sum_{n=1}^{N_b} e^{i\phi_n} \right| \tag{18}$$

which defines the multibunch form factor. Because of normalization we have the following bounds,

$$0 \le F_b\{\lambda_0(z')\} \le 1, \tag{19}$$

$$0 \le \Phi(\{\phi_n\}) \le 1. \tag{20}$$

According to Eq. (18), the absolute bunch phase at a given time has no relevance for the absolute PETS power production, which only depends on the dynamic phase change over a time equal to the field buildup time. When the last N_b bunches have had the same bunch phase, the multibunch form factor will evaluate to 1. Any phase change will cause a form factor reduction, and consequently a lower power production and energy extraction.

For Gaussian bunch distributions we can further simplify the single-bunch form factor. Based on streak camera measurements in the TBL, an assumption of Gaussianity

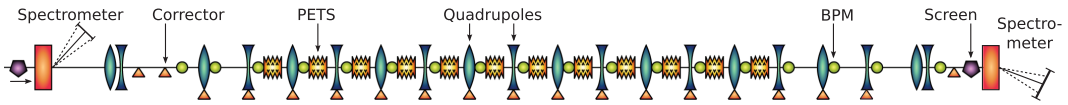

FIG. 2. The current TBL lattice. Quadrupole magnets are shown as blue lenses, dipole magnets as orange rectangles, corrector devices as orange triangles, BPMs as green circles, OTR screens as purple pentagons, and PETS as brown corrugated structures.

in the longitudinal distribution is reasonable. Consider a normalized Gaussian distribution around zero,

$$\lambda_0(z') = \frac{1}{N_b\sqrt{2\pi}\sigma_z}\exp\left(-\frac{z'^2}{2\sigma_z^2}\right). \tag{21}$$

From numerical calculations we find that for the CLIC bunch frequency the condition in Eq. (14) is satisfied for $\sigma_z \leq 9.9$ mm. The single-bunch form factor in Eq. (17), by properties of the Fourier transform of a Gaussian, evaluates to

$$F_b\{\lambda_0(z')\} = F_b(\sigma_z) = \exp\left(-\frac{2\pi^2\sigma_z^2 f_b^2}{c^2}\right). \tag{22}$$

From Eq. (22) we see the importance of having short bunches in the drive beam, to maximize the power production and energy extraction from Eqs. (1)–(4). In CLIC and in nominal CTF3 operation, the bunches are $\sigma_z = 1$ mm long.

IV. EXPERIMENTAL SETUP

In the following, we will describe the experimental equipment that make up the TBL. Similar to the CLIC decelerators, the TBL optics mainly consists of a FODO (focusing magnet, drift space, defocusing magnet, drift space) lattice. This was chosen to provide tight focusing in conditions of strong transverse wakes and because of the need for a large energy acceptance. The quadrupole focusing is tapered to provide constant focusing for the most decelerated particles, as proposed in [8]. The high-energy particles in the transient are then contained in the envelope of the low-energy particles. Normal operation uses a 90° phase advance per cell. The TBL lattice at the time of writing is shown in Fig. 2, and a selection of beam, lattice, and structure parameters is given in Table I.

Each quadrupole magnet in the FODO lattice is mounted on a mechanical mover, which can move the magnet horizontally and vertically with a precision of 5 μm. The movers were developed by CIEMAT, Madrid [9], and allow efficient beam steering and the use of beam-based alignment routines. The lattice also includes three conventional dipole corrector magnets.

TABLE I. Beam, lattice, and PETS structure parameters. Nominal parameters are given for both the TBL and one CLIC decelerator, in addition to currently achieved numbers for the TBL.

Symbol	Parameters	Current TBL	Nominal TBL	CLIC design
–	Total length of lattice [m]	40	40	≤ 1053
E_0	Initial energy [MeV]	120–125	150	2,370
$E_{\min}$	Minimum final energy [MeV]	77–118	67	240
η_{extr}	Energy extraction, $(E_0 - E_{\min})/E_0$ [%]	6–36	55	90
σ_z	Bunch length, rms [mm]	1.0–2.5	1.0	1.0
–	Bunch charge [nC]	2.3	2.3	8.4
f_b	Bunch frequency [GHz]	1.499–11.994	11.994	11.994
–	Bunch train length [ns]	140–1120	140	244
I	Beam current [A]	3.5–22	28	101
$\varepsilon_{N_{x,y}}$	Initial norm. transverse emittances, rms [μm]	150–500	150	150
–	Number of PETS [–]	12	16	1492
–	Vacuum chamber inner radius [mm]	11.5	11.5	11.5
–	Repetition rate [Hz]	0.83–1.67	0.83–5.0	50
$\omega_{\text{rf}}/2\pi$	Synch. mode frequency [GHz]	11.994	11.994	11.994
R'/Q	Synch. mode impedance per meter [linac-Ω/m]	2,222	2,222	2,290
v_g	Synch. mode group velocity [c]	0.46	0.46	0.45
η_Ω	Synch. mode ohmic loss factor [–]	0.985	0.985	0.996
L	PETS length [m]	0.8	0.8	0.235
P	Power production per PETS [MW]	2–70	135	134
$\hat{V}$	Max. deceleration per PETS [MeV]	0.6–3.3	5.2	1.45
N_b	Bunches required for field build-up [–]	37	37	10

The TBL has space between the quadrupoles for 16 PETS, of which 12 are currently installed. Three structures were constructed by CIEMAT [10,11] and the other nine were constructed at CERN. Since the nominal CTF3 drive beam current is around 1/4 of the CLIC drive beam current, the PETS are four times longer for compensation, and can produce roughly the same amount of rf power in accordance with Eq. (1). Each PETS is placed in a vacuum tank with water cooling, to avoid frequency shifts due to thermal deformation. One of the installed PETS tanks is shown in Fig. 3. All of the structures are equipped with higher-order mode absorbers made of silicon carbide, to damp any deflecting higher-order modes which can induce beam loss.

At the downstream side of each PETS, an output coupler guides the field into two waveguide arms. One arm from each structure is connected to readout electronics through a directional coupler and an attenuation chain for measuring the produced power. Most of the power is not used for measurements via the directional coupler but is dissipated in water-cooled loads. In case some power would be reflected by the load, this can also be measured. Since the power amplitude is too high to be measured directly, the power is attenuated by approximately 90 dB before entering the electronics. This includes the directional coupler, attenuators, and cables. The attenuation chain must be calibrated piecewise, and this can lead to a large systematic error for the power amplitude. We estimate a power calibration error of up to 20%, which corresponds to an attenuation error of 0.8 dB over the whole measurement chain. Note that this describes a constant attenuation error of the whole signal, such that the signal shape should be unaffected. The power amplitude from each PETS is measured with Schottky diodes. In addition, one PETS is measured with IQ (in-phase/quadrature-phase) demodulators that also give information about the rf phase.

The beam position monitors (BPMs) in the TBL are a scaled and revised version of those in the CTF3 drive beam linac [12]. They were designed and manufactured by IFIC Valencia and UPC Barcelona, and are inductive pickup wall current monitors that are also used for intensity diagnostics. The major error contribution in the intensity measurements is the resolution of the 192 MHz digitizers [13], which is constant and therefore relatively larger at lower beam currents.

The beam current entering the TBL can range from 3.5 A to 28 A. This is because the CTF3 contains one delay loop that can interleave bunches by a factor of two, and one combiner ring that can interleave bunches by a factor of four. When both of these are used, the initial bunch frequency of 1.5 GHz and the average intensity of 3.5 A are multiplied by a factor of 8. During operation it is also possible to bypass either or both of these, which gives access to the large intensity span. This allows TBL operation with different amounts of deceleration, since the beam current affects the deceleration linearly according to Eqs. (2)–(4).

In order to measure the energy of the decelerated beam, there is one spectrometer at the beginning and another at the end of the TBL. The spectrometer at the end of the line is a segmented dump that consists of 32 tungsten segments, which allows for time-resolved, single-shot spectrometry with a resolution of 1% [14–16]. The spectrometer at the beginning of the line is of a simpler type and is equipped with a single slit, which provides time-resolved spectrometry with a scan.

Optical transition radiation (OTR) screens are used for monitoring the transverse beam distribution, and are used in emittance measurements. One of these screens is placed just before the dipole magnet at the entry to the experiment, while another is placed after the decelerator FODO lattice, as shown in Fig. 2. These screens are inserted into the vacuum pipe when measurements are needed and are imaged by charge-coupled device (CCD) cameras. Finally, a streak camera imaging the OTR screen at the beginning of the line can provide information about the bunch length and bunch spacing. The performance of the OTR screens is documented in [14,17].

Compared to the future CLIC decelerators, the TBL experiment starts with a lower incoming energy and usually a higher emittance in both the longitudinal and the transverse planes. In addition, the TBL suffers from beam jitter originating from the CTF3, even though this is under improvement [18]. Thus, the TBL experiment is considered more challenging than the CLIC case.

Some of the nominal beam parameters in Table I have not yet been reached, mainly because of upstream beam losses originating from the combination process.

V. DECELERATION RESULTS

We focus primarily on measurements where the CTF3 was set up for a factor of 4 bunch combination, by utilizing the CTF3 combiner ring and bypassing the delay loop. This gave an average beam current of 13.5 A during 280 ns long bunch trains. The measured incoming energy was $E_0 = 123.5$ MeV with an energy spread of 3.0% FWHM. The mean energy was lower than the nominal value in Table I because of two klystrons in the CTF3 linac that are not in operation. A data set collected over 60 consecutive pulses was used for the analysis.

The transmission along a decelerator line affects the possible deceleration and energy extraction because of the change in effective beam current. The transmission in the TBL is normally above 90%. The incoming beam current for the data set was 14.0 A and the outgoing was 13.2 A, resulting in a 94% transmission. The systematic error on the intensity measurement, dependent on the intensity level, was estimated to be 2%. Within this error the beam losses were spread fairly evenly over the beamline.

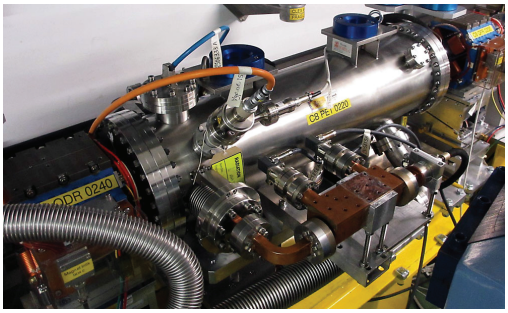

FIG. 3. One of the installed PETS tanks, which keeps the structure in a vacuum. In the front, one can see a waveguide arm, where the rf power is coupled out, measured, and dissipated in a load.

The normalized horizontal emittance was measured to 330 μm instead of the nominal 150 μm. This blowup of the transverse phase space is believed to originate from a horizontal mismatch of the bunch combination, since a few distinct beam spots were visible on the OTR screens. By using the relation $\sigma_{x,y} = \sqrt{\varepsilon_{x,y}\beta_{x,y}}$ that relates the transverse beam size to the emittance and the beta function, the maximum $3\sigma_x$ beam size was 8.3 mm (the average size was 5.8 mm). Comparing this with the aperture of 11.5 mm, and taking into account the orbit which had an rms offset of 1.3 mm, we can expect that some scraping occurred which could account for the 6% beam loss. In addition, in the case of a nonperfect bunch combination the different beamlets may have had slightly different trajectories that were not shown by the BPM signal averages.

Figure 4 compares the signal from one PETS and the closest BPM, taken from the middle of the beamline. The beam current was almost constant along the pulse, with a rise-time dominated by the bandwidth of the electronics. The PETS rf power has a different and rounder shape. Since the only free parameter for the power production other than the beam current is the form factor,[1] we infer that there was a change of the bunch phase and/or the bunch length over the pulse, originating upstream.

Bunch length measurements were unavailable on the day of measurement, but we analyze the RF phase from the first PETS and calculate a multibunch form factor. The phase measurement from the combined beam cannot be used directly because there can be large bunch-to-bunch phase jumps from the combination, and the sampling frequency of the IQ demodulators is lower than the bunch frequency, which violates the Nyquist-Shannon sampling theorem.

[1]There is also a possibility of pulse shortening due to rf breakdowns in the PETS, however the breakdown rate is negligible at the measured power level, which is 1/4 of the nominal value.

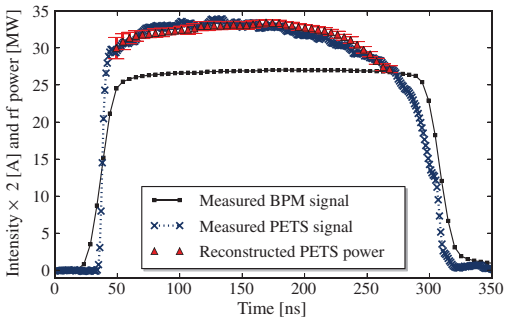

FIG. 4. Measured beam current and RF power for one BPM and one PETS. The beam current has been multiplied by a factor of 2. The shape of the produced power pulse is somewhat different from the beam current pulse, which can be explained by a change in the form factor over the pulse. A reconstruction from the BPM signal and the multibunch form factor based on Eqs. (1), (16), (18), and the signal in Fig. 5 is shown with red triangles.

Instead we look at the phase from an uncombined beam (which should be smoother from bunch to bunch), measured for the same run at a different time. The 12 GHz phase as measured in the PETS is shown in Fig. 5. To construct a multibunch form factor, the raw 12 GHz phase measurement was first converted to $f_b = 3$ GHz phase, and interpolated to the same sample rate as the bunch frequency. The samples were then reshuffled to simulate a factor of 4 bunch combination in the combiner ring, and the phase was converted back to 12 GHz. Finally, a multibunch form factor was constructed where each sample was based on N_b samples from the calculated phase and Eq. (18). The resulting combined multibunch form factor was then resampled for use together with the BPM or the PETS signal. In Fig. 4 we show a reconstructed power signal based on the beam current squared and the multibunch form

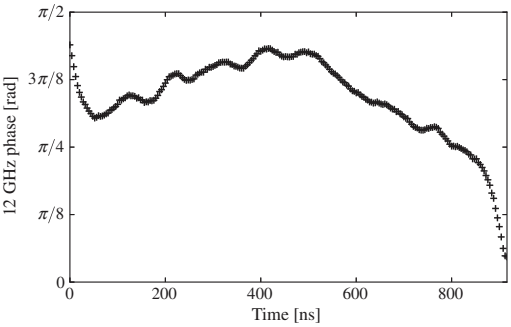

FIG. 5. 12 GHz phase measured in a PETS for an uncombined beam, which itself has a 3 GHz bunch structure and a longer bunch train than the combined beam.

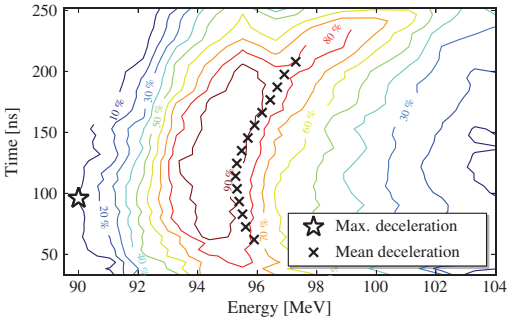

FIG. 6. Measured energy spectrum along the pulse at the end of the TBL for a beam current of 13.5 A. The contour lines show 10% increments of the maximum value of the signal, and the energy changes slightly along the pulse. The star shows the point with the most decelerated particles, while the crosses show the mean energies.

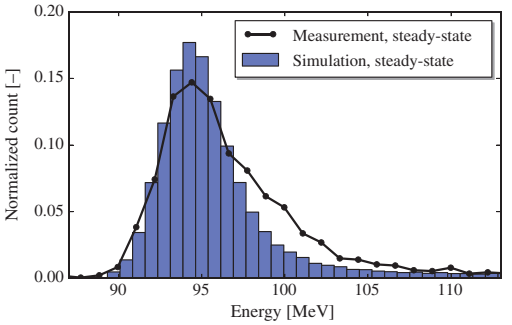

FIG. 7. The measured energy spectrum at the time instant with the most decelerated particles in Fig. 6. In addition, we show a simulated steady-state energy profile from PLACET for a form factor of $F\{\lambda(z)\} = 0.95$.

factor squared with Eq. (1). We see that the multibunch form factor to a large extent explains the different shape of the power signal. It is important to keep in mind that the significant phase change over the pulse is an artifact from the CTF3 machine, which is not built to have the same stability as CLIC.

The measured energy spectrum at the end of the TBL is shown in Fig. 6. The ordinate shows the time along the pulse, and we see that the energy changes slightly. The shape is similar to the PETS power in Fig. 4, as expected from the change in form factor. The contour lines indicate 10% increments of the signal compared to its maximum value. For finding the energy of the most decelerated particles, we define a threshold of 10% of the maximum signal. Close to the start of the pulse, this occurs at an energy of $E_{\mathrm{min}} = 90.0$ MeV. Expressing the total energy extraction as $\eta_{\mathrm{extr}} = (E_0 - E_{\mathrm{min}})/E_0$, we arrive at a maximum deceleration of $\eta_{\mathrm{extr}} = 27\%$.

Simulations of the TBL are regularly performed with the tracking code PLACET for comparing measurements with theory. PLACET simulates both single-bunch and multibunch wakefields and therefore provides a precise model of the beam energy spread. In Fig. 7, simulation results are shown where we used the measured input parameters taken together with the analyzed data set (i.e., an incoming energy of 123.5 MeV, 13.5 A beam current, 3.0% energy spread, and transverse parameters). In the same figure we have also plotted the measured energy profile at the time instant coinciding with the maximum deceleration, indicated by the star in Fig. 6. The bunch length had to be estimated in the simulation, because a streak camera measurement was unavailable during the run. For a form factor of $F\{\lambda(z)\} = 0.95$ in the simulation, we achieve a good agreement between simulation and measurement. Since the calculated multibunch form factor at this time instant was $\Phi(\{\phi_n\}) = 0.98$, by assuming Gaussian bunches we infer from Eq. (16) that the single-bunch form factor must have been $F_{\mathrm{b}}(\sigma_z) = 0.97$, corresponding to bunch lengths of $\sigma_z = 1.0$ mm. In Fig. 7 the measurement has a slightly different shape than the simulation because of an artifact in the incoming energy distribution that propagated down the beamline and that could not be reproduced in simulations. Note that the measured energy spread can be slightly overestimated due to beam scattering in the target and exit window close to the spectrometer [14], but according to simulations this overestimation is less than 1% in our case.

We next correlate the measured deceleration with that predicted from theory, and focus on the average deceleration indicated by crosses in Fig. 6. This is done for both the measured beam current and the PETS rf power, using Eqs. (2)–(4). The predicted deceleration from all individual BPM or PETS signals are added together and subtracted from the incoming energy. Our procedure for fitting the two predictions with the spectrometer measurement follows. (i) Fit the predicted deceleration from the beam current to the spectrometer measurement using Eq. (4) because the only free parameter that relates them is the form factor. The calculated multibunch form factor used for Fig. 4 is used, and a constant single-bunch form factor is chosen as an empirically derived scaling factor. Both form factor contributions are applied with Eq. (16). (ii) Fit the predicted deceleration from the PETS power with Eqs. (2) and (4) to the other two curves because this has a large scaling uncertainty from calibration errors, as described earlier. The same form factors $\Phi(\{\phi_n\})$ and $F_{\mathrm{b}}\{\lambda_0(z')\}$ are used, and a global scaling of the power amplitudes is used to estimate calibration errors. The scaling is applied before the square root in Eq. (2) is applied.

With this procedure, we arrive at a single-bunch form factor of $F_{\mathrm{b}}\{\lambda_0(z')\} = 0.96$. The rf power amplitudes need to be increased by 5%, and this is well within the expected

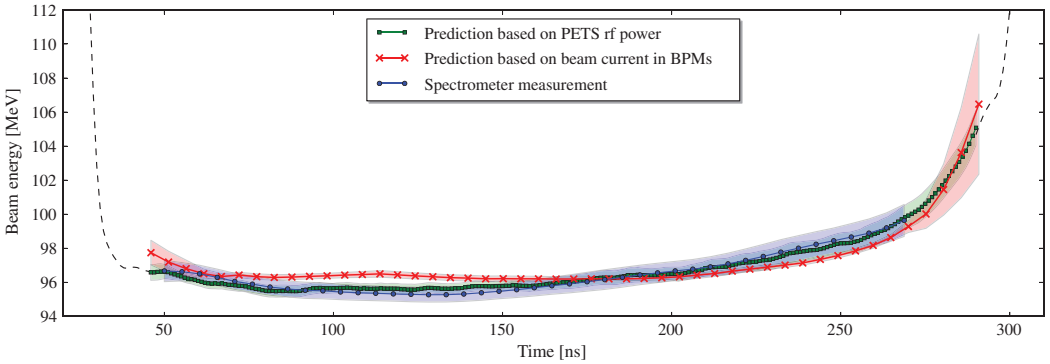

FIG. 8. Comparison between measured mean deceleration and deceleration predicted from measured beam current and PETS rf power. The curves with markers represent the average values over the data series, while the corresponding colored bands show the standard deviations. The predictions are only shown where the multibunch form factor could be calculated. Outside of this, we show the remaining signal based on the PETS rf power for reference, as a black stapled line.

uncertainty of the rf calibration. The results are shown in Fig. 8, which shows the average signals over the data series along with their standard deviations. Reliable phase information was only available in the steady-state part of the pulse, and this limits the area where the multibunch form factor can be applied. For reference we have also plotted the remaining prediction from the PETS power by using the $\Phi(\{\phi_n\})$ end-range values as guidelines for the pulse edges. The prediction based on the beam current has some small deviations from the other curves, and this can possibly be attributed to a small change in the bunch length, since our analysis uses a constant single-bunch form factor and the BPM signals are the only measurements that are not directly affected by the form factor. Note that the estimated single-bunch form factor $F_b\{\lambda_0(z')\} = 0.96$ is lower than the value obtained from the analysis in Fig. 7. This is because the latter describes a local form factor at close to the 100 ns mark in Figs. 6 and 8, where the bunch length may have been slightly shorter than the average value. Note also that the 6% beam loss mentioned earlier not only affects the BPM signals, but also the possible deceleration and the PETS rf power, such that it should not cause any discrepancy between the three signals.

As described earlier the CTF3 machine can be set up for different bunch combination schemes, and we can study how this affects the deceleration. Using the combiner ring only, the machine was set up for bunch combination with factors of 2, 3, and 4, and in addition we used the uncombined beam. This resulted in beam currents ranging from 3.5 to 13.5 A delivered to the TBL. At each setting 60 pulses were recorded, including the already analyzed data set. The bunch combination of a factor of 3 was set up twice

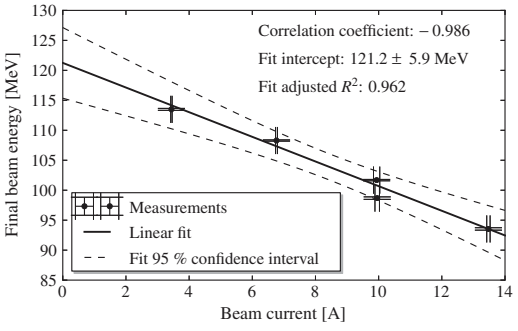

FIG. 9. Measured final energy at different beam currents and levels of deceleration. The intercept derived from a linear fit estimates what the final energy would be without deceleration.

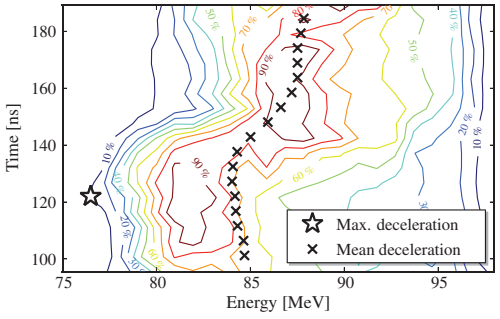

FIG. 10. Measured energy spectrum along the pulse at the end of the TBL, for 21.4 A beam current. The contour lines show 10% increments of the maximum value of the signal, and there is a step in the measured energy because of a change in the form factor. The star shows the point with the most decelerated particles, while the crosses show the mean energies.

due to instabilities during the first try. The resulting mean energies measured at the end of the TBL are shown in Fig. 9. The correlation coefficient between beam current and energy is −0.986. A linear fit was performed on the data, where the intercept was 121.2 MeV. This can be compared to the measured incoming energy of $E_0 =$ 123.5 MeV because it estimates the final energy without deceleration, something that is not possible to measure in practice. However, the intercept has a large uncertainty because the fit is extrapolated outside the measurement range. This is illustrated by the 95% confidence interval of the fit, which is shown with stapled lines in Fig. 9.

The maximum deceleration measured in the TBL was obtained during another run with an average beam current of 21.4 A and an incoming energy of 120 MeV, and amounts to 36%. Both the delay loop and the combiner ring were utilized, and the energy spectrum at the end of the line is shown in Fig. 10.

VI. TRANSVERSE EMITTANCE

For CLIC, it is vital to know that the drive beam can be transported through the 1 km decelerators, even with heavy deceleration and a large energy spread. Deceleration will cause the transverse beam size to increase significantly from adiabatic undamping, since the energy is reduced by 90%.

In the TBL case, for a perfect machine at nominal conditions, the $3\sigma_{x,y}$ beam size will grow to $2/3$ of the aperture [2] and the TBL is therefore a good test bench for the future machine. An important part of the experiment is therefore to study the evolution of the transverse emittance with deceleration.

In the TBL the transverse emittance is measured using quadrupole scans, in which the strength of one quadrupole magnet in a doublet is varied and the beam size is measured on a downstream OTR screen. A parabola is fitted to the resulting beam waist, and this gives information about the transverse emittances and the Twiss parameters. Instead of comparing single numbers for the emittance before and after deceleration, we have chosen another method that should be more meaningful. First, a number of quadrupole scans are performed at the beginning of the line, and numbers are averaged to find estimates of the emittances and Twiss parameters. The estimations are then used as input to a simulation code, in our case PLACET. A quadrupole scan is simulated at the end of the line, by varying the quadrupole strength of one magnet in the doublet in the simulation code. For the beam size we use the rms of the transverse particle distribution. Finally, a number of quadrupole scans are performed at the end of the line, and numbers are again averaged to find estimates that can be compared with simulations. If the normalized transverse emittances remain constant through the line, the beam waist should be the same in measurements and simulations at the end, and any deviations can be explained from the emittance or the Twiss parameters.

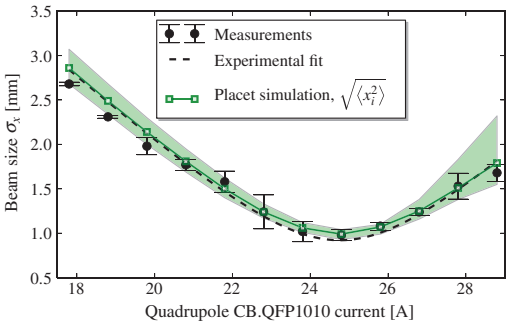

FIG. 11. Measured and simulated horizontal quadrupole scan at the end of the TBL. The measurement is an average of four quadrupole scans, and a parabola was fitted to the data. The curve for the simulations has a green band representing the uncertainty in the Twiss parameters and emittance measured at the beginning of the beamline.

For technical reasons we have only been able to perform the experiment for the horizontal emittance, and for this we carried out three scans at the beginning of the line and four at the end. The measurements were performed during the same run as most of the results in Sec. V, with 13.5 A beam current and 27% deceleration. The average beam size measurements at the end of the line are shown with error bars in Fig. 11, and a parabolic fit to the data is shown with a black dashed curve.

Beam sizes obtained from simulations with PLACET are shown with a green line with squares, and this line is very close to the experimental fit. This is a strong indication that the normalized emittance was constant at 330 μm through the line. At the beginning of the line there was a certain spread in the measured parameters from the quadrupole scan, because of uncertainty in the individual beam size measurements and small differences between the three scans. We therefore also ran a scan of simulations with different parameters based on the error bars at the beginning of the line. The resulting spread in the simulated beam size at the end is shown with a light green band in Fig. 11.

For a beam with a large energy spread such as a drive beam, chromaticity affects the beam size measured during quadrupole scans as described in [19]. In the TBL with nominal conditions, chromaticity contributes a 20% error to the measured emittance [14], although this error can easily be corrected [19]. For the conditions here with less deceleration and consequently a lower final energy spread, the emittance error is significantly smaller and was estimated to 1.7%. Both measurement errors given here were found with a numerical method that did not use the thin-lens simplification from [19]. However, an assumption was made in the analysis that the beam arrives at the scanning

quadrupoles with no correlation between momentum and transverse beam position. In the PLACET simulations, chromatic effects are fully taken into account.

When including errors we see an excellent agreement between measurements and simulations, which means that the change in geometrical emittance can be attributed to adiabatic undamping alone.

VII. CONCLUSIONS

We have studied beam deceleration through a line of 12 PETS structures. At an average beam current of 13.5 A, the most decelerated particles experienced 27% deceleration. The measurements agreed well with simulations when a form factor of $F\{\lambda(z)\} = 0.95$ was used in the simulation code. We also correlated the spectrometer measurements with predicted deceleration based on the beam current and the power production in PETS. A multibunch form factor was calculated based on the PETS rf phase, and when this was used together with an estimated value of the single-bunch form factor we saw a good agreement, within the expected errors of the measurements. The maximum deceleration measured in the TBL at the time of writing amounts to 36%.

We also investigated the evolution of the horizontal emittance with deceleration. Quadrupole scans performed before and after deceleration were compared with particle tracking simulations, and there was an excellent agreement between measurements and simulations.

The deceleration experiments with the test beam line in the CTF3 are meant to validate the design of the CLIC decelerators. The presented results show that all relevant aspects of the beam deceleration and power production have been measured and agree well with theoretical predictions. The highest possible beam current and deceleration in the CTF3 have not been achieved, yet we consider the theoretical models used to design the CLIC decelerators as validated.

ACKNOWLEDGMENTS

We want to acknowledge the CTF3 operations team—F. Tecker, P. Skowronski, R. Corsini, T. Persson, B. Constance, D. Gamba, and J. Quirante—for setting up quality beams, aiding the TBL experiment, and making the most out of the machine. Furthermore, we want to thank our Spanish collaborators in CIEMAT, IFIC, and UPC for the design and construction of important experimental equipment. Finally, we acknowledge K. Sjøbæk, G. Sterbini, I. Syratchev, and A. Bell for fruitful discussions.

[1] M. Aicheler, P. Burrows, M. Draper, T. Garvey, P. Lebrun, K. Peach, N. Phinney, H. Schmickler, D. Schulte, and N. Toge, *A Multi-TeV Linear Collider Based on CLIC Technology: CLIC Conceptual Design Report* (CERN, Geneva, 2012).

[2] E. Adli, Ph.D. thesis, Oslo University, 2009 [http://cds.cern.ch/record/1239173].

[3] S. M. Lidia, in Phys. Rev. ST Accel. Beams **4**, 041001 (2001).

[4] G. Geschonke *et al.* (The CLIC Study Team), CTF3 Design Report No. CERN/PS-2002-008 (RF), 2002 [http://cds.cern.ch/record/559331].

[5] The PLACET tracking code, online at https://savannah.cern.ch/projects/placet/.

[6] R. L. Lillestol, S. Doebert, M. Olvegaard and E. Adli, in *Proceedings of the 4th International Particle Accelerator Conference, IPAC-2013, Shanghai, China, 2013* (JACoW, Shanghai, China, 2013).

[7] E. Adli, R. Ruber, V. Ziemann, R. Corsini, A. Dubrovskiy and I. Syratchev, Phys. Rev. ST Accel. Beams **14**, 081001 (2011).

[8] J. A. Riche, CERN Report No. CLIC-Note-266, 1994 [http://cds.cern.ch/record/275691].

[9] F. Toral *et al.*, in *11th Proceedings of the European Particle Accelerator Conference, Genoa, 2008* (EPS-AG, Genoa, Italy, 2008).

[10] D. Carrillo *et al.*, in *11th Proceedings of the European Particle Accelerator Conference, Genoa, 2008* (EPS-AG, Genoa, Italy, 2008).

[11] F. Toral *et al.*, in *Proceedings of the International Particle Accelerator Conference, Kyoto, Japan* (ICR, Kyoto, 2010).

[12] J. J. García Garrigós, M.Sc. thesis, Universidad Politecnica de Valencia, 2008 [http://cds.cern.ch/record/1164156].

[13] J. J. García Garrigós, Ph.D. thesis, Universidad Politécnica de Valéncia, 2013 [http://riunet.upv.es/handle/10251/34327].

[14] M. Olvegård *et al.*, Phys. Rev. ST Accel. Beams **16**, 082802 (2013).

[15] M. Olvegård *et al.*, Nucl. Instrum. Methods Phys. Res., Sect. A **683**, 29 (2012).

[16] M. Olvegård *et al.*, in *Proceedings of the International Particle Accelerator Conference, Kyoto, Japan* (ICR, Kyoto, 2010).

[17] M. Olvegård, B. Bolzon, E. Bravin, S. Burger, A. Dabrowski, T. Lefèvre, and C. P. Welsch, in *Proceedings of the 10th European Workshop on Beam Diagnostics and Instrumentation for Particle Accelerators, Hamburg, Germany, 2011* (DESY, Hamburg, 2011).

[18] T. Persson, P. Skowronski, and R. Corsini, Nucl. Instrum. Methods Phys. Res., Sect. A **735**, 152 (2014).

[19] M. Olvegård and V. Ziemann, Nucl. Instrum. Methods Phys. Res., Sect. A **707**, 114 (2013).

A.2 Experimental results from the TBL

- **Title**: Experimental Results from the Test Beam Line in the CLIC Test Facility 3
- **Abstract**: In the CLIC two-beam scheme, the main beam is accelerated by rf power provided by energy extraction from a secondary drive beam. This energy is extracted in decelerators, and the first prototype decelerator is the Test Beam Line in the CLIC Test Facility 3. The line is currently equipped with 12 Power Extraction and Transfer Structures (PETS), which allows for extracting up to 40 % of the beam energy. We correlate the measured deceleration with predictions from the beam current and the rf power produced in the PETS. We also discuss recent bunch length measurements and how it influences the deceleration. Finally we look at the evolution of the transverse emittance.
- **Where**: The 4$^{\text{th}}$ International Particle Accelerator Conference, IPAC'13, Shanghai, China
- **When**: May 2013
- **Contribution**: Reidar was the main author, and wrote the entire article. The experiments were carried out together with S. Doebert, and Reidar did all the simulations and all the data analysis. He presented the article with a poster at the IPAC conference in Shanghai.
- **Authors**: R. L. Lillestol, S. Doebert, M. Olvegaard and E. Adli
- **Bibliography entry**: [40]

EXPERIMENTAL RESULTS FROM THE TEST BEAM LINE IN THE CLIC TEST FACILITY 3

R.L. Lillestol*, S. Doebert and M. Olvegaard, CERN, Geneva, Switzerland,
E. Adli, University of Oslo, Norway

Abstract

In the CLIC two-beam scheme, the main beam is accelerated by rf power provided by energy extraction from a secondary drive beam. This energy is extracted in decelerators, and the first prototype decelerator is the Test Beam Line in the CLIC Test Facility 3. The line is currently equipped with 12 Power Extraction and Transfer Structures (PETS), which allows for extracting up to 40 % of the beam energy. We correlate the measured deceleration with predictions from the beam current and the rf power produced in the PETS. We also discuss recent bunch length measurements and how it influences the deceleration. Finally we look at the evolution of the transverse emittance.

INTRODUCTION

In the future proposed Compact Linear Collider (CLIC), two low-energy electron drive beams are used as power sources to accelerate the two main beams before collision. The rf fields used for acceleration are extracted from the drive beams using 24 decelerators, each of which comprise a FODO lattice with a large number of Power Extraction and Transfer Structures (PETS), and which extracts 90 % of the drive beam energy. The PETS are constant impedance, passive microwave devices with a fundamental mode at 12 GHz.

In the CLIC Test Facility 3 (CTF3) at CERN, the Test Beam Line (TBL) is built as a prototype decelerator. Two of the main purposes of TBL are to demonstrate stable beam transport after significant deceleration and to study the consistency with theoretical models, and these topics will be addressed in this paper.

EXPERIMENTAL SETUP

The TBL has a similar lattice as the CLIC decelerators, and consists of 8 FODO cells with space for up to 16 Power Extraction and Transfer Structures (PETS). Figure 1 shows the current lattice. Currently 12 PETS are installed in the line. Since TBL has a 4 times lower beam current than the CLIC drive beam, the PETS are 4 times longer to compensate, and produce roughly the same amount of power. The 12 GHz rf power produced by the PETS is coupled out and measured with Schottky diodes. One PETS is measured with IQ demodulators, which also provides information about the rf phase. Since the power is attenuated by around 90 dB before entering the electronics, and the attenuation is measured piecewise [2], the accuracy of the measured amplitude is estimated to be around 10 %.

* reidar.lunde.lillestol@cern.ch

The quadrupoles in the FODO lattice are placed on moving tables made by CIEMAT [3], which allow micrometer positioning. The quadrupole focusing is tapered along the line to provide a constant phase advance for the most decelerated particles, normally 90°.

The BPMs are high precision inductive wall current monitors designed and constructed by IFIC Valencia and UPC Barcelona [4], and have a resolution of 5 μm. The beam current can vary between 3.5 and 28 A, because of different bunch combination schemes using the delay loop and combiner ring in CTF3. This affects the TBL deceleration linearly and the PETS power production quadratically.

At the end of TBL a segmented dump spectrometer [5] provides time-resolved energy measurements with an accuracy of a few percent. The start of the line is equipped with a more simple spectrometer with a single slit. The other diagnostic devices are OTR screens, and a streak camera that images an OTR screen and allows bunch length measurements.

EMITTANCE EVOLUTION

In the CLIC decelerators, the 3σ beam envelope can according to simulations fill around half the aperture [1]. It is therefore important that the transverse beam dynamics through deceleration is well understood, and that there are no unknown effects on the transverse beam size.

One important parameter which we can verify experimentally is the transverse emittance. We can compare the phase space (including the Twiss parameters) in one transverse plane by

1. performing one or more quad scans at the beginning of the TBL,
2. using the quad scan results as input to a simulation code, in this case the tracking code Placet [6],
3. performing one or more quad scans at the end of the TBL and comparing the results with the expected values from the simulation.

This comparison has been performed for different beam currents in TBL. Figure 2a shows a comparison for a factor 4 bunch combination, corresponding to a beam current of 13.5 A and 25 % deceleration. The plot is similar to a standard quad scan plot, where the beam size is shown as a function of the focusing of one quadrupole.

Based on the uncertainties in the Twiss parameters and emittance at the beginning of TBL, a number of Placet simulations were run with different input parameters. The resulting beam size at the end of TBL has an uncertainty,

ISBN 978-3-95450-122-9

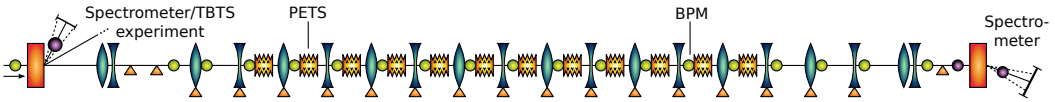

Figure 1: The current TBL lattice with 12 out of 16 PETS installed, with the CTF3 drive beam arriving from the left. Quadrupoles are shown as blue lenses, dipoles as red rectangles, correctors as orange triangles, BPMs as green circles, OTR screens as purple circles and PETS as brown corrugated structures.

given by the simulation results, that is represented by the blue band in Figure 2a. The blue line represents the simulated condition using the mean measured values from the beginning, which were also used for matching the TBL. Measured quad scans at the end of TBL are shown with black error bars and a corresponding quadratic fit. The measurements agree very well with the simulations, and we conclude that evolution of the transverse emittance is well understood.

We also show a similar comparison between measurements and simulations for an uncombined beam, corresponding to a beam current of 3.5 A and 7 % deceleration, in Figure 2b. Here the measurements disagree with the simulations. However, the beam size at the waist is roughly the same, but the waist is wider. We therefore believe that the emittance behaves as expected, but that the error lies in the Twiss parameters, maybe due to a drift of the machine. When the measurement was performed, the TBL was still matched and optimized for transporting the combined beam measured in Figure 2a, and this is a further uncertainty factor, even though the simulations were performed with the same optics. In the future we want to repeat the measurement for the uncombined beam, and also match the line for that beam.

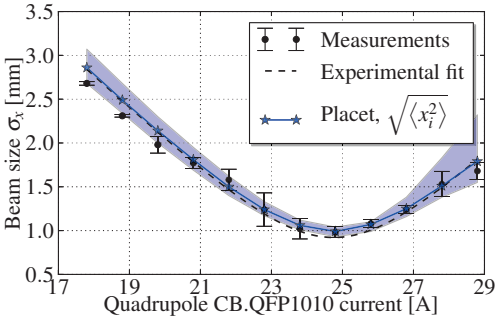

(a) Factor 4 bunch combination, 25 % deceleration.

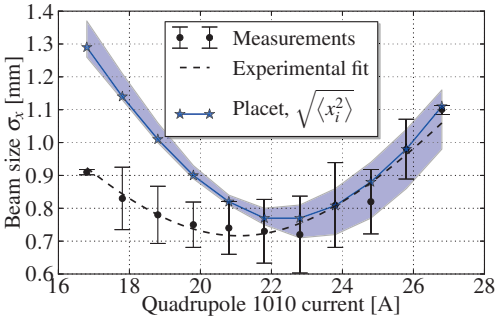

(b) Uncombined beam, 7 % deceleration.

Figure 2: Emittance evolution in the TBL. The plots represent quad scans done at the end of TBL. The simulations are based on the Twiss parameters and transverse emittance from the beginning of TBL. The emittance agrees well for both cases, while there is some uncertainty in the Twiss parameters for the uncombined beam.

DECELERATION

Energy measurements are regularly performed in the TBL, and the energy of the decelerated beam is compared to predictions from the measured beam current and from the rf power measured in the PETS. In Figure 3 one such measurement is shown, where the measured energy along the bunch train is shown in blue. The predicted deceleration based on the measured beam current is shown in red, while the prediction based on the measured PETS rf power is shown in green. A total of 60 pulses was used in the analysis. The means of the three measurements over the 60 pulses are shown with solid lines, while the standard deviations of the distributions are shown as colored bands.

When correlating the two predictions with the spectrometer measurements, one uncertainty is the charge distribution form factor $F(\lambda)$. This parameter takes the value of unity for infinitely short bunches with a perfect bunch phase. Based on bunch length and phase measurements, a reasonable estimate most of the time [7] is $F(\lambda) \leq 0.90$. One example of this is the bunch length measurement in Figure 4. Ignoring bunch phase effects and assuming Gaussian bunches, we can use the single bunch form factor

$$F(\lambda) = F_b(\sigma_z) = \exp\left[-\frac{1}{2}(\sigma_z 2\pi f_b/c)^2\right], \qquad (1)$$

where σ_z is the bunch length, f_b the bunch frequency and c the speed of light in vacuum. Using eq. (1) and the data in Figure 4 (including error bars), we obtain $F_b(\lambda) \in [0.81, 0.88]$.

In Figure 3 the form factor is used as a fudge factor, and a value of 1.05 had to be assumed, which is non-physical. A possible explanation can be an offset in the spectrometer, either because of a calibration error or a non-centred beam. Another issue is that the dipole magnet cannot currently be demagnetized correctly. To investigate a possible system-

ISBN 978-3-95450-122-9

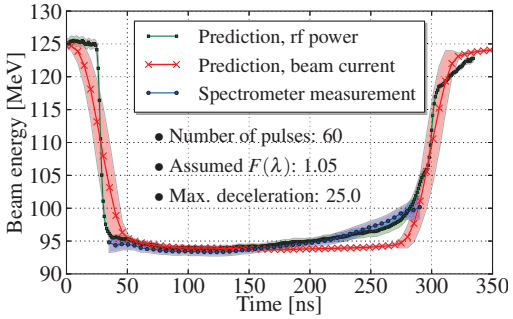

Figure 3: Deceleration of a 12.5 A beam through TBL. The measured energy along the pulse is shown, together with predictions based on the measured beam current and PETS rf power. Each colored band represents the mean ± the standard deviation.

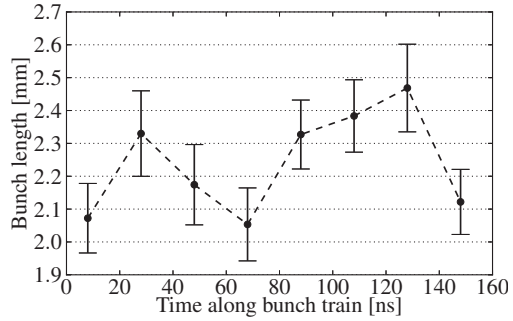

Figure 4: Streak camera measurement, where the bunch length (measured in sigmas) is shown at 8 points along the bunch train.

atic error, an experiment was performed where the the final beam energy was measured for different beam currents, and this is shown in Figure 5. A linear fit was used to find the intersect, which represents the beam energy without deceleration. This should correspond to the measured incoming energy of 125 MeV, but the intersect is 3 % lower. However, it is still inside the 95 % confidence interval of the fit, and therefore no conclusion can be made.

For the prediction from rf power there is also another uncertainty, namely the rf calibration. In Figure 3 an 8 % calibration error had to be assumed, something which is within the expected 10 % calibration uncertainty.

As seen in Figure 3, the agreement is worse at the end of the pulse. This mainly originates from a change in the form factor (bunch length and phase) along the pulse, which started upstream of the TBL. Figure 4 does not show the whole bunch train, but there is a tendency towards longer bunches at the end (except for the last point).

As shown by Figure 3 we can currently reach 25 % deceleration with a 12.5 A beam. Later this year it is expected

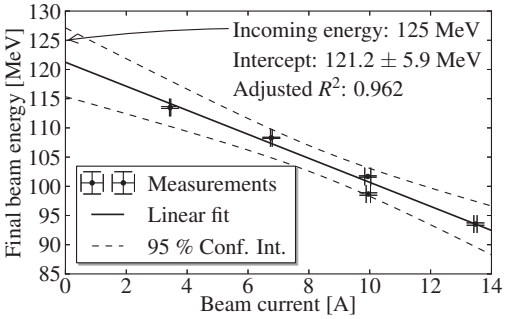

Figure 5: Measured beam energy at the end of TBL versus the beam current. A fit to the data determines the intersect, which represents the beam energy with no deceleration.

to operate with a beam current above 20 A, and it is reasonable to expect more than 40 % deceleration before the end of the year.

CONCLUSION

The TBL currently operates with 12 PETS, and has reached 25 % deceleration with a beam current of 12.5 A. There is generally good agreement with theoretical expectations. However, a small systematic uncertainty in the spectrometer measurements is still a concern even though it is not evident from the current data.

With 25 % and 7 % deceleration we have studied the evolution of the transverse emittance through deceleration in PETS. The emittance measurements agree very well with theory, except for some difference in the Twiss parameters for one measurement.

CTF3 is now starting high-current operation, and TBL will likely reach 40 % deceleration before the end of 2013.

REFERENCES

[1] M. Aicheler et al., *A Multi-TeV Linear Collider Based on CLIC Technology: CLIC Conceptual Design Report*, Geneva, 2012

[2] R.L. Lillestøl, *Power Production Experiments at the Test Beam Line in the CLIC Test Facility 3*, MSc thesis, NTNU, Trondheim, 2010.

[3] F. Toral et. al., "Design, Manufacturing and Tests of a Micrometer Precision Mover for CTF3 Quadrupoles", EPAC'08, Genoa, 2008.

[4] J.J. Garcia-Garrigos et al., *Design and Construction of a Beam Position Monitor Prototype for the Test Beam Line of the CTF3*, PhD thesis, Universitat Politecnica de Valencia, Valencia, 2009.

[5] M. Olvegaard et al., "Spectrometry in the Test Beam Line at CTF3", IPAC'10, Kyoto, 2010.

[6] `https://savannah.cern.ch/projects/placet/`.

[7] R. Lillestol et al., "Experimental verification of the CLIC decelerator with the Test Beam Line in the CLIC Test Facility 3", IPAC'12, New Orleans, 2012

A.3 Longitudinal space charge in the CLIC drive beam

- **Title**: Longitudinal Space Charge Effects in the CLIC Drive Beam
- **Abstract**: The CLIC main beam is accelerated by rf power generated from a high-intensity, low-energy electron drive beam. The accelerating fields are produced in Power Extraction and Transfer Structures, and are strongly dependent on the drive beam bunch distribution, as well as other parameters. We investigate how longitudinal space charge affects the bunch distribution and the corresponding power production, and discuss how the bunch length evolution can affect the main beam. We also describe the development of a Particle-in-Cell space charge solver which was used for the study.
- **Where**: The 4$^{\text{th}}$ International Particle Accelerator Conference, IPAC'13, Shanghai, China
- **When**: May 2013
- **Contribution**: Reidar was the main author, and wrote the entire article. He wrote the simulation code described after discussions with co-authors, and performed all the simulations. Reidar presented the work with a poster at the IPAC conference in Shanghai.
- **Authors**: R. L. Lillestol, S. Doebert, A. Latina, D. Schulte, E. Adli and K. N. Sjobak
- **Bibliography entry**: [47]

LONGITUDINAL SPACE CHARGE EFFECTS IN THE CLIC DRIVE BEAM

R.L. Lillestol*, S. Doebert, A. Latina and D. Schulte, CERN, Geneva, Switzerland
E. Adli and K.N. Sjobak, University of Oslo, Norway

Abstract

The CLIC main beam is accelerated by rf power generated from a high-intensity, low-energy electron drive beam. The accelerating fields are produced in Power Extraction and Transfer Structures, and are strongly dependent on the drive beam bunch distribution, as well as other parameters. We investigate how longitudinal space charge affects the bunch distribution and the corresponding power production, and discuss how the bunch length evolution can affect the main beam. We also describe the development of a Particle-in-Cell space charge solver which was used for the study.

INTRODUCTION

In the Compact Linear Collider (CLIC) scheme [1], the main beams are accelerated by rf fields extracted from two high-intensity, low-energy drive beams, before being brought into collision. These fields are extracted in Power Extraction and Transfer Structures (PETS), which are passive microwave structures with a fundamental mode at 12 GHz. In order to keep a high luminosity for the main beams, strict tolerances are necessary for several parts of the machine. One factor that affects the rf fields sent to the main beam is the drive beam bunch length. Assuming perfect bunch phase, the power produced in a single PETS scales as $P \propto F_b^2(\lambda)$, where $F_b(\lambda)$ is the single-bunch form factor. For a Gaussian bunch it can be written

$$F_b(\lambda) = F_b(\sigma_z) = \exp\left[-\frac{1}{2}(\sigma_z 2\pi f_b/c)^2\right], \qquad (1)$$

where σ_z is the bunch length, f_b is the bunch frequency and c is the speed of light in vacuum.

The nominal drive beam bunch length is 1 mm. The bunch length tolerance can be calculated from a specification for the main beam of maximum 1 % luminosity loss, which requires an energy spread of $\frac{\Delta E}{E} < 7 \times 10^{-4}$. This leads to a tolerance for a coherent bunch length change of 1.1 %, and a tolerance for an incoherent bunch length change of 3.3 %.

Even though the CLIC drive beams are relativistic ($\gamma \in [470, 4700]$ in the decelerator), there has been some concern that longitudinal space charge in the high-intensity bunches may violate the bunch length tolerance. This has previously not been studied for the CLIC scheme. In this paper we describe the development of a simulation code and its preliminary results.

* reidar.lunde.lillestol@cern.ch

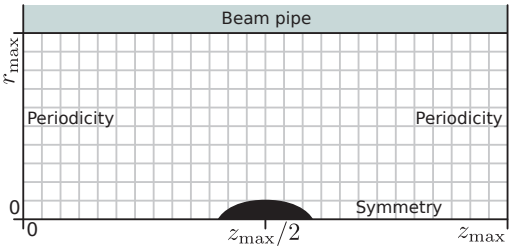

Figure 1: The system that is modeled. A bunch is placed on axis in an axisymmetric r-z grid. The maximum z value $z_{\max}$ is equal to the bunch separation.

MODEL

A common method for simulating space charge and similar effects in simulation codes is using the Particle-in-Cell framework (PIC). Because it is a well-known scheme that is intuitive and relatively straightforward to implement, PIC was chosen as the framework. It is foreseen to implement the space charge code into the existing tracking code Placet [2], and PIC should be compatible with the particle tracking in that code.

A full 3D PIC simulation requires a large amount of memory (e.g., fieldsolver matrices require $n_x^2 n_y^2 n_z^2$ elements, where $n_{x,y,z}$ is the number of grid points in each dimension) and extensive computation time. A 1D longitudinal code would have long-range Coulomb forces (the force is constant and does not fall off with distance) and overestimates the longitudinal force for particles outside the axis. A compromise was therefore chosen with a 2D code with cylindrical coordinates (r,z). This model – shown in Figure 1 – assumes axisymmetry, which is a simplification but applicable to the fairly round beams in the decelerator FODO lattice. Each code iteration follows a fairly standard PIC algorithm:

1. Define a grid for one bunch in the beam frame, based on its current energy in the lab frame. Because of length contraction the longitudinal coordinates scale with the Lorentz γ. A fixed number of grid points is used every iteration.

2. Assign charge with a linear, cloud-in-cell weighting to grid points near the particles.

3. Calculate charge densities on the grid points based on the volumes they represent.

ISBN 978-3-95450-122-9

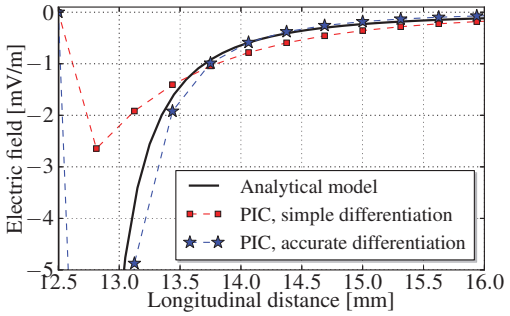

Figure 2: Longitudinal electric field from a point charge, where the PIC code is compared to an analytical model. For this grid size we clearly see the difference between the two types of numerical differentiation.

4. Solve Poisson's equation to obtain the potential ϕ everywhere on the grid.
5. Calculate electric fields from $\vec{E} = -\nabla\phi$. Magnetic fields are ignored since we solve in the beam frame.
6. Assign electric fields to each particle, in a linear cloud-in-cell manner.
7. Calculate particle kicks (i.e., update velocities and positions) from Lorentz' equation $\vec{F} = q\vec{E}$ and by using a leap-frog algorithm.

During the development it was found that normal 2-point numerical derivatives did not give accurate solutions for certain grid sizes and particle distributions. Therefore more accurate derivatives are used, and we write Poisson's equation for a free space grid point as

$$\begin{aligned}\nabla^2\phi|_{i,j} \approx & \frac{1}{r_i}\frac{\phi_{i-2,j} - 8\phi_{i-1,j} + 8\phi_{i+1,j} - \phi_{i+2,j}}{12\Delta_r} \\ & + \frac{-\phi_{i-2,j} + 16\phi_{i-1,j} - 30\phi_{i,j} + 16\phi_{i+1,j} - \phi_{i+2,j}}{12\Delta_r^2} \\ & + \frac{-\phi_{i,j-2} + 16\phi_{i,j-1} - 30\phi_{i,j} + 16\phi_{i,j+1} - \phi_{i,j+2}}{12\Delta_z^2} \\ & = -\frac{\rho_{i,j}}{\epsilon_0},\end{aligned} \tag{2}$$

where $\phi_{i,j}$ is the potential and $\rho_{i,j}$ is the charge density at coordinates $(r = r_i, z = z_j)$, ϵ_0 is the electric permittivity in vacuum and $\Delta_{r,z}$ is the grid length in each dimension. Figure 2 shows a comparison between the two numerical differentiation schemes. In this example a coarse grid in the r dimension shows that the more accurate differentiation clearly outperforms the simpler version.

A sketch of the system that is simulated is shown in Figure 1. The bunch is situated at $r = 0$, and this axis has a Neumann boundary condition with $\frac{\partial}{\partial r}\phi = 0$ to represent symmetry. Longitudinally, the grid spans from half the distance to the previous bunch, to half the distance to the next bunch. To eliminate any effects of bunch phase we use periodic boundary conditions longitudinally. A bunch offset from the longitudinal center would therefore not have an impact on the simulation. At the final boundary, which is the beam pipe, the potential is fixed to $\phi = 0$.

IMPLEMENTATION

The code has been written in Octave. The tracking code Placet [2] has an interface to Octave, and at a later stage this will make an implementation of the space charge code into Placet easier. Octave also offers a good environment for development.

Matrices used for the fieldsolver are stored in sparse format, which offers very good compression since the matrices have at most 9 diagonals. In this way we can use larger grids without running into memory problems. We solve for the potential using incomplete LU factorization, which was found to be the fastest method for large grids, and which operates on sparse matrices.

Several steps have been made to optimize the code for speed. However, since the energy changes along the decelerator, the grid (in the beam frame) and the field solver matrices must be remade every timestep, including the incomplete LU factorization. To increase the speed of this bottleneck, the chosen solution is to store normalized sparse matrices, which are scaled each iteration. Still, each iteration takes around 1.5 s for the conditions normally used (51×61 grid size and 10'000 macro particles).

BENCHMARKING

The code results have been compared to a number of analytical models. Mainly we have compared the electric fields, which agree reasonably well. One example is shown in Figure 2, which shows the longitudinal electric field close to a point particle. Another example is shown in Figure 3, which shows the longitudinal electric field from a bunch with a Gaussian longitudinal distribution with all particles placed on the axis transversally. In this particular analytical model we integrated a Gaussian distribution numerically to obtain the field everywhere on the axis.

For a small number of grid points in the r dimension and certain distributions like the Gaussian, the code has been found to underestimate the longitudinal field. To get a sufficiently accurate solution, we therefore need at least 60 points for a converging solution. This effect can be seen in Figure 3, where the field from the 41×51 grid ($r \times z$, in red) is underestimated (even though it converges in the Gaussian tails).

FIRST RESULTS

Some preliminary results have been obtained. However, since the code is not yet implemented in Placet, quadrupole focusing and beam dynamics other than space charge is not included. Therefore the simulations are quite simplified, and should be seen as the first stage of a study.

One simulation treated the decelerator as a long drift space, where the beam energy changed stepwise from 2.4 to 0.24 GeV from the 1492 PETS in the lattice. We used

ISBN 978-3-95450-122-9

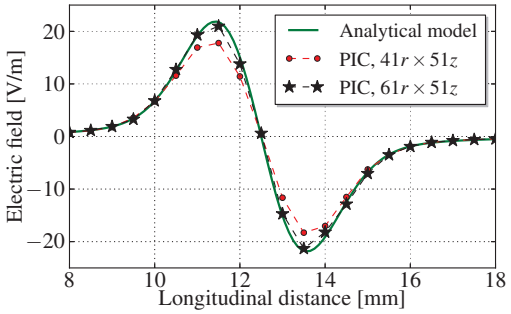

Figure 3: Longitudinal electric field from a bunch that is Gaussian distributed longitudinally and placed on axis transversally. 10'000 macroparticles were used in the PIC code and the result is compared to an analytical model. It is necessary to use at least 60 grid points radially to ensure convergence.

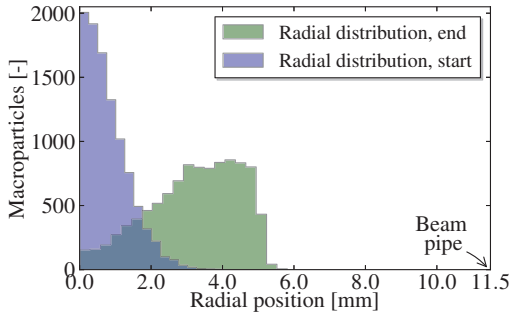

Figure 4: Radial bunch distribution before and after going through the CLIC decelerator (without quadrupole focusing).

nominal starting parameters, a 61×51 grid and 10'000 macro particles. The particles also started out stationary, which means zero emittance and energy spread. With these conditions the bunch length barely increased, with a factor $(1 + 6 \times 10^{-7})$. This is well within the coherent bunch length tolerance of 1.1 %, and has a negligible effect on the PETS power production. The space charge effect is more noticable transversally, where the beam occupies half the aperture as shown in Figure 4. However, when quadrupole focusing is included later we expect it to correct the transverse space charge defocusing, and also increase the longitudinal effect.

A similar simulation was performed for the Test Beam Line [3] in the CLIC Test Facility 3, which is a prototype CLIC decelerator. In this simulation the beam was decelerated from 120 to 60 MeV with 16 PETS, and here we also got a negligible bunch lengthening of a factor $(1 + 5 \times 10^{-5})$.

FUTURE PROSPECTS

It is foreseen to implement the space charge code into the Placet code. One approach for how it could work inside Placet, is that each time the tracker encounters a lattice element, it should estimate a number of timesteps that is needed for numerical convergence. This is based on the length of the current lattice element and the stability criterion [4]

$$\delta_t \leq \frac{1}{c} \frac{1}{\sqrt{\frac{1}{\Delta_r^2} + \frac{1}{\Delta_z^2}}}, \tag{3}$$

where δ_t is the timestep. The calculated positions and velocities at the end of the lattice element can then be interleaved with the other effects calculated in Placet.

After being merged with Placet, it will be possible to benchmark the code with more advanced models using other existing codes.

Adding the space charge effect to Placet will force it to run considerably slower, particularly because the field solver matrices are updated every iteration. Therefore it will likely be an effect that can be used by demand.

CONCLUSION

A PIC code for space charge has successfully been developed in Octave, and benchmarked with some analytical models. Simulations have been performed for the CLIC decelerator without quadrupole focusing, and showed a negligible bunch lengthening. In the future it is foreseen to implement the space charge code in Placet, and this will allow simulations closer to the real case. In particular the goal is to verify that longitudinal space charge is not an issue for PETS power production and for luminosity loss in CLIC.

ACKNOLEDGEMENTS

The authors want to thank Steven M. Lund of the Lawrence Berkeley and Lawrence Livermore National Laboratories, for helpful discussions and tips during the code development.

REFERENCES

[1] M. Aicheler et al., *A Multi-TeV Linear Collider Based on CLIC Technology: CLIC Conceptual Design Report*, Geneva, 2012.

[2] `https://savannah.cern.ch/projects/placet/`.

[3] R. Lillestol et al., "Experimental Results from the Test Beam Line in the CLIC Test Facility 3", these proceedings.

[4] A. Taflove and M.E. Brodwin, "Numerical Solution of Steady-State Electromagnetic Scattering Problems Using the Time-Dependent Maxwell's Equations", IEEE Trans. Microwave Theory & Techniques MTT-23, 623, 1975.

ISBN 978-3-95450-122-9

A.4 Experimental verification of the CLIC two-beam technology in CTF3

- **Title**: Experimental verifiction of the CLIC two-beam acceleration technology in CTF3
- **Abstract**: The Compact Linear Collider international collaboration is pursuing an extensive R&D program towards a multi-TeV electron-positron collider. In particular, the development of two-beam acceleration technology is the focus of the CLIC test facility CTF3. In this paper we summarise the most recent results obtained at CTF3: the results of the studies on the drive beam generation are presented, the achieved two beam acceleration performance is reported and the measured breakdown rates and related observations are summarised. The stability of the deceleration process performed over 12 subsequent modules and a comparison of the obtained results with the theoretical expectations are discussed. We also outline the future experimental program.
- **Where**: The 4^{th} International Particle Accelerator Conference, IPAC'13, Shanghai, China
- **When**: May 2013
- **Contribution**: Reidar contributed to the article with the plot in Figure 5, where he performed the experiment and the data analysis. He also provided input for the text about the TBL, and participated in the analysis of the R_{56} effects.
- **Authors**: B. Constance, A. Andersson, J. Barranco, R. Corsini, S. Doebert, A. Dubrovskiy, P. K. Skońwronski, F. Tecker, W. Farabolini, T. Persson, R. L. Lillestol, E. Ikarios, M. Jacewicz, A. Palaia, R. Ruber
- **Bibliography entry**: [41]

EXPERIMENTAL VERIFICTION OF THE CLIC TWO-BEAM ACCELERATION TECHNOLOGY IN CTF3

B. Constance*, A. Andersson, J. Barranco, R. Corsini, S. Doebert, A. Dubrovskiy, P. K. Skowroński, F. Tecker, CERN, Geneva, Switzerland
W. Farabolini, CERN, Geneva, Switzerland & CEA/DSM/IRFU, Saclay, France
T. Persson, CERN, Geneva, Switzerland & Chalmers University of Technology, Gothenburg, Sweden
R. L. Lillestol, CERN, Geneva, Switzerland & University of Oslo, Oslo, Norway
E. Ikarios, CERN, Geneva, Switzerland & National Technical University of Athens, Athens, Greece
M. Jacewicz, A. Palaia, R. Ruber, Uppsala University, Uppsala, Sweden

Abstract

The Compact Linear Collider international collaboration is pursuing an extensive R&D program towards a multi-TeV electron-positron collider. In particular, the development of two-beam acceleration technology is the focus of the CLIC test facility CTF3. In this paper we summarise the most recent results obtained at CTF3: the results of the studies on the drive beam generation are presented, the achieved two beam acceleration performance is reported and the measured breakdown rates and related observations are summarised. The stability of the deceleration process performed over 12 subsequent modules and a comparison of the obtained results with the theoretical expectations are discussed. We also outline the future experimental program.

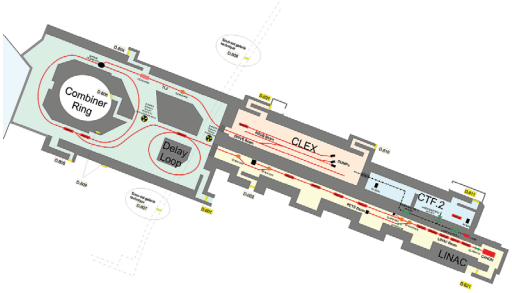

Figure 1: Layout of the CTF3 complex at CERN.

INTRODUCTION

A leading contender for the next generation of high energy lepton colliders, the Compact Linear Collider [1] (CLIC) is one of the two machine designs being pursued by the many international partners of the Linear Collider Collaboration. Integral to the verification of many aspects of the CLIC design is the work carried out at the CLIC Test Facility [2] (CTF3) located at CERN. In particular, a drive beam complex consisting of a 120 MeV e^- linac followed by a stretching chicane, a 42 m Delay Loop (DL) and an 84 m Combiner Ring (CR) is used to generate a high-current drive beam using a system of bunch frequency multiplication and pulse compression. This drive beam is then transported to the CLIC Experimental Area (CLEX) where it is used as a source of 12 GHz RF power.

A 3 GHz, 4 Amp beam from the linac, initially 1.5 µs long, can be injected directly into the CR using 3 GHz transverse deflecting RF cavities. Here it is stacked to produce a 12 GHz pulse of 16 A and of 280 ns duration. This mode of operation is referred to as factor 4 combination.

Alternatively, a sub-harmonic bunching system may be used to reduce the linac bunch frequency to 1.5 GHz. By coding the beam phase with a series of 180° phase shifts, 140 ns sections of the pulse may be alternately injected or allowed to bypass the DL. On exiting the DL, the delayed sections interleave with those sections bypassing. This results in a train of four 140 ns sub-pulses, separated by 140 ns, with a current of some 8 A and a 3 GHz bunch frequency. These four sub-pulses are then stacked in the CR before extraction to CLEX, where the final 12 GHz pulse is 140 ns long. The typically expected combined current is around 28 A before transport, since some fraction of the charge is lost to satellite bunches in the unused RF buckets. This is similarly referred to as factor 8 combination.

In CLEX, 12 GHz RF power is extracted from the drive beam using resonant Power Extraction and Transfer Structures (PETS). The drive beam may be directed to one of two beamlines: the Test Beam Line (TBL) or the Two-Beam Test Stand (TBTS). In TBL the stability of the drive beam under deceleration is assessed experimentally, and the produced RF power is compared to theoretical models. Two-beam acceleration studies are carried out in the TBTS, which is also served by a 200 MeV injector (CALIFES) to be used as a probe beam. RF power from the PETS is fed into two accelerating structures in the probe beam line.

STATUS OF DRIVE BEAM GENERATION

Recent drive beam studies have included the addition of software feedbacks to help improve beam stability and the commissioning of new stretching chicane optics to allow control of bunch length and beam phase. By careful closure of the CR orbit, it has also been possible to achieve emittances in both planes close to the design value of 150 π µm for a factor 4 combined beam

* ben.constance@cern.ch

ISBN 978-3-95450-122-9

New Feedback Tests

Unlike at CLIC, CTF3 relies on klystron pulse compression to generate the RF power necessary to accelerate the drive beam to 120 MeV. RF pulses of 5.5 μs are compressed down to around 1.5 μs using resonant cavities, increasing peak power by a factor of 2 to over 30 MW. This necessarily introduces a phase sag into the linac RF, which by design is transferred to the beam phase in such a way as to maintain constant acceleration along the beam pulse. In addition, despite temperature stabilisation of the compression cavities and RF phase feedback loops, this procedure has an adverse impact on the beam stability in both energy and phase. Two new feedbacks have been implemented to combat these effects [3].

In the first, feedback loops are closed between two beam phase monitors and the phases of the two 3 GHz bunching cavities. Each phase monitor is positioned just downstream of a bunching cavity. As the phase of the beam is seen to drift with respect to a more stable local oscillator, the beam bunching is adjusted to compensate. This ensures a more static working point against which to tune the rest of the machine, with the resulting improvement in beam phase at the end of the linac shown in figure 2 (a).

The second feedback loop is closed between the horizontal position read from the first dispersive BPM in the transfer line to the CR, and the power of the compressed RF fed to the last two accelerating cavities in the linac. Energy drifts leading to position drifts in the dispersive pick-up are thus compensated, giving a factor 2 improvement in stability as shown in figure 2 (b).

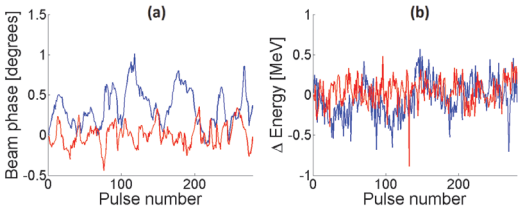

Figure 2: Effect of injector phase (a) and beam energy (b) feedbacks.

Control of the Stretching Chicane R_{56}

In previous runs, the stretching chicane at the end of the linac has been operated in its 'natural' state, with quadrupoles within the chicane off and with $R_{56} = 0.45$. In this configuration, an increase in RMS phase variation along the pulse of around a factor 5 was observed. Energy variations are coupled to beam phase by the large R_{56} value. Two new sets of optics were designed, with $R_{56} = 0.2$ and $R_{56} = 0$, to help control this effect, and the improvement is clearly visible in the data of figure 3 [4]. The new optics are also expected to affect the bunch length, though streak camera measurements have not yet been conclusive and require further study. The chicane is now regularly operated with a low R_{56}.

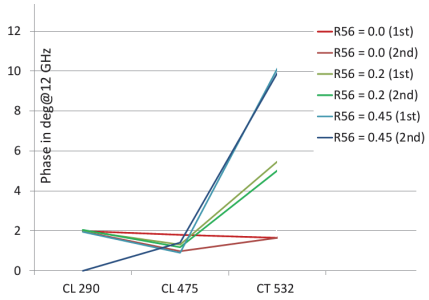

Figure 3: RMS phase variation measured in various phase monitors for different chicane R_{56} values. CL290 and CL475 are before the chicane and CL532 is after.

Factor 8 Combination

One outcome of the drive beam generation studies has been an increase in maximum current obtained by factor 8 combination to 26 A, with a good current stability along the pulse. Figure 4 shows the current over the four successive turns in the CR during such operation as measured in a BPM. The second half of each turn shows the current lost to satellite bunches due to imperfect sub-harmonic bunching, in this case around 4 A. CTF3 has 3 sub-harmonic bunchers each driven by a separate 1.5 GHz travelling wave tube (TWT), yet so far only 2 have been operated simultaneously. This has been due to limited TWT availability. With 3 TWTs available, it has previously been observed that the satellite current is reduced and therefore the maximum current achieved will likewise be increased.

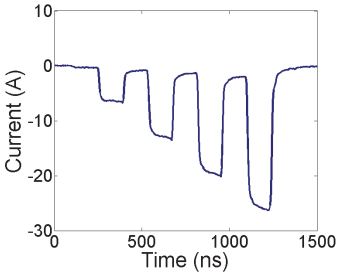

Figure 4: CR current over 4 turns during factor 8 combination.

STATUS OF THE TBL EXPERIMENT

Since the number of PETS in TBL was increased to 12 in the summer of 2012, a factor 4 combined beam has been successfully decelerated by 25% from 125 MeV. The decelerated beam was stably transported along the entire beam line to dump, and the final energy compared to theoretical predictions. See [5] in these proceedings for further details.

ISBN 978-3-95450-122-9

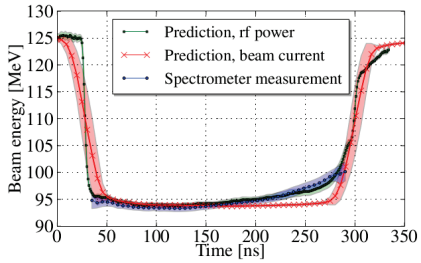

Figure 5: Beam energy along the factor 4 pulse at the end of TBL along with theoretical predictions. Coloured bands represent measured standard deviations

Figure 5 shows the energy along the pulse as measured in a spectrometer at the end of TBL, along with the predictions from beam current and produced RF power.

STATUS OF THE TBTS EXPERIMENT

Two accelerating structures are now installed in the TBTS and powered from a single PETS. With the nominal accelerating gradient (100 MV/m), the energy gain experienced by the probe beam will be 43.4 MeV for an input power of 42.2 MW each. Accurate checks of the structures' acceleration have been made for various powers and phases, and the performance is very close to expectation.

Concerning the breakdown rate, the structures are still in their very first period of conditioning. However, the location of the particular cell where breakdowns occur is quite evenly distributed for both structures. Conversely, the previous structure tested in the TBTS presented a hot spot around cell number 6.

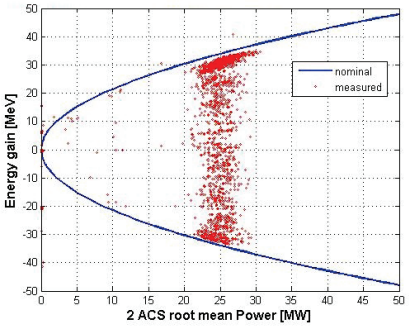

Figure 6: Measured probe beam energy gain vs. RF power. Most pulses are in the 20 to 30 MW range, and the beam to RF pase was scanned. Predicted curves are shown for in phase and in antiphase acceleration.

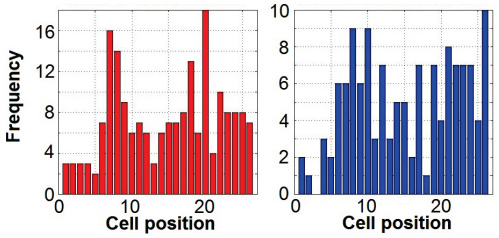

Figure 7: Frequency of recorded breakdowns in each cell of the two TBTS accelerating structures.

FUTURE PROGRAM

In addition to the consolidation of the drive beam development studies discussed here through software automation, and the demonstration of stable deceleration of a factor 8 beam through 12 PETS, there are several other studies planned at CTF3 in the coming months.

In the TBTS, the two new structures will be conditioned with drive beam RF and the breakdown rates measured. Two-beam acceleration experiments with a factor 8 beam will be performed, and new instrumentation to measure the drive beam wakefield tested. Kicks imparted to the beam during breakdown events will be measured and characterised.

A dogleg halfway down the linac allows the drive beam to be directed to a test accelerating structure. This structure is being driven by a 12 GHz X-Band klystron [6]. By delivering a 1 A beam from the linac, the intention is to compare breakdown rates in the cavity with and without beam loading.

Finally, a novel phase feed-forward system has been designed to correct the beam phase profile and jitter, demonstrating the possibility of reaching CLIC requirements. Further details may be found in [7] in these proceedings.

REFERENCES

[1] G. Guignard (Ed), "A 3 TeV e+e- linear collider based on CLIC technology,", CERN 2000-008, 2000.

[2] R. Corsini et al., "Experimental verification of the CLIC two-beam scheme, status and outlook", TUOBC01, IPAC2012

[3] A. Dubrovskiy and T. Persson, "Review of the drive beam stabilization in the CLIC Test Facility CTF3", WEPEA069, IPAC2013

[4] A. Gerbershagen, "CLIC Drive Beam Phase Stabilisation", D. Phil thesis, 2013

[5] R. L. Lillestol et al., "Experimental results from the Test Beam Line in the CLIC Test Facility 3", TUPWA046, IPAC2013.

[6] J. Kovermann et al., "Commissioning of the first klystron-based X-band power source at CERN", CERN-ATS-131

[7] P. K. Skowroński et al., "Design of Phase Feed Forward System in CTF3 and Performance of Fast Beam Phase Monitors", WEOBB203, IPAC2013

A.5 Experimental verification of the CLIC decelerator with the TBL

- **Title**: Experimental verification of the CLIC decelerator with the Test Beam Line in the CLIC Test Facility 3
- **Abstract**: The Test Beam Line in the CLIC Test Facility 3 is the first prototype of the CLIC drive beam decelerator. The main purpose of the experiment is to demonstrate efficient 12 GHz rf power production and stable transport of an electron drive beam during deceleration. The Test Beam Line consists of a FODO structure with high precision BPMs and quadrupoles mounted on mechanical movers for precise beam alignment. Nine out of the planned 16 Power Extraction and Transfer Structures have currently been installed and commissioned. We correlate rf power production measurements with the drive beam deceleration measurements, and compare the two measurements to the theoretical predictions. We also discuss the impact of the drive beam bunch length and bunch combination on the measurements.
- **Where**: The 3$^{\text{rd}}$ International Particle Accelerator Conference, IPAC'12, New Orleans, USA
- **When**: May 2012
- **Contribution**: Reidar was the main author, and wrote the entire article. He performed the experiments in participation with the co-authors, and carried out all the data analysis alone. Reidar presented the work with a poster at the IPAC conference in New Orleans.
- **Authors**: R. L. Lillestøl, S. Döbert, M. Olvegård, A. N. Rabiller, G. Sterbini and E. Adli
- **Bibliography entry**: [39]

EXPERIMENTAL VERIFICATION OF THE CLIC DECELERATOR WITH THE TEST BEAM LINE IN THE CLIC TEST FACILITY 3

R.L. Lillestøl*, S. Döbert, M. Olvegård, A.N. Rabiller, G. Sterbini, CERN, Geneva, Switzerland
E. Adli, University of Oslo, Oslo, Norway

Abstract

The Test Beam Line in the CLIC Test Facility 3 is the first prototype of the CLIC drive beam decelerator. The main purpose of the experiment is to demonstrate efficient 12 GHz rf power production and stable transport of an electron drive beam during deceleration. The Test Beam Line consists of a FODO structure with high precision BPMs and quadrupoles mounted on mechanical movers for precise beam alignment. Nine out of the planned 16 Power Extraction and Transfer Structures have currently been installed and commissioned. We correlate rf power production measurements with the drive beam deceleration measurements, and compare the two measurements to the theoretical predictions. We also discuss the impact of the drive beam bunch length and bunch combination on the measurements.

INTRODUCTION

In the proposed future e^+e^- collider CLIC, 90 % of the energy of a high intensity *drive beam* will be converted into 12 GHz rf power for acceleration of the main beam [1]. The CLIC Test Facility 3 (CTF3) was set up to verify key technology concepts of the CLIC scheme, and the decelerator Test Beam Line (TBL) is the first prototype of the CLIC drive beam decelerator, with up to 55 % energy extraction in the final configuration [2].

A part of the kinetic energy of the beam is converted to rf power in constant impedance Power Extraction and Transfer Structures (PETS), which are passive microwave devices with a fundamental mode of 12 GHz. The main purposes of the TBL are to

- show stable power production in the PETS,
- demonstrate stable beam transport after significant deceleration, and
- test decelerator beam-based alignment schemes.

EXPERIMENTAL SETUP

The Test Beam Line consists of 16 units, each with one Power Extraction and Transfer Structures (PETS), one quadrupole on a mechanical mover and one BPM. A FODO structure is used because of the large energy acceptance, and the quadrupole gradients are scaled along the line to provide a constant phase advance for the most decelerated particles (normally 90° per FODO cell). The TBL lattice is shown in Figure 1, and at the time of writing, 9 out of 16 PETS are installed. Both the current and the nominal beam parameters are given in Table 1 for comparison.

Because CLIC uses a 3.6 times more intense beam than the nominal CTF3 beam, the TBL PETS are a factor 3.7 longer, and will produce slightly more power than the baseline 135 MW required for CLIC. The longer PETS lead to a longer fill-time of the structure, and therefore a longer high-energy transient in the pulse. The 12 GHz power is coupled out on both sides at the end of the structures. At one side the power is measured with either IQ demodulators or Schottky diodes. The accuracy of the power measurements is estimated to be on the order of 10 %, because of an attenuation chain of 90 dB which must be calibrated piecewise [3].

A segmented dump spectrometer is installed at the end of the line [4], and provides time-resolved (ns) energy measurements with an accuracy of about 5 %. The start of the line is equipped with a spectrometer with a single slit. In addition, OTR screens are placed in both of these locations. A streak camera – imaging an OTR screen located at the beginning of the line – allows for bunch length and bunch spacing measurements.

TBL uses high precision inductive BPMs designed and constructed by IFIC Valencia and UPC Barcelona [5], with a resolution of 5 μm. The quadrupoles are mounted on moving tables made by CIEMAT [6], which allow positioning in the micrometer range. A beam-based alignment campaign has been performed in the TBL [7], and has improved the orbit and eased the transmission.

DECELERATION RESULTS

The TBL has been operated with different beam currents using various combination schemes of the CTF3 drive beam. For the deceleration studies, the main interest lies in using a high intensity beam since the deceleration is linear in current. We therefore report results from a fully combined beam (using both the CTF3 delay loop and combiner ring). Some parameters upstream of the TBL were not fully optimized at the time of taking data, particularly the overall bunch combination and the phase coding. Because of this there were electrons outside of the main pulse, which can also be seen in the PETS power production and deceleration.

The incoming beam energy was 117 MeV instead of the nominal 150 MeV designed for CTF3, because of two

* reidar.lunde.lillestol@cern.ch

ISBN 978-3-95450-115-1

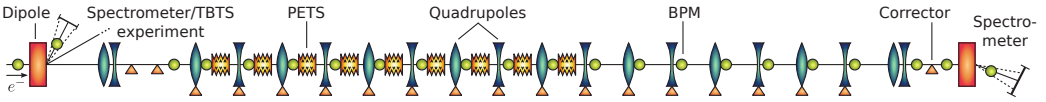

Figure 1: The TBL lattice with 9 out of 16 PETS installed, where the CTF3 drive beam comes from the left.

Table 1: Current (I) and nominal (II) parameters for the TBL for a fully combined beam. (*) corresponds to the PETS fundamental mode.

Parameter	Symbol	(I)	(II)
Number of PETS	N_{PETS}	9	16
Length of PETS [m]	L	0.80	0.80
Initial average current [A]	I	21	28
PETS power [MW]	P	70	138
Initial energy [MeV]	E_0	117	150
Mean energy extracted [%]	η	∼26	55
PETS synch. freq. [GHz]*	f_{rf}	12.0	12.0
PETS imped. [linac-Ω/m]*	(R'/Q)	2222	2222
PETS group velocity [c]*	v_g	0.46	0.46
PETS ohmic loss factor *	η_Ω	0.985	0.985
Pulse length [ns]	t_{pulse}	140	140
Transient length [ns]	t_{fill}	3.1	3.1
Repetition rate [Hz]	f_{rep}	0.83	≤ 5
Bunch rms length [mm]	σ_z	1-2	1.0
Init. norm. emittance [μm]	$\varepsilon_{N_{x,y}}$	∼500	150

missing klystrons in the CTF3 linac. The beam current was around 19 A (down from the nominal 28 A), mostly because of losses in the upstream transfer line.

The mean beam energy loss $\langle V \rangle$ can be deduced by three different methods based on three different measurements:

- Prediction from the measured PETS rf power P, using

$$\langle V \rangle = \frac{L}{2} F(\lambda,\phi) \sqrt{\frac{(R'/Q)\,\omega_{\mathrm{rf}} P}{v_g}} \qquad (1)$$

  with structure parameters from Table 1. $F(\lambda,\phi)$ is the charge distribution form factor, dependent on the bunch length and bunch spacing.

- Prediction from the measured beam current, using eq. (1) with

$$P = \frac{1}{4}(R'/Q)\frac{\omega_{\mathrm{rf}}}{v_g} L^2 I^2 F^2(\lambda,\phi)\,\eta_\Omega^2. \qquad (2)$$

- Direct measurement in the spectrometers.

The results of all three methods were correlated and are shown together in Figure 2, which shows the beam energy along the pulse. The circles, crosses and squares show mean values for the three measurement types over 48 consecutive pulses, corresponding to 58 seconds of operation. The colored bands around the means show one standard deviation for each measurement. This result corresponds to around 26 % deceleration and energy extraction, the highest achieved in the TBL so far.

The form factor $F(\lambda,\phi)$, which depends on both the bunch length and bunch phase (influenced by the bunch combination), affects both the deceleration and the power production. Here λ is the single-bunch charge distribution and ϕ is the bunch phase deviation from the synchronous phase. Since there was no direct form factor measurement available, it was used as a fudge factor in the analysis. The curves fitted well for a form factor of $F(\lambda,\phi) = 0.95$, close to the design value of 0.97 (corresponding to 1 mm Gaussian bunches with perfect phases, i.e., $\phi = 0$). In addition to this, the prediction from the rf power was scaled up by 10 %, and this deviation can be justified by the systematic error due to the very large signal attenuation before the electronics. The prediction from beam current deviates from the measurement and the prediction from rf power in the first part of the pulse, indicating a change in the form factor along the pulse. This probably originates from the CTF3 bunch combination.

In Figure 2, the rf derived signal is not shown outside of the main pulse. This is because the power production is quadratic in the current, and the measured satellites were much smaller than the main pulse, so that the signal there was not significantly above the noise floor.

A decelerated beam gets a larger envelope because of adiabatic undamping, making beam transport challenging when using many PETS. Most of the BPMs in the FODO structure were not calibrated with high beam currents and were saturated. They were therefore not usable for getting an estimate of the transmission. By trusting the very last BPM however, the transmission was close to 100 %, so operation with 9 PETS does not seem to have an impact on the transmission. Only the first BPM in the FODO lattice was used for the analysis in Figure 2 because of the saturation of the other BPMs. Since the curve still fitted the spectrometer measurement with a high form factor, this is also an indication of a good transmission.

FORM FACTOR ESTIMATES

The form factor is not known exactly in the power production and deceleration measurements, but can be estimated from streak camera measurements of the bunch lenghts and bunch spacings. One such measurement was performed with a 12 A beam. This gave bunch lengths of 1.9–2.8 mm, excluding one bunch which showed significant deviations from the others, one possible explanation being a measurement error. This corresponds to single-bunch form factors in the interval $F_\lambda(\lambda) \in [0.78,\ 0.89]$.

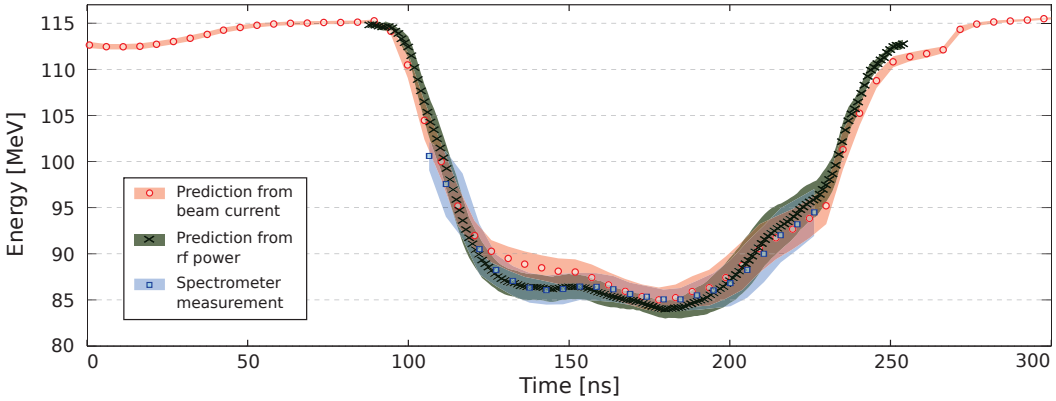

Figure 2: Beam energy along the pulse as measured in the spectrometer, and predicted from the beam current and the rf power. The symbols show the mean values over 48 pulses, while the bands show one standard deviation on each side.

In earlier work [2], the single-bunch form factor has been treated as the total contribution to the form factor. However, the bunch phase will also influence the power production and deceleration, and is especially important for a combined beam. For the same streak camera measurement, bunch spacings were used to calculate phase between bunches. A contribution to the form factor was then calculated using

$$F_\phi(\phi) = \frac{1}{N}\left|\sum_{n=1}^{N} e^{i\phi_n}\right| \qquad (3)$$

where ϕ_n is the phase deviation from zero for bunch n and N is the number of bunches in the measurement. This gave contributions to the form factor in the interval $F_\phi(\phi) \in [0.83,\ 0.88]$ along the pulse. The total form factor can be approximated $F(\lambda,\phi) \approx F_\lambda(\lambda)F_\phi(\phi)$[1], and therefore lies between $F(\lambda,\phi) \in [0.65,\ 0.79]$. The statistics of the streak measurement was low however, and it would be preferred to measure a larger number of bunches in the future.

The total form factor was estimated in the TBL from beam current and rf measurements in the same week, also using a 12 A beam, and gave values of $F(\lambda,\phi) \in [0.85, 0.90]$. This is outside of the interval calculated from the streak measurements, and the cause is likely that the machine and the beam had changed between the different days. For the next run, streak measurements should be taken in close connection to TBL operation for comparison.

CONCLUSION

The TBL has been operated with a total of nine PETS and a beam current of 21 A. Under these conditions a beam deceleration of 26 % was measured in the spectrometers. The measured energy loss was correlated with predictions from beam current and PETS rf power. A form factor of 0.95 and an adjustment of 10 % of the rf power had to be assumed.

The form factor contributions from bunch length and bunch spacing measurements have been evaluated. They differ from estimates from the beam current and rf power performed on different days. For the future we aim to perform both types of measurement on the same day for comparison. It is also preferable to take more streak measurements, also using a higher number of consecutive bunches.

For the next run, TBL will have 13 PETS installed, providing even higher deceleration, before eventually all 16 PETS are installed next winter. Effort will be made to improve the incoming beam parameters for the TBL, in particular the beam current. This will allow going towards the nominal 55 % deceleration.

We want to thank CIEMAT (Madrid), IFIC (Valencia), UPC (Barcelona) and the University of Oslo for their contributions to the TBL experiment.

REFERENCES

[1] *CLIC Conceptual Design Report*, to be published 2012.

[2] E. Adli, *A Study of the Beam Physics in the CLIC Drive Beam Decelerator*, PhD thesis, Uni. Oslo, Oslo, 2009.

[3] R.L. Lillestøl, *Power Production Experiments at the Test Beam Line in the CLIC Test Facility 3*, MSc thesis, NTNU, Trondheim, 2010.

[4] M. Olvegaard et al., "Spectrometry in the Test Beam Line at CTF3", IPAC'10, Kyoto, 2010.

[5] J.J. Garcia-Garrigos et al., *Design and Construction of a Beam Position Monitor Prototype for the Test Beam Line of the CTF3*, PhD thesis, Universitat Politecnica de Valencia, Valencia, 2009.

[6] F. Toral et. al., "Design, Manufacturing and Tests of a Micrometer Precision Mover for CTF3 Quadrupoles", EPAC'08, Genoa, 2008.

[7] G. Sterbini et al., "Beam-based alignment in CTF3 Test Beam Line", IPAC'12, these proceedings.

[1] Assuming an equal and even charge distribution per bunch, the total form factor can be separated with an equality.

ISBN 978-3-95450-115-1

A.6 Beam-based alignment in the TBL

- **Title**: Beam-based alignment in CTF3 Test Beam Line
- **Abstract**: The CLIC linear collider is based on the two beams acceleration scheme. During acceleration of the colliding beams, the drive beam suffers a large build up of its energy spread. In order to sufficiently transport such a beam, beam-based alignment techniques together with tight pre-alignment tolerances are crucial. To evaluate the performance of these steering algorithms, a beam-based steering campaign has been conducted at the Test Beam Line of the CLIC Test Facility. In the following we present and discuss the obtained results.
- **Where**: The 3rd International Particle Accelerator Conference, IPAC'12, New Orleans, USA
- **When**: May 2012
- **Contribution**: Reidar helped with the implementation of the algorithms towards the CTF3 control system. He participated in the experiments in the CTF3, but not in the data analysis. The article was written by G. Sterbini, but Reidar contributed with corrections to the text.
- **Authors**: G. Sterbini, S. Döbert, E. Marín, R. L. Lillestøl, D. Schulte and E. Adli
- **Bibliography entry**: [23]

BEAM-BASED ALIGNMENT IN CTF3 TEST BEAM LINE

G. Sterbini*, S. Döbert, E. Marín, R. L. Lillestøl, D. Schulte, CERN, Geneva, Switzerland
E. Adli, University of Oslo, Oslo, Norway

Abstract

The CLIC linear collider is based on the two beams acceleration scheme. During acceleration of the colliding beams, the drive beam suffers a large build up on its energy spread. In order to efficiently transport such a beam, beam-based alignment techniques together with tight pre-alignment tolerances are crucial. To evaluate the performance of these steering algorithms, a beam-based steering campaign has been conducted at the Test Beam Line of the CLIC Test Facility. In the following we present and discuss the obtained results.

INTRODUCTION

The Compact Linear Collider, CLIC, [1][2] is based on the two beams acceleration scheme: the colliding beams will be accelerated by decelerating a high intensity, low energy drive beam, DB. During its deceleration, the DB will increase its energy spread up to 90%. In this condition the beam transport is very challenging: beam-based alignment techniques together with tight pre-alignment tolerances are crucial to obtain the nominal performance. To reach the required level of pulse to pulse DB current jitter ($< 7.5 \times 10^{-4}$ [2]) the quadrupoles magnetic centre has to be pre-aligned with a RMS offset of 20 μm with respect to the laser straight reference. A beam-based steering campaign has been conducted at the Test Beam Line (TBL, [3]) of the CLIC Test Facility (CTF3) to evaluate and check several algorithms.

The TBL line consists of 8 FODO cells typically running with $\mu_x = \mu_y = 90°$ phase advance per cell. Each of the 16 quadrupoles is mounted on horizontal and vertical movers to allow beam based alignment (BBA) and has a BPM close by. At the moment of our experiments only 4 out of 16 Power Extraction and Transfer Structure (PETS) were installed in TBL. Hence the total deceleration produced on the beam was only 15%, having, as we will discuss later, a direct impact of the algorithm choice. In this condition the TBL beam transmission was, within the BPMs accuracy, almost complete even before automatic BBA. Nevertheless as we showed in simulations using the PLACET code [4] (Fig. 1), increasing the number of PETS beyond 8 and with full recombination current ($I_B = 28$ A) it is likely to require BBA even for routine operation. So the goal of this work is two-fold:

- to demonstrate the effectiveness of the BBA algorithms that will be used in CLIC,
- to ease the future operation of TBL and CTF3 lines.

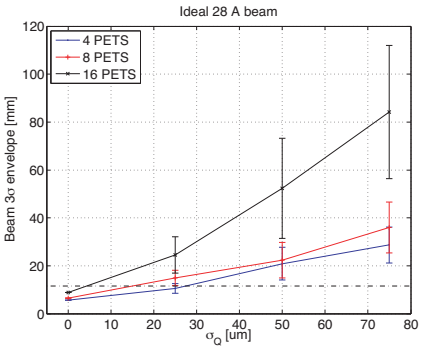

Figure 1: Effect of the quadrupoles misalignment on the TBL beam envelope at the end of the line. For comparison, the mechanical aperture of the PETS is $R = 11.5$ mm (dashed line). In the plot we show the results of a Montecarlo simulation: we vary the RMS misalignment of the quadrupole magnetic centre (σ_q) and we compute the 3σ envelope of the beam at the end of the line (99th percentile over 1000 seeds). We consider three different scenarios (4, 8 and 16 PETS in TBL) using the fully recombined beam ($I_B = 28$ A).

BEAM BASED ALIGNEMENT METHODS

In order to achieve the CLIC required DB efficiency and pulse-to-pulse reproducibility, the DB size has to be minimized along the decelerator. Neglecting the injections errors at the start of the decelerator, the DB envelope growth is dominated by the offset of the quadrupole magnetic centre with respect to the laser straight line. Since (1) the relation between quadrupole offset and envelope is non-linear, (2) the beam envelope is difficult to observe along the machine, instead of minimizing directly the envelope we can address the associate linear problem where we consider as observables to minimize (a) the horizontal and vertical betatron orbits and/or (b) the dispersive orbits at the BPMs all along the decelerator. These two different approaches are referred in the following as all-to-all and Dispersion Free Steering (DFS) correction [5]. The advantage of the DFS with respect to the all-to-all algorithm is its robustness against BPM accuracy being based on differential positions.

The response matrix, R, between observables and quadrupole positions is in general ill-conditioned: due to the finite BPM precision we cannot directly invert the problem but we can effectively correct the system using Singu-

* guido.sterbini@cern.ch

lar Value (SV) filtering: we neglect in the correction all the quadrupole eigen-directions that are barely detectable by the BPMs (corresponding to the lower singular values of the R's SV Decomposition). An equivalent approach is to consider as additional observables the correction vector itself that is the required offset of the quadrupoles. In this condition the algorithm tries to minimize the correction with respect to the pre-aligned machine thus becoming stable without SV filtering.

As already mentioned, at the moment of the tests only 4 PETS were installed in TBL producing a modest deceleration. It was difficult to measure the differential orbit induced by the quadrupole misalignment between decelerated and unperturbed beam. This difficulty was further increased by a dispersive wave propagating to TBL from the CTF3 ring. This led us to implement a BBA algorithm based only on the minimization of the orbit. In this framework we could operate even with a less intense beam (typically no recombination or factor 4 recombination, instead of factor 8 recombination more suitable for the DFS).

As an alternative and complementary method, the quadrupole shunting technique (QST) has been investigated too. This technique tries to directly center the magnetic centre of a single quadrupole. It consists in moving the magnet to three different positions (-Δu, 0, +Δu), where u stands for x and y, by means of a mover on which the quadrupole is mounted. At each position the current of the quadrupole is initially shunted by $\pm\Delta I$. From the orbit difference recorded by the downstream BPMs the magnetic centre (x_0, y_0) is inferred (position were the orbit difference is null). The values of Δu and ΔI are adjusted at each iteration in order to reduce beam losses during the measurement. The process is iterated until the obtained BBA resolution does not improve further. This method is very powerful since uses differential BPM reading (robust against BPM accuracy) and it can predict the exact zeros of the quadrupole without using response matrix of the system. Nevertheless the main assumption is based on is that during the shunting the magnetic centre motion is negligible. In reality, as we will discuss, this assumption cannot always be applied. Moreover this technique is expected to require much more commissioning time for the CLIC decelerator than the all-to-all and DFS algorithms and cannot fit the powering constraint of the DB quadrupoles (series connection, limited ΔI).

EXPERIMENTAL RESULTS

The experiment of BBA in TBL line has been approached in three different ways: (1) a non-iterative correction using SVD filtering and high gain (G=1), (2) an iterative correction using low gain (G=0.1), (3) and using quadrupole shunting technique.

High gain correction

In this condition, we observe the beam orbit averaging it in sets of 10-50 consecutive pulses. This is needed to increase the algorithm robustness mainly with respect to injection error in TBL and energy jitter in the CTF3 linac [6]. Once the error orbit is observed we compute the required offset of the quadrupole movers. Typically the pseudo-inverse of the response matrix is computed using only the first 9 SVs out of the 16 in total: with these parameters the RMS value of the corrected orbit is significantly reduced and, in the meantime, the correction strength lies within the acceptable range of the hardware (maximum mover offset). Typical values of the orbit before and after the correction are reported in Table 1 for the vertical and horizontal orbit: the RMS horizontal orbit was reduced from 1.65 to 0.31 mm and the vertical one from 1.30 to 0.61 mm. Typical trajectories before and after BBA are reported in Fig. 2.

Table 1: Comparison of the orbit before and after BBA.

	Before BBA	After BBA
Mean H, V orbit [mm]	-0.90, -0.69	0.22, -0.07
RMS H, V orbit [mm]	1.65, 1.30	0.31, 0.61

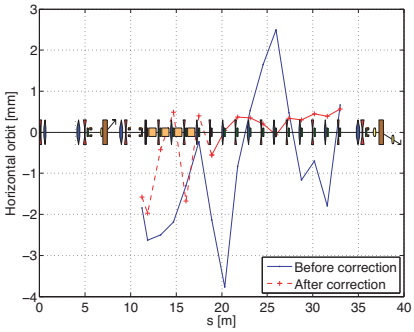

Figure 2: An example of the orbit correction performance in the horizontal plane before and after BBA.

The first part of the corrected trajectory (dashed line in Fig. 2) behaves like a damped oscillator. This is an expected behavior due to the error at the TBL injection and to the reduced SVs pseudo-inverse. In fact the algorithm will only partially use the quadrupole movers to correct the orbit error at the entrance of the line and it will take about one betatron oscillation to damp the oscillation. After this transient the corrected orbit reaches its steady state RMS. This approach has an important limit: due to the needed statistics on several beam pulses and to the CTF3 energy and orbit drift, when the corrections takes place the orbit used for correction is in general different from the actual orbit: this will originate a residual orbit even after correction. To avoid it, the use of a slow feedback correction is justified.

ISBN 978-3-95450-115-1

Slow feedback correction

In this approach we correct after each single beam pulse (no average for a long observation period) applying only partially the correction (typically G=0.1). In doing so we are much more robust against errors in the synchronization of the BPM reading, BPM precision, limited precision of the response matrix of the system[1] and machine drifts.In Fig. 3 the measurements of the vertical and the horizontal positions of the first two BPMs of TBL is shown during the feedback loop. As expected the damping of the orbit is an exponential with the time constant of 1/G=10 pulses. After 50 pulses the only components still visible are the pulse-to-pulse uncorrelated jitter that cannot be compensated by our feedback. A complete test of the slow feedback loop on the TBL full length has still to be done but the result obtained on the first part of the line are very encouraging.

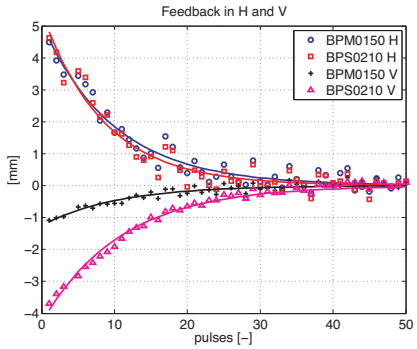

Figure 3: Measurement during orbit correction feedback.

Quadrupole shunting technique

An example of QST is shown in Fig. 4: we plot the orbit difference at 7 different BPMs when the ΔI is -20% and +20% of nominal current (I=2.56 A) for the three vertical positions of the quadrupole. The lines cross at the position 475 ± 25 μm indicating the magnetic centre of the quadrupole. We measured 9 quadrupoles out of 16 using QST: the obtained average error bar has been 200, 100 μm in the horizontal and vertical plane respectively. The limited precision of the measurements is probably due to the combination of the beam orbit jitter during the data acquisition, the precision of the BPMs if beam losses occur due to the induced beam perturbation, and the motion of the quadrupole magnetic centre due to the shunting. The latter contribution has been verified via direct magnetic measurements of a TBL quadrupole of similar characteristics [7]: in the range of our shunting current the measured motion of the magnetic centre is ≈ 7 μm. This effect even if not relevant at this stage in TBL, has to be taken into account in the design and the pre-aligment phase of the DB quadrupoles.

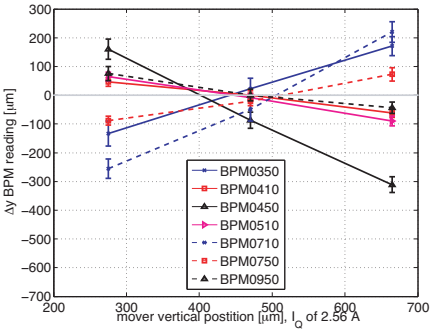

Figure 4: Example of quadrupole alignment using the QST.

CONCLUSIONS

In this work we reported the results of the beam based alignment in the Test Beam Line of CTF3.

The performance of the high gain correction algorithm appears to be limited by the beam orbit and energy drifts and not by the BPMs or movers resolution. To solve this problem a pulse-to-pulse orbit feedback has been set up and tested on the first BPMs of the line: it allowed to follow the CTF3 drifts and the results are in line with the expectation. In fact the residual orbit after correction is dominated by the uncorrelated pulse-to-pulse orbit jitter. After the test of the quadrupole shunting technique and the magnetic test of the TBL quadrupole, we pointed out a potential limit in the pre-alignment methods of the CLIC decelerator quadrupoles if its magnetic centre varies with the gradient: possible solutions are presently under investigation.

Helpful discussions with J. Barranco, R. Corsini, D. Gamba, I. Gorgisyan, A. Latina, J. G. Perez, T. Persson, P. Skowronski, F. Tecker and R. Tomás are gratefully acknowledged.

REFERENCES

[1] `www.clic-study.org`.

[2] "CLIC Conceptual Design Report", to be published.

[3] R. Lillestøl, "Power production experiments at the Test Beam Line in the CLIC Test Facility 3", NTNU, 2010.

[4] D. Schulte, `savannah.cern.ch/projects/placet`.

[5] E. Adli, Phd. Thesis, Uni. Oslo, Oslo, October 2009.

[6] T. Persson et al., "Beam stability at CTF3", these proceedings.

[7] J. G. Perez, private communication, 2012

[1] We know the linear response of the system, $\mathbf{R}$, within finite precision: the response matrix used for correction is $\overline{\mathbf{R}} = \mathbf{R} + \mathbf{\Delta R}$ that yields $\mathbf{X_n} = (\mathbf{I} - \overline{\mathbf{R}}^{+}\mathbf{R})^{\mathbf{n}} \times \mathbf{X_0}$, where X_n represents the residual orbit after n iteration. If $\overline{\mathbf{R}}$ is diagonalizable, we can still converge to $\lim_n \mathbf{X_n} = \mathbf{0}$ and only if the eigenvalues of $\mathbf{I} - \overline{\mathbf{R}}^{+}\mathbf{R}$ have module smaller than 1.

A.7 The CLIC feasibility demonstration in CTF3

- **Title**: The CLIC feasibility demonstration in CTF3
- **Abstract**: The objective of the CLIC Test Facility CTF3 is to demonstrate the feasibility issues of the CLIC two-beam technology: the efficient generation of a very high current drive beam, used as the power source to accelerate the main beam to multi-TeV energies with gradients of over 100 MeV/m, and stable drive beam deceleration. Results of successful beam acceleration with over 100 MeV/m energy gain are shown. Measurements of drive beam deceleration over a chain of Power Extraction Structures (PETS) are presented. The achieved RF power levels, the stability of the power production and of the deceleration are discussed. Finally, we give an overview of the remaining issues to be addressed by the end of 2011.
- **Where**: The 2nd International Particle Accelerator Conference, IPAC'11, San Sebastián, Spain
- **When**: September 2011
- **Contribution**: Reidar participated in the experiment that led to Figure 3, but did not make the plot itself. He contributed with information for the section about the TBL and the conclusion.
- **Authors**: P. K. Skowroński, J. Barranco, S. Bettoni, B. Constance, R. Corsini, M. Divall Csatari, A. E. Dabrowski, S. Doebert, A. Dubrovskiy, O. Kononenko, R. L. Lillestol, M. Olvegaard, T. Persson, A. Rabiller, F. Tecker, Wilfrid Farabolini, E. Adli, T. Muranka, A. Palaia, R. Ruber
- **Bibliography entry**: [19]

THE CLIC FEASIBILITY DEMONSTRATION IN CTF3

P.K.Skowroński, J.Barranco, S.Bettoni, B.Constance, R.Corsini, M.Divall Csatari, A.E.Dabrowski, S.Doebert, A.Dubrovskiy, O.Kononenko, R.L.Lillestol, M.Olvegaard, T. Persson, A.Rabiller, F.Tecker, CERN, Geneva, Switzerland
Wilfrid Farabolini, CEA/DSM/IRFU, Saclay, France
E.Adli, University of Oslo, Oslo, Norway
T.Muranka, A.Palaia, R.Ruber, Uppsala University, Uppsala, Sweden

Abstract

The objective of the CLIC Test Facility CTF3 is to demonstrate the feasibility issues of the CLIC two-beam technology: the efficient generation of a very high current drive beam, used as the power source to accelerate the main beam to multi-TeV energies with gradients of over 100 MeV/m, and stable drive beam deceleration. Results of successful beam acceleration with over 100 MeV/m energy gain are shown. Measurements of drive beam deceleration over a chain of Power Extraction Structures (PETS) are presented. The achieved RF power levels, the stability of the power production and of the deceleration are discussed. Finally, we give an overview of the remaining issues to be addressed by the end of 2011.

INTRODUCTION

The CLIC study aims to provide a design of a multi-TeV electron-positron collider [1]. The demonstration of its feasibility is carried out with the help of the CLIC Test Facility (CTF3) [2], in particular the generation and use of the high-current drive beam [3]. CTF3 was built at CERN by an international collaboration, which at present includes 41 institutes from 21 countries [4]. A detailed description of the facility can be found in [2,5].

CTF3 generates the drive beam from a 1.5 μs long electron pulse of 5 A intensity, see Figure 2. The injector, which includes a 1.5 GHz sub-harmonic bunching system, produces bunches spaced by 20 cm, twice the acceleration wavelength. Afterwards, bunches are compressed by a four bend chicane where off-energy electrons are also stopped by collimation slits. A pulse of 4 A intensity is injected into the linac and accelerated to about 120 MeV. Later, bunches are stretched by a chicane. The 42 m long Delay Loop (DL) converts the train to four 140 ns pulses of twice higher current, see Figure 2. They are transferred to the Combiner Ring (CR) where they are recombined producing a single 140 ns long pulse of eight times the intensity in the linac.

The CTF3 experimental area (CLEX) contains two lines where the beam is decelerated and 12 GHz power is produced. One is the Test Beam Line (TBL), where stable deceleration over several structures is studied. The other one is the Two-Beam Test Stand (TBTS), which provides power to accelerate the probe beam delivered by the CALIFES linac.

During previous runs, several feasibility issues of the CLIC design had already been shown and published: fully loaded acceleration with RF to beam efficiency of 95.3%, bunching with phase coding, bunch length control and beam recombination factor 8. The remaining issues are: 12 GHz RF power production with CLIC nominal pulse length (140 ns) and power level (135 MW), probe beam acceleration with a gradient of 100 MeV/m and stable deceleration.

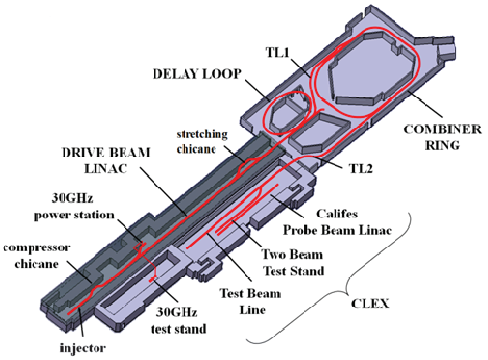

Figure 1: Layout of CTF3.

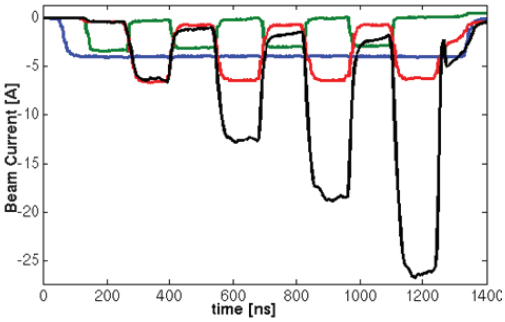

Figure 2: The beam current along the pulse at different parts of CTF3: blue – end of linac, green – in the DL, red – in between DL and CR, black – in the CR.

* Also NTNU, Trondheim, Norway
**Also Chalmers Univ. of Technology, Gothenburg, Sweden

THE DRIVE BEAM

During recent runs the reproducibility and stability of the drive beam was significantly increased. This was possible thanks to development of specialized control and software tools monitoring all available signals. They permitted the most important sources of the beam drifts to be spotted. The acquired knowledge triggered development of adequate feedback systems, e.g. temperature of various RF systems [6], the gun current and the flatness of the compressed RF pulses. Additionally, the RF scheme for the drive beam was improved in the beginning of the 2010 run. The RF power compression mechanism introduces an inevitable phase variation of parabolic shape along the pulse with amplitude of 7-10 degrees. In the previous setup, this led to bunch length, phase and energy variations along the pulse that made the beam optimization difficult. Since this year, the RF power compression is adjusted to give identical phase variation for all klystrons, and variable phase shifters controlled by arbitrary waveform generators are used to shape the phase variation of the bunching system to match the one from the RF power compression. This way the energy and also the bunch length along the pulse are constant. The variation of the bunch phase can be corrected with the help of the stretching chicane and appropriate energy modulation along the pulse in the last accelerating cavities.

STABLE BEAM DECELERATION AND RF POWER PRODUCTION

The Test Beam Line (TBL) was set up to verify the CLIC decelerator concept, and the main purpose is to produce 12 GHz RF power and to demonstrate the stability of a heavily decelerated beam [7]. It consists of 8 FO DO cells, and will eventually house 16 PETS which will extract 55 % of the beam energy. The design power produced per PETS is up to 139 MW. So far, 4 PETS have been installed and commissioned. The maximum achieved RF power has been 55 MW, for a beam current of 19 A. The PETS power scales as $P \propto F^2(\lambda)\, I^2$, where $F(\lambda)$ is the charge distribution form factor and I is the beam current.

The energy lost by the beam in the deceleration process can be calculated from the produced power, which in turn can be also inferred from the beam current. The deceleration is also measured directly in spectrometers with time resolution located at the beginning and the end of the TBL. Figure 3 contains a comparison between the three methods, which show a good agreement when the power measurements are scaled down by 10% which is within the uncertainty of the measurements. The current of the combined main pulse amounted to 18 A, preceded by satellites. A form factor of 0.85 was used for the prediction, consistent with recent bunch length measurements in CLEX.

The TBL has also been used as a diagnostic for the bunch combination in CTF3, by comparing BPM readings and RF measurements to estimate the form factor variation along the pulse [8]. Estimations over a large number of pulses, as well as phase signals, have been used to optimize the combination.

The quadrupoles in the FODO lattice are mounted on mechanical movers with a precision of 5 µm [9]. These have been used to investigate beam-based alignment techniques and steering algorithms including dispersion-free steering [10].

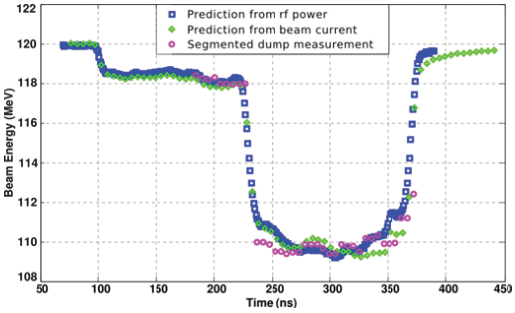

Figure 3: Measured deceleration in the spectrometer and predictions from the beam current and the PETS RF power.

TWO BEAM ACCELERATION

The Power Extraction Structure in the Two Beam Test Stand is longer than the TBL ones and is equipped with an RF power recirculation loop, thus allowing power levels up to and beyond 150MW, even with lower than nominal drive beam current.

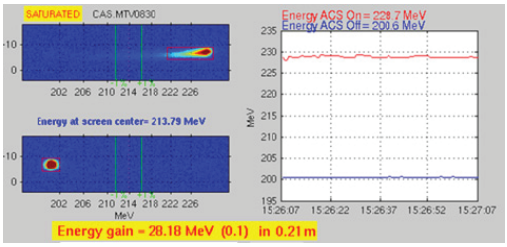

Figure 4: Screenshot of online acceleration measurement in the Two Beam Test Stand.

The probe beam delivered by the CALIFES injector has 190-200 MeV kinetic energy and a bunch charge of 0.12 nC. Its energy is measured with help of a profile monitor placed in the spectrometer at the end of the line. Its repetition rate is twice of the drive beam and in this way the energy gain from the two beam acceleration is measured in a truly online manner, see Figure 4.

Already in 2010 we have achieved an acceleration of 100 MeV/m. However, the required power levels were considerably higher than expected. A detailed examination of the structure revealed that the frequency of the accelerating cavity was 10 MHz too high due to accidental mechanical stress experienced during its

assembly. Over the last winter shutdown the cavity was re-tuned and its performance was validated during the last run, reaching an energy gain of 150 MeV/m. Figure 5 shows measured acceleration versus input power of the structure, together with the predicted curve. We believe that the observed discrepancy is mainly due to imperfect accuracy of the RF power measurements. Other possible sources for a lower gradient are drive-beam/probe-beam synchronization and phase but these were carefully optimized.

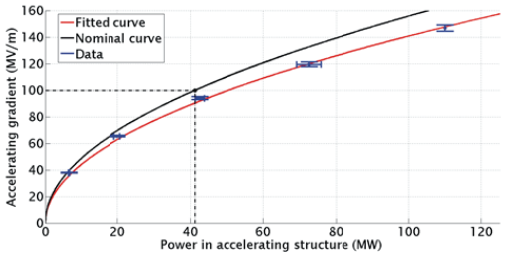

Figure 5: Accelerating gradient as function of measured RF input power. The line represents the theoretical curve.

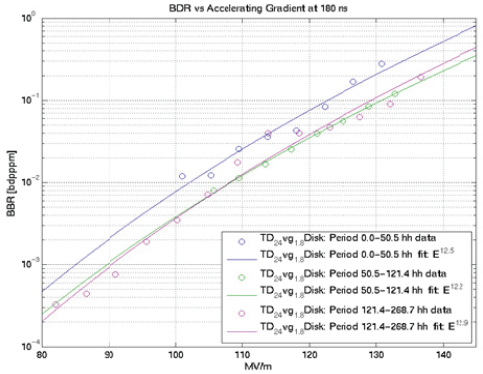

Figure 6: The break down rate versus accelerating gradient measured in the Two Beam Test Stand of CTF3.

Figure 6 presents the measured break down rate as a function of accelerating gradient. The repetition rate of the beam is only 0.8 Hz at present in CTF3 therefore the structure processing is much more aggressive in CTF3 compared to a klystron driven experiment. As a consequence this kind of data can't be easily compared and only an upper limit can be determined form the CTF3 experiments. The total conditioning time in CTF3 is equivalent to less than 24 hours of a klystron based processing at 60 Hz. The CLIC study managed to demonstrate breakdown rates below 3 10^{-7} corresponding to the CLIC target value after more than 1000 hours of processing at 60 Hz [11].

CONCLUSIONS AND OUTLOOK FOR FUTURE

CTF3 has already shown most of the feasibility issues of the drive beam generation scheme. Fully loaded acceleration is routinely used since 2004. The bunch length is well controlled. Stable acceleration with the nominal CLIC gradient of 100 MV/m was accomplished and maximum gradients of 150 MV/m were reached. The dependence of acceleration as a function of delivered RF power is in very good agreement with the predicted curve.

We have plans to continue the CTF3 operation at least until 2016. TBL will be equipped with a total of 12 PETS before the 2012 run, and up to 16 structures shall be installed before the end of 2012. This will allow for more detailed beam deceleration studies. Eventually, the produced RF power will be used to condition and test the accelerating structures. Full-fledged CLIC modules will be installed in the TBTS area in order to validate their design with beam measurements. A prototype of the phase feed forward system will be used to demonstrate the phase stabilization concept to the precision needed in CLIC. A dedicated monitor will measure the phase of the beam at the end of the linac. A fast kicker system located in the transfer line between CR and CLEX will then correct eventual phase jitter. This should also improve the operational stability of the facility.

REFERENCES

[1] G.Guignard (Ed.), "A 3 TeV e+e- linear collider based on CLIC technology", CERN 2000-008, 2000.
[2] G.Geschonke and A. Ghigo Eds, "CTF3 Design Report", CERN/PS 2002-008 (RF).
[3] R.Corsini (Ed.), "The CLIC RF power source", CERN 99-06, 1999.
[4] http://clic-meeting.web.cern.ch/clic-meeting/CTF3_Coordination_Mtg/Table_MoU.htm.
[5] R.Corsini et al., "Experimental studies on drive beam generation in CTF3", EPAC08.
[6] A.Dubrovskiy, F.Tecker, "RF pulse compression stabilization at the CTF3 CLIC test facility",IPAC10.
[7] E.Adli, Ph.D. Thesis, University of Oslo, Oslo, 2009.
[8] R.Lillestol, M.Sc. Thesis, Norwegian University of Science and Technology, Trondheim, 2010.
[9] F.Toral et al., "Design, manufacturing and tests of a micrometer precision mover for CTF3 quadrupoles", EPAC08.
[10] E.Adli, D.Schulte, "Beam-Based Alignment for the CLIC Decelerator", CERN-AB-2008-013,EPAC08.
[11] T.Higo et al., 'Various observables of the TW accelerator structures operating in 100 MV/m or higher at X-band Facility, NEXTEF of KEK', Proc. IPAC10.

Appendix B

List of abbreviations

Abbreviation	Meaning
ADC	Analog/Digital Converter
BC	Boundary Condition
BPM	Beam Position Monitor
BPR	Beam Position monitor with Resonant pickup
CERN	The European laboratory for particle physics (originally Conseil Européen pour la Recherche Nucléaire)
CLEX	CLIC EXperimental area
CLIC	Compact Linear Collider
CTF3	CLIC Test Facility 3
FODO	Focusing, drift, Defocusing, drift
GUI	Graphical User Interface
HOM	Higher-Order Mode
IQ	In-phase and Quadrature
LHC	Large Hadron Collider
OTR	Optical Transition Radiation
PETS	Power Extraction and Transfer Structure(s)
PIC	Particle-in-Cell
TBL	Test Beam Line

Table B.1: A list of abbreviations in the thesis. The meaning of the abbreviations are given together with the section in which they are defined.